

**BIPHASIC DISPERSION FUELS FOR HIGH PERFORMANCE HYBRID
PROPULSION**

by

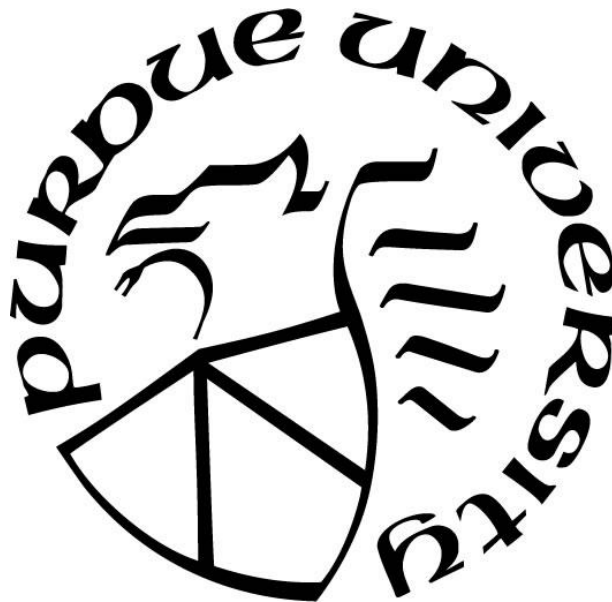
Joshua David Mathews

A Dissertation

Submitted to the Faculty of Purdue University

In Partial Fulfillment of the Requirements for the degree of

Doctor of Philosophy



School of Aeronautics & Astronautics

West Lafayette, Indiana

August 2019

THE PURDUE UNIVERSITY GRADUATE SCHOOL
STATEMENT OF COMMITTEE APPROVAL

Dr. Timothée Pourpoint, Chair

Department of Aeronautics and Astronautics

Dr. Stephen Heister

Department of Aeronautics and Astronautics

Dr. Elias Franses

Department of Chemical Engineering

Dr. Bryan Boudouris

Department of Chemical Engineering

Approved by:

Dr. Wayne Chen

Head of the Graduate Program

To my family

ACKNOWLEDGMENTS

I would like to first thank my advisor, Professor Timothée Pourpoint for his continual help, support, and guidance throughout my doctoral studies. Your efforts have been instrumental in my educational and professional development.

I would also like to thank my committee members, Professor Stephen Heister, Professor Elias Franses and Professor Bryan Boudouris, and my NASA mentor, George Fletcher, for their advice and contributions to the development of my research. To my fellow researchers at the Maurice J. Zucrow Laboratories, specifically the members of Professor Pourpoint's Hydrogen Systems Lab, Green Propellants Lab, and Low-Pressure Lab, thank you for your time, assistance, and friendship.

I would like to thank NASA for providing financial support through the NASA Space Technology Research Fellowship (NSTRF).

I would like to thank my family for always believing in me and supporting me at every step of my education.

Finally, I would like to thank God for providing me with this opportunity. Without your strength, love and guidance, I would not have been able to accomplish this.

TABLE OF CONTENTS

LIST OF TABLES	7
LIST OF FIGURES	8
ABSTRACT	12
1. INTRODUCTION	14
1.1 Motivation.....	14
1.2 Research Objectives.....	16
2. BACKGROUND	17
2.1 Emulsion Applications.....	17
2.2 Secondary Atomization Phenomenon.....	18
2.3 Emulsion Formation and Stabilization.....	20
2.4 Reactive Hybrid Rockets Propellants	26
2.4.1 Hypergolic Propellants	28
2.4.2 Theoretical Performance Gains	31
3. EXPERIMENTAL METHDOS	34
3.1 Component Solubility	34
3.2 Surfactant Screening and Sample Emulsions	35
3.3 Fuel Binder Emulsions.....	39
3.4 Droplet Size Diagnostics and Internal Droplet Structure	40
3.5 Biphasic Dispersion Fuels Synthesis and Casting	44
3.5.1 Batch Mixing Vessel and Fuel Grain Synthesis - Design One	46
3.5.2 Batch Mixing Vessel and Fuel Grain Synthesis - Design Two	49
3.5.3 Batch Mixing Vessel and Fuel Grain Synthesis - Design Three	51
3.6 Combustion Performance and Data Analysis	56
4. RESULTS AND DISCUSSION.....	60
4.1 Liquid Fuel Additives and Surfactant Screening.....	60
4.2 Liquid Fuel Additive Solubility Experiments.....	60
4.3 Surfactant Screening Experiments.....	65
4.3.1 Liquid Additive One - Ethanol	66
4.3.2 Liquid Additive Two - Water	70

4.3.3 Liquid Additive Three - Formamide.....	76
4.4 Stokes' Settling Velocity and Droplet Sizing.....	81
4.5 Biphasic Dispersion Fuel Synthesis.....	89
4.6 Combustion Performance Analysis.....	93
5. CONCLUSIONS AND FUTURE WORK.....	108
APPENDIX.....	112
REFERENCES.....	116
VITA.....	120
PUBLICATIONS.....	122

LIST OF TABLES

Table 2.1 Predicted superheat limit values for water, ethanol, and formamide and saturation temperatures of several n-alkanes at 200 psia	20
Table 2.2 List of surfactant molecules.....	23
Table 2.3 Solvation parameters of several different polar solvents.....	25
Table 2.4 Molecular structure and ignition delay of selected hypergolic fuels.....	30
Table 2.5 Theoretical peak performance values for different BDF formulations. [†]	33
Table 4.1 Summary of OCC test results.	94
Table 4.2 Regression rate correlation data for different hybrid rocket propellants	95

LIST OF FIGURES

Fig. 2.1 Emulsions formed between paraffin oil and water using a high shear homogenizer. a) 10 wt.% water, no surfactant. b) 10 wt.% water, 1 wt.% nonionic surfactant.	24
Fig. 2.2 Diffusion-limited combustion of a hybrid rocket motor [24].....	27
Fig. 2.3 Hypergolic drop test vessel. [26].....	29
Fig. 2.4 Hypergolic drop test of MON-25 on 2,3-Dihydrofuran. Time stamps indicate time from propellant contact.	30
Fig. 2.5 Theoretical characteristic velocities for eight different hybrid fuel formulations.....	32
Fig. 2.6 Theoretical sea level specific impulse for eight different hybrid fuel formulations.	32
Fig. 2.7 Theoretical sea level density impulse for eight different hybrid fuel formulations.	33
Fig. 3.1 Emulsion component solubility apparatus.....	34
Fig. 3.2 FR 5560 paraffin wax composition as determined by GC/MS analysis.....	36
Fig. 3.3 Sample emulsions formed between water and squalane oil using different surfactants. a) Polyethylene glycol oleyl ether used as a surfactant. b) Sorbitan monooleate used as a surfactant.	39
Fig. 3.4 Optically accessible emulsion visualization apparatus.....	40
Fig. 3.5 Peclet number as a function of droplet radius for an emulsion of water in squalane oil.	44
Fig. 3.6 Biphasic dispersion fuel synthesis system plumbing and instrumentation diagram.	45
Fig. 3.7 Biphasic dispersion fuel synthesis system. Instrumentation labels match those found in fuel synthesis system plumbing and instrumentation diagram above.	46
Fig. 3.8 Batch BDF mixing vessel design one. a) Mixing vessel. b) Piston head. c) Top flange. d) Threaded drive shaft. e) CAD rendering of completed assembly.	47
Fig. 3.9 Neat paraffin fuel grain extrusion process. a) Molten paraffin wax in vessel. b) Wax cooled to 45°C in vessel. c) Top flange replaced with cutting plate. d) First inch of fuel grain extrusion. e) Last inch of fuel grain extrusion.	48
Fig. 3.10 Neat paraffin fuel grains. a) Fuel grains after extrusion. b) Fuel grains after reshaping with a heated mold. c) Cut-view of an extruded fuel grain.	49
Fig. 3.11 Mixing vessel design two with coring cylinder. a) Guide plate and coring cylinders. b) CAD assembly of mixing chamber with guide plate and coring cylinders in place.....	50
Fig. 3.12 Batch BDF mixing vessel design three.....	51
Fig. 3.13 Injection-style fuel grain casting mold assembly.	52
Fig. 3.14 Test cast one. Trapped gas bubbles formed voids during the cooling process.....	53

Fig. 3.15 Neat paraffin wax injection test cast two, using an acrylic grain mold for optical accessibility.....	54
Fig. 3.16 Neat paraffin fuel grain cast using the final design iteration of the injection-style grain mold assembly.	54
Fig. 3.17 One-dimensional heat transfer analysis of injection-style casting mold design.....	56
Fig. 3.18 Optically accessible hybrid rocket motor design and components.....	57
Fig. 3.19 Combustion of a neat paraffin fuel grain in the OCC. Flow is from left to right. a) 0.025 seconds after ignition. b) 0.950 seconds after ignition.	58
Fig. 3.20 Neat paraffin fuel grain after a combustion test in the OCC. Flow is from left to right	58
Fig. 4.1 Mutual solubilities of FR 5560 paraffin wax and water at 75°C. a) Solubility plot. b) 1 wt.% water in wax, after stirring. c) 1 wt.% water in wax after three hours. d) 1 wt.% wax in water after stirring and waiting three hours.	61
Fig. 4.2 Mutual solubilities of FR 5560 paraffin wax and ethanol at 75°C. a) Solubility plot. b) 9 wt.% ethanol in wax, after stirring. c) 9 wt.% ethanol in wax after three hours. d) 2 wt.% wax in ethanol after stirring.....	62
Fig. 4.3 Mutual solubilities of FR 5560 paraffin wax and formamide at 75°C. a) Solubility plot. b) 2 wt.% formamide in wax, after stirring. c) 2 wt.% formamide in wax after one hour. d) 1 wt.% wax in formamide after stirring.	63
Fig. 4.4 Mutual solubilities of squalane and water at 25°C. a) Solubility plot. b) 1 wt.% water in squalane before and after mixing. c) 1 wt.% squalane in water before and after mixing.....	64
Fig. 4.5 Mutual solubilities of squalane and ethanol at 25°C. a) Solubility plot. b) 3 wt.% ethanol in squalane before and after mixing. c) 3 wt.% squalane in ethanol before and after mixing.....	65
Fig. 4.6 Ethanol-in-oil emulsion control group, formed without a surfactant. Composition is 90 wt.% oil and 10 wt.% ethanol.....	67
Fig. 4.7 Ethanol-in-oil emulsion formed with glycerol monostearate as a surfactant. Composition is 89.5 wt.% oil, 10 wt.% ethanol, 0.5 wt.% surfactant.....	68
Fig. 4.8 Ethanol-in-oil emulsion formed with Brij® 93 as a surfactant. Composition is 89.5 wt.% oil, 10 wt.% ethanol, and 0.5 wt.% surfactant.	69
Fig. 4.9 Water-in-oil emulsion control group, formed without a surfactant. Composition is 90 wt.% oil and 10 wt.% DI water.	70
Fig. 4.10 Water-in-oil emulsion formed with Brij® 52 as a surfactant. Composition is 89.5 wt.% oil, 10 wt.% water, and 0.5 wt.% surfactant	71
Fig. 4.11 Water-in-oil emulsion formed with Span® 85 as a surfactant. Composition is 89.5 wt.% oil, 10 wt.% water, and 0.5 wt.% surfactant.	72

Fig. 4.12 Water-in-oil emulsion formed with Span® 80 as a surfactant. Composition is 89.5 wt.% oil, 10 wt.% water, and 0.5 wt.% surfactant.	72
Fig. 4.13 Water-in-wax emulsion control group, formed without a surfactant. Composition is 90 wt.% wax and 10 wt.% DI water.	73
Fig. 4.14 Water-in-wax emulsion formed with Span® 85 as a surfactant. Composition is 89.5 wt.% wax, 10 wt.% water, and 0.5 wt.% surfactant.	74
Fig. 4.15 Water-in-wax emulsion formed with Span® 80 as a surfactant. Composition is 89.5 wt.% wax, 10 wt.% water, and 0.5 wt.% surfactant.	75
Fig. 4.16 Water-in-oil emulsion formed at 75°C with Span® 80 as a surfactant. Composition is 89.5 wt.% oil, 10 wt.% water, and 0.5 wt.% surfactant.....	76
Fig. 4.17 Formamide-in-wax emulsion control group, formed without a surfactant. Composition is 80 wt.% wax and 20 wt.% formamide.	77
Fig. 4.18 Formamide-in-paraffin oil emulsion control group, formed without a surfactant. Composition is 90 wt.% oil and 10 wt.% formamide.....	78
Fig. 4.19 Formamide-in-paraffin oil emulsion formed with Span® 80 as a surfactant. Composition is 89.0 wt.% oil, 10 wt.% formamide, and 1.0 wt.% surfactant.....	78
Fig. 4.20 Formamide-in-wax emulsion, formed with Span® 80 as a surfactant. Composition is 79.5 wt.% wax, 20 wt.% formamide, and 0.5 wt.% surfactant.....	79
Fig. 4.21 Formamide-in-wax emulsion, formed with Triton™ X-100 as a surfactant. Composition is 79.5 wt.% wax, 20 wt.% formamide, and 0.5 wt.% surfactant.	80
Fig. 4.22 Formamide-in-wax emulsion, formed with Brij® 52 as a surfactant. Composition is 79.5 wt.% wax, 20 wt.% formamide, and 0.5 wt.% surfactant.....	80
Fig. 4.23 Experimental data points of interfacial position of the emulsion pictured in Fig. 4.12.	82
Fig. 4.24 Relationship between droplet settling velocity and droplet radius for an emulsion of water in squalane, assuming Stokes' flow.	83
Fig. 4.25 Image of emulsified water droplets taken on a HIROX KH-8700 digital microscope under 700 times magnification.....	84
Fig. 4.26 Histogram of emulsion droplet diameters for the emulsion pictured in Fig. 4.12.....	84
Fig. 4.27 Image of an undiluted emulsion taken on a HIROX KH-8700 digital microscope under 140 times magnification.....	85
Fig. 4.28 Water-in-wax emulsion formed with Span® 80 as a surfactant. Composition is 79.5 wt.% wax, 10 wt.% water, and 0.5 wt.% surfactant	86
Fig. 4.29 Experimental data points of interfacial position of the emulsion pictured in Fig. 4.28.	87
Fig. 4.30 Image of emulsified water droplets from a diluted BDF sample taken on a HIROX KH-8700 digital microscope under 700 times magnification.....	88

Fig. 4.31 Histogram of emulsion droplet diameters for the emulsion pictured in Fig. 4.28.....	88
Fig. 4.32 Rapid formation of droplet aggregates in an emulsion formed between water and paraffin wax.	89
Fig. 4.33 Water-in-paraffin oil emulsion formed with a mixture of Span® 80 and Triton™ X45 as surfactants. Composition is 85 wt.% oil, 10 wt.% water, and 5 wt.% surfactant.	90
Fig. 4.34 Ethanol-in-paraffin oil emulsion formed with Span® 80 as surfactants. Composition is 85 wt.% oil, 10 wt.% aqueous ethanol solution, and 5 wt.% surfactant.	91
Fig. 4.35 Hybrid rocket fuel grains prepared for OCC testing. a) BDF formulation one. b) BDF formulation two.....	92
Fig. 4.36 BDF formulation three fuel grains cast using a rapidly cooled injection-style casting mold assembly.	93
Fig. 4.37 Measured space-time-average regression rates for several different hybrid rocket fuels plotted as a function of mean oxidizer mass flux.	96
Fig. 4.38 Measured space-time-average regression rates for all three biphasic dispersion fuel formulations plotted as a function of mean oxidizer mass flux.	97
Fig. 4.39 Combustion environment and flame height comparison between three different fuels. Flow is left to right. a) Neat paraffin fuel. b) BDF one (water) c) BDF two (ethanol) d) BDF three (water).	98
Fig. 4.40 Three subsequent frames from the combustion of hybrid rocket fuels. Flow is left to right. a) Neat paraffin fuel. b) BDF one (water) c) BDF two (ethanol) d) BDF three (water).	99
Fig. 4.41 Surface pitting in a fuel grain of BDF formulation three.	100
Fig. 4.42 Expected nominal fuel grain densities and measured fuel grain densities for neat paraffin and BDF formulation three.	101
Fig. 4.43 X-ray CT scan image of BDF-3 sample. a) Live x-ray image. b) Image of horizontal slice showing voids.	101
Fig. 4.44 Pressure traces of four different hybrid rocket fuel formulations tested in the OCC..	102
Fig. 4.45 Average combustion efficiencies of four different hybrid rocket fuel formulations tested in the OCC.	103
Fig. 4.46 Combustion efficiency of all twenty tests performed in the OCC.	104
Fig. 4.47 Maximum theoretical characteristic velocity for each fuel formulation as a function of O/F ratio. Numbers refer to test numbers found in Table 4.1.	105
Fig. 4.48 Thrust profile for four different hybrid rocket fuels tested in the OCC at an average nominal oxidizer mass flux of 150 kg/m ² /s	107

ABSTRACT

Author: Mathews, Joshua, D. PhD

Institution: Purdue University

Degree Received: August 2019

Title: Biphasic Dispersion Fuels for High Performance Hybrid Propulsion.

Committee Chair: Dr. Timothée Pourpoint

Hybrid rocket propulsion is a crosscutting technology with the potential for significant cost reductions and improvements in safety and simplicity over liquid and solid rocket propellants. Significant strides have been made in the past decade with both paraffin-based hybrid fuels and traditional polymeric hybrid fuels by including solid additives to increase regression rates and thrust levels. Yet low combustion efficiencies and high-mass exhaust products have limited performance gains.

This dissertation describes a novel approach to synthesize high performance multiphase hybrid rocket propellants via the formation of biphasic dispersions. The techniques employed involve the emulsification of liquid fuels within solid fuel binders at elevated temperature and pressure to create an internal structure composed of homogeneously dispersed micron-sized liquid fuel droplets. The primary goal of the research is to demonstrate augmented regression rates, without reducing combustion efficiency, of the biphasic dispersion fuels relative to traditional hybrid rocket fuels due to the proposed mechanism of secondary atomization. The biphasic dispersion fuels are prepared under an inert, pressurized environment via high-shear homogenization and cast into cylindrical fuel grains. The combustion performance of each biphasic dispersion fuel is analyzed using an optically accessible small-scale hybrid rocket motor that allows for the measurement of fuel regression rates, thrust, and combustion efficiency. Additionally, the average dispersed droplet diameter and internal droplet structures are investigated for each synthesized propellant formulation via optical microscopy and x-ray computed tomography techniques. Three different biphasic dispersion fuels were prepared. The first fuel formulation (BDF-1) contained 75 wt.% paraffin wax, 20 wt.% deionized water, and 5 wt.% surfactant. The second fuel formulation

(BDF-2) contained 75 wt.% paraffin wax, 20 wt.% aqueous ethanol solution (95:5 ethanol to water by mass), and 5 wt.% water. The third fuel formulation (BDF-3) contained 79.5 wt.% paraffin wax, 20 wt.% deionized water, and 0.5 wt.% surfactant. The biphasic dispersion fuels formed between water and paraffin wax served as non-reactive cases to validate the effects of secondary atomization and trouble shoot the procedures required to synthesize and cast propellants. Combustion performance tests of BDF-1 showed moderate increases in both regression rate (up to a 30% increase) and mean combustion efficiency (1% increase), relative to neat paraffin wax fuels tested at similar conditions. The biphasic dispersion fuels formed between ethanol and paraffin wax (BDF-2) showed greater increases in regression rate (up to an 86% increase) but moderate decreases in mean combustion efficiency (4% decrease), relative to neat paraffin wax fuels tested at similar conditions. However, emulsion experiments indicated that no surfactant molecule was able to adequately stabilize ethanol and prevent emulsion separation. BDF-2 formulations were prepared by continuously stirring while cooling the mixture until the wax solidified, preventing further droplet separation. Similarly, emulsion experiments indicated that no surfactant molecule was able to adequately stabilize formamide and prevent emulsion separation. After modification of the synthesis and casting procedures, a third biphasic dispersion fuel formulation was formed between water and paraffin wax. BDF-3 exhibited substantial increases in regression rate (up to a 543% increase) and moderate improvements in mean combustion efficiency (4% increase), relative to neat paraffin wax fuels tested at similar conditions. Droplet settling velocity analysis performed using backlit digital photography indicated an average droplet diameter on the order of 80 μm but optical microscopy analysis of diluted samples indicated average droplet diameters on the order of 5 μm . Density measurements and x-ray CT analysis of BDF-3 fuel grains indicated that a significant portion of the dispersed water droplets leaked prior to testing, leaving a porous, internal void structure. The improvements in regression rate for these fuel grains are attributed to an increased burn surface area and thus increased fuel mass flowrate. Preliminary work with the emulsification of liquid fuels into paraffin wax has shown potential for transformative improvements to the current state of hybrid fuels. Further testing is required to find surfactants that could help to better stabilize emulsions, prior to cooling them and solidifying the fuel binder, preventing further separation. Additionally, further testing of biphasic dispersion with more volatile liquid additives and other binders is required to demonstrate the benefits of secondary atomization effects in hybrid rocket propellants.

1. INTRODUCTION

1.1 Motivation

The term hybrid rocket most commonly refers to a chemical propulsion system comprised of a liquid oxidizer and a solid fuel. The advantages of such propellant combinations are versatility, safety, and the ability to throttle or shutdown on command. However, traditional hybrid rocket fuels such as hydroxyl-terminated polybutadiene (HTPB), polyethylene (PE), or dicyclopentadiene (DCPD) exhibit low regression rates, and thus require larger burning surface areas to generate high thrust which can be accomplished through the use of a multi-port design or exotic port configurations such as wagon-wheel fuel section. Multi-port designs can be effective at increasing thrust, but the port design also increases manufacturing complexity, reduces the total fuel volume available for combustion, and can leave a significant portion of the fuel unburned in the form of fuel slivers. [1] Solid additives can improve the combustion performance of hybrid rocket propellants in terms of density impulse and regression rate by increasing the transfer of energy from the flame zone to the fuel surface. For example, pyrophoric additives, hydrogen-rich metal hydrides, and metal particles such as nano aluminum have been studied at Purdue by Shark and Zaseck as a means to increase the combustion performance of solid fuels like dicyclopentadiene (DCPD) and paraffin wax. [2],[3] Similarly, Weismiller et al. studied the effect of adding ammonia-borane to hybrid fuels and demonstrated increases in regression rate of up to 40%. [4] However, solid additives pose several issues for hybrid rocket systems. First, due to large differences in density, solid additives can be difficult to homogeneously disperse throughout a fuel binder. Additionally, unburned additives can be detrimental to a rocket system's performance, limiting combustion efficiency and reducing exhaust gas velocity due to two-phase flow losses, as well as causing nozzle erosion, as discussed by Li et al. [5]

An alternative approach to increasing the regression rate of hybrid fuels is to use liquefying propellants [6]. Liquefying hybrid propellants form a hydro-dynamically unstable, low viscosity melt layer on the fuel surface during combustion, resulting in the entrainment of molten fuel under the strong shear force of oxidizer flow. Karabeyoğlu et al. have demonstrated this phenomenon in paraffin wax-based propellants, achieving 300-400% increases in regression rate over polymeric

hybrid fuels [6]. However, entrained fuel droplets can leave the nozzle prior to complete combustion, resulting in lower combustion efficiencies than those achieved in both liquid and single-component solid rocket engines. For instance, combustion efficiencies for a large-scale paraffin hybrid rocket engine tested by Karabeyoğlu et al. ranged from 79 to 91%, depending on the test conditions [7].

To further enhance the combustion performance of hybrid propellants, liquid fuel additives can be dispersed within a solid fuel binder. Reactive and/or volatile liquid fuels do not possess the same difficulties as many solid additives in igniting and burning completely, but still possess high energy densities and thus are promising candidates for rocket applications aimed at increasing fuel regression rates. Liquid fuels can be homogeneously dispersed into a fuel binder via emulsification and cured to form a biphasic dispersion fuel (BDF) in which volatile liquid fuel droplets comprise a significant portion of the total propellant mass. In addition to the benefits of a liquid additive's heat of combustion and reduced heat of vaporization relative to the fuel binder, BDF formulations could show an improved combustion performance due to secondary atomization effects which result from significant differences in the boiling points of the fuel binder and liquid fuel additive. As emulsified droplets are entrained from the fuel surface, heat is transferred to the interior containing the liquid fuel additive, causing the internal pressure to increase to the point of explosion and subsequent secondary droplet breakup. This secondary droplet breakup could help to increase mixing and reduce the amount of unburned fuel droplets leaving the nozzle. Additionally, if sufficient heat is transferred to the fuel grain during combustion, the trapped liquid near the surface could boil and eventually burst, causing an increase in the fuel burning surface area. Surface explosions and an increased surface area translate to a larger mass transfer rate of fuel to both the turbulent melt layer of the propellant and the flame zone, in turn producing more thrust. Thus, a hybrid fuel composed of a solid fuel binder and a dispersed reactive and/or volatile liquid fuel could potentially exhibit increased combustion efficiency, regression rate, and thrust relative to the current state of the art, without requiring a complex fuel port design. No mention of biphasic dispersions has been found in literature with application to hybrid rocket propellants and thus is a topic rich with material for investigation.

1.2 Research Objectives

The research presented in this dissertation focuses on investigating the effects of incorporating micron-scale liquid fuel droplets into hybrid rocket propellants and evaluating the combustion performance of these synthesized biphasic dispersion fuel (BDF) formulations. A small-scale hybrid rocket motor is used to evaluate propellant combustion performances based on the metrics of regression rate, combustion efficiency, and thrust. Optical microscopy and x-ray computed tomography (CT) techniques are employed to investigate the average droplet size and internal droplet structure of the propellants. Theoretical and experimental work found in literature provide a general understanding of the behavior and governing principles of emulsions and biphasic dispersions, but little work has been performed on the synthesis of biphasic dispersions between non-aqueous fuels and hybrid fuel binders, such as paraffin wax. Thus, much of the work relevant to hybrid rocket biphasic dispersion fuels must be determined experimentally, on a case-by-case basis. The specific objectives of this study include:

1. Gain a fundamental understanding of the physical and surface chemistry relevant to kinetically stable liquid-fuel-in-solid-fuel-binder biphasic dispersions.
2. Develop a set of procedures to select potential liquid fuel candidates and determine the ideal formulations for both increased combustion performance relative to the state of the art and long-term propellant stability.
3. Develop experimental hardware to synthesize and test the performance of hybrid rocket biphasic dispersion fuels.
4. Analyze the stability against separation and the internal droplet structure of hybrid rocket biphasic dispersion fuels.
5. Analyze the combustion performance of biphasic dispersion fuels via a small-scale hybrid rocket motor.

2. BACKGROUND

2.1 Emulsion Applications

Hiemenz and Rajagopalan define a colloid as any suspended particle with a linear dimension in the range of 1 nm to 1 μm . [8] Colloidal dispersions are a general class of mixtures defined by colloidal particles of any phase, dispersed in a continuous medium of a different phase. Emulsions are a more specific type of dispersion in which the dispersed and continuous phases are immiscible liquids. In the present work, we refer to the synthesized fuels as biphasic dispersions since they contain liquid droplets within a solid binder with average droplet diameters that exceed the limits defined by a colloidal dispersion. Droplet sizes can be estimated using Stokes' law. Emulsions formed between molten paraffin wax and liquid additives can be monitored using periodic photographs, while maintaining elevated temperature and pressure. The settling of emulsified droplets through the continuous phase over specific time intervals provide a measure of the experimental Stokes' settling velocity that can be used to estimate the mean dispersed droplet diameter. Emulsion droplet sizing results can be corroborated for solidified biphasic dispersions using diagnostic imaging techniques such as x-ray computed tomography, which relies on density differences within the sample to form three-dimensional images of the internal structure.

Emulsions and other dispersion systems are pervasive, finding use in many science and engineering disciplines such as analytical chemistry, chemical manufacturing, materials science, and petroleum engineering. Paints, cosmetics and ceramics, etc are all products that involve or are in themselves a colloidal or biphasic dispersion. In addition to common consumer products, emulsions have also been used in combustion science applications to increase combustion efficiency, reduce NO_x formation, and lower particulate matter emissions. For instance, Syu et al. emulsified water into diesel fuels at varying concentrations to study the effect of water content on the thermal efficiency and pollutant emission concentrations of a diesel engine. [9] Experimentation indicated that diesel fuels containing 15 wt.% water increased the engine thermal efficiency by 19% and reduced NO emissions by 45.4%, relative the combustion of diesel fuel alone. Similarly, Chavez et al. dispersed water into a high-viscosity heavy fuel oil to increase the combustion efficiency of an electric power conversion furnace. [10] Tests indicated that the

sprayed fuel emulsions reduced particulate matter emission by up 36%, relative to the combustion of heavy fuel oils alone. Lasheras et al. tested the combustion behavior of both solutions and emulsions formed between n-paraffins and several different alcohols that were sprayed into a vertical combustion duct maintained at atmospheric pressure. [11] Disruptive burning phenomenon, or microexplosions, were observed via high-speed video for emulsions formed between ethanol and n-paraffins, with the strength of the explosion dictated by the relative concentration of each constituent. In contrast to the sprayed fuel emulsions studied by Syu, Chavez, and Lasheras, I sought to take advantage of microexplosions in a hybrid rocket system to both increase burn surface area and increase turbulent mixing as a means of augmenting combustion efficiency, fuel regression rate and thrust, relative to the current state of the art.

2.2 Secondary Atomization Phenomenon

Lasheras et al. first observed disruptive burning effects, or secondary atomization, during the combustion of sprayed fuel mixtures, as mentioned previously. [11] In their work, both solutions and emulsions formed between n-paraffins and several different alcohols were sprayed into a vertical combustion duct maintained at atmospheric pressure and their combustion performance was monitored via high-speed video. Combustion gases from a premixed, laminar flame stabilized on a flat-plate burner provided a high-temperature vertical gas flow, injected into a combustion duct in opposition to gravitational acceleration. A droplet generation chamber produced droplets containing different n-paraffin/alcohol mixtures and injected them into the combustion duct, parallel to the gas flow. The initial diameter of all injected droplets was in the range of 250 to 400 μm . Lasheras et al. monitored the droplet combustion characteristics, including the strength and location of disruptive microexplosion phenomenon along the droplet trajectories visually, noting specifically a sudden increase in droplet diameter at the onset of spontaneous nucleation and a broadened and more intense flame emission at the point of microexplosions. [11] Microexplosions were observed for both solutions and emulsions formed between ethanol and n-paraffins, with the strength of the explosion dictated by the relative concentration of each constituent. Fuel mixtures exhibited microexplosions for solutions formed between ethanol and n-paraffins ranging from n-undecane ($\text{C}_{11}\text{H}_{24}$) to n-tridecane ($\text{C}_{13}\text{H}_{28}$), and for emulsions formed between ethanol and n-paraffins ranging from n-tetradecane ($\text{C}_{14}\text{H}_{30}$) to n-hexadecane ($\text{C}_{16}\text{H}_{34}$). Only mixtures that

contained n-paraffins with saturation temperatures exceeding the superheat limit of ethanol exhibited microexplosions.

Shepherd et al. proposed that secondary atomization, or microexplosions, occur due to a phenomenon termed spontaneous homogenous nucleation. [12] A liquid dispersed within another liquid is shielded from potential nucleation sites and can be brought to its superheat limit. The superheat limit, T_L , is defined as the maximum temperature to which a substance can be brought, above its boiling point, without vaporizing, and is a function of the substance's saturation temperature, saturation pressure, and surface tension. Once the superheat limit is reached, homogenous nucleation can occur, resulting in rapid evaporation and explosion. Elgowainy suggested that for secondary atomization to take place, the superheat limit of the interior phase must be below the saturation temperature of the surrounding phase [13], which is in agreement with experimental results of Lasheras et al. [11] For many substances, the superheat limit is about 90% of the critical temperature. For instance, Ching et al. determined that superheat limit of ethanol ranged from 85% to 91% of its critical temperature, depending on the rate of heating. [14] However, thermophysical data and experimental results of a substance's superheat limit are often not readily available. Law described a method of accurately estimating a liquid's superheat limit via a two-parameter equation of state and the boundary conditions relevant to the thermodynamic limit of superheat. [15] Assuming that the ambient pressure for the given application is significantly smaller than the liquid's critical pressure, the superheat limit can be described as a function of the ambient pressure, P , and a free parameter, n , as shown in Eq. 1.

$$\hat{T}_L = \left(\frac{27}{32}\right)^{(1/n+1)} + \frac{1}{8(n+1)}\hat{P} \quad (1)$$

The $\hat{}$ operator in Eq. 1 signifies the ratio of a variable to its value at the critical state. n can vary between the values of zero and one. Using the same approach, Eberhart and Schnyders found that a value of 0.5 for n provided good agreement with experimental observations of the superheat limit of various hydrocarbons. [16] Additionally, for values of \hat{P} less than 0.4, the simplifying assumption applied in deriving Eq. 1 predicts the thermodynamic limit of superheat of a liquid with a maximum of 0.5 % error. A more detailed analysis, including the derivation of Eq. 1 can be

found in the work of Law. [15] Table 2.1 provides values for the predicted superheat limit of water, ethanol, and formamide with $n = 0.5$, as well as the saturation temperature of various n-alkanes from hexane to dodecane, as reported in the NIST Thermophysical Properties Webbook [17].

Table 2.1 Predicted superheat limit values for water, ethanol, and formamide and saturation temperatures of several n-alkanes at 200 psia

Liquid Additive	Critical Temperature/Predicted Superheat Limit (P = 200 psia) [±]
Water	647 K/581 K
Ethanol	516 K/470 K
Formamide	537 K/488 K
n-alkane	Saturation Temperature (P = 200 psia) [±]
Hexane (C ₆ H ₁₄)	456 K
Heptane (C ₇ H ₁₆)	494 K
Octane (C ₈ H ₁₈)	528 K
Decane (C ₁₀ H ₂₂)	587 K
Dodecane (C ₁₂ H ₂₆)	638 K

[±] Nominal average chamber pressure of all hybrid rocket biphasic dispersion fuel tests

In the present work, biphasic dispersions are formed between various liquid additives and FR 5560 grade paraffin wax, which consists of an approximately normal distribution of n-alkanes ranging from C₂₄H₅₀ to C₄₀H₈₂, as determined using gas chromatography and mass spectrometry (GC/MS) analysis. As the chain length of an n-alkane increases, so does the boiling point and saturation temperature. In the case of a biphasic dispersion containing droplets of water, ethanol, or formamide dispersed within FR 5560 paraffin wax, all n-alkane constituents have saturation temperatures well above the superheat limit of the dispersed liquid additives and thus could produce disruptive burning phenomenon.

2.3 Emulsion Formation and Stabilization

A thermodynamic analysis of the interface that forms between two immiscible fluids is helpful to understanding the behavior and formation of emulsions. When considering a mixture of two immiscible fluids, the interfacial tension can be described by the energy required to increase the interfacial area by a finite amount or by the work per unit area required to expand the interface between the two fluids. Alternatively, by using the first and second law of thermodynamics for a reversible, constant temperature, and constant pressure process, one can describe the interfacial

tension as the incremental change in Gibbs free energy per unit change in interfacial area. The interfacial tension is a result of complex surface forces acting at the interface of two or more components of a mixture, and the reader should refer to the work of Hiemenz and Rajagopalan for a more detailed thermodynamic analysis. [8] The relationship between interfacial tension and Gibbs free energy gives important insight into the formation of emulsions. Specifically, for a positive and constant interfacial tension, expansion of an emulsion's interfacial area results in a positive change in Gibbs free energy, which demonstrates that emulsion formation is thermodynamically unfavorable and does not occur spontaneously. Thus, a means of stabilization is required to prevent separation of the components and slow the process of emulsion breaking. For the purposes of this work, one means of defining emulsion stability is the time required, after emulsion formation, for a mixture to undergo complete separation into two distinct phases.

Agitation and/or stirring of a mixture of two immiscible fluids provides a means of droplet formation and further droplet breakup, with an associated increase in the interfacial area between the two fluids. During this process, new droplets are formed, yet several different mechanisms can cause droplet breakdown or growth, simultaneously. As the distance between droplets decrease, van der Waals forces overcome repulsive forces and droplet aggregates form by a process termed flocculation. Thin layers of continuous phase trapped between aggregated droplets can hinder the growth of these droplets. However, as the liquid layer between droplets becomes sufficiently thin, attractive forces can induce droplet coalescence or merging, causing an overall decrease in the number of droplets, an increase in the average volume of droplets. Ostwald ripening, or disproportionation is driven by the solubility of the dispersed phase in the continuous phase. Although emulsions are defined as systems of two immiscible fluids, all real systems will have a non-negligible mutual solubility. Differences in the chemical potential between droplets of different diameters causes dispersed phase molecules to diffuse from the surface of smaller droplets into the bulk and eventually combine with larger droplets. [18] Thus, larger droplets will grow at the expense of smaller droplets, causing an increase in the system's polydispersity. Additionally, as the breakdown mechanisms just described take place, differences in the density of the dispersed and continuous phases give rise to buoyancy forces, causing sedimentation or creaming of dispersed droplets, depending on the sign of the density difference. Since no emulsion system is perfectly monodisperse, droplets of different sizes will travel through the continuous

phase at different rates, leading to further droplet flocculation and/or coalescence and eventually the complete breakdown of the emulsion. Tadros provides more detail on the thermodynamics and physical processes relevant to each of the above-mentioned breakdown mechanisms. [19]

Surfactants or surface-active-agents are amphiphilic molecules, containing both hydrophobic and hydrophilic sections, which can adsorb at the interface between the two fluids in an emulsion, providing an energy barrier to emulsion breakdown and droplet growth. In general, surfactants can be classified into different categories, based on their physicochemical properties. Anionic surfactants contain a negatively charged functional group at the head of the molecule. Some common examples include sodium lauryl ether sulfates and alkylbenzene sulfonates, both of which are used as detergents, shampoos, soaps, etc. Cationic surfactants, such as Benzalkonium chloride (BAC) contain a positively charged functional group at the head and find use as anti-microbial agents. Amphoteric or zwitterionic surfactants contain both cationic and anionic functional groups. Their properties depend strongly on the pH of the solution in which they are dissolved. In contrast to ionic surfactants, non-ionic surfactants do not contain charged functional groups as the name implies. Non-ionic surfactants include a wide variety of chemical structures which can be used in a wide variety of applications, including wetting agents, food-grade additives, cleaners, emulsifiers, etc. For applications to emulsions, the adsorption of the surfactant molecules at the interface provides a physical boundary between neighboring droplets, preventing droplet breakdown via steric stabilization. For the purposes of this research, I experimented with 18 different surfactants, representing five classes of non-ionic surfactants. Table 2.2 below lists the different surfactants that were used.

Table 2.2 List of surfactant molecules.

Class	Chemical Name	Brand Name
Poly (alkylene oxide) block copolymers	Poly(ethylene glycol)-block-poly(propylene glycol)-block-poly(ethylene glycol)	Pluronic® L81
	Ethylenediamine tetrakis (propoxylate-block-ethoxylate) tetrol	Tetronic® 701
	Polyethylene-block-poly(ethylene glycol)	N/A
Oligomeric alkyl-ethylene oxides	Polyethylene glycol hexadecyl ether	Brij® 52
	Polyethylene glycol oleyl ether	Brij® 93
	Polyethylene glycol dodecyl ether	Brij® L4
	Secondary alcohol ethoxylate	Tergitol™ 15-S-7
Alkyl-phenol Ethoxylates	Polyethylene glycol 4-tert-octylphenyl ether	Triton™ X-45
	Polyethylene glycol tert-octylphenyl ether	Triton™ X-100
Sorbitan esters	Sorbitan monostearate	Span® 60
	Sorbitan tristearate	Span® 65
	Sorbitan monooleate	Span® 80
	Sorbitan triooleate	Span® 85
	Polyethylene glycol sorbitan monostearate	Tween® 60
	Polyethylene glycol sorbitan monooleate	Tween® 80
	Polyoxyethylene sorbitan triooleate	Tween® 85
Stearic acid derivatives	Stearic acid	N/A
	Glycerol monostearate	N/A

The efficacy of a surfactant molecule in providing emulsion stabilization is dependent on the emulsion components and thus finding a surfactant that works well for a specific application requires experimentation. To illustrate the effect that surfactants can have on emulsion stability, Fig. 2.1 shows two different emulsion formed between paraffin oil and deionized (DI) water. As Fig. 2.1a shows, the emulsion is unstable and separates quickly without the use of a surfactant. After 15 minutes, the water and oil were completely separated, with the water phase resting at the bottom of the vial. In contrast, Fig. 2.1b illustrates the effectiveness of Span 80 to slow separation. After 6 hours, emulsified water droplets began to settle. After 24 hours, emulsified water droplets had settled roughly one-third of the total vial height.



Fig. 2.1 Emulsions formed between paraffin oil and water using a high shear homogenizer. a) 10 wt.% water, no surfactant. b) 10 wt.% water, 1 wt.% nonionic surfactant.

Additional testing and optimization of surfactants can result in greater stability, even preventing separation for months. However, droplet migration and droplet breakdown mechanisms are dependent on the continuous phase viscosity. For the present work, emulsions are formed between molten paraffin wax and a polar liquid additive, while maintaining the mixture at elevated temperature and pressure. As the emulsion cools and the wax solidifies, a biphasic dispersion is formed with liquid droplets trapped within the solid binder. The cooling of the wax causes solidification, eliminating further separation. Thus, for the current application, emulsions need only to be stable enough to avoid separation for the time required to cool the mixture below the melting point of the wax.

In general, aqueous emulsions can be categorized by which fluid forms the dispersed and continuous phases, respectively. For instance, an emulsion containing water dispersed as droplets in a non-polar oil phase can be defined as a water-in-oil (W/O) emulsion. The converse can be described as an oil-in-water (O/W) emulsion, that is, if the emulsion contains droplets of oil dispersed in an aqueous phase. Literature also cites oil-in-oil (O/O) type emulsions and so called O/W/O or W/O/W multiple-emulsions [20],[21]. Much of the research pertaining to emulsions involves the formation of W/O or O/W type emulsions. However, little research has detailed the

formation of non-aqueous emulsions, in which neither the dispersed nor continuous phase contains water.

Imhof and Pine studied the stability of non-aqueous emulsions formed between various polar solvents and decane and considered the effects of solvent polarity and hydrogen bonding ability on emulsion stability. [22] Note that in this paper, stability and emulsion breaking was defined based on the time required for 5% of the total volume of dispersed phase droplets to settle or cream from the emulsion. In their work, they tested emulsions formed between decane and water, formamide, N-methylformamide (NMF), N,N'-dimethylformamide (DMF), dimethylsulfoxide (DMSO), methanol, and acetonitrile. In order to account for solvent polarity and hydrogen bonding ability, they compared the dipole moment (μ), relative permittivity (ϵ), and Hildebrand cohesive energy density (δ_H^2), as well as the Kamlet–Taft solvatochromic parameters α , β , and π^* to that of water. α , β , and π^* are non-dimensional and normalized parameters which represent the hydrogen bond donating ability, hydrogen bond accepting ability, and polarity/polarizability of the molecule, respectively. These values are listed in Table 2.3 for the solvents tested by Imhof and Pine. Of the polar solvents tested, only water, formamide, and DMSO formed stable emulsions, taking more than 500 hours in one case for an emulsion formed between formamide and decane, with the use of Brij 52 as a surfactant, to break.

Table 2.3 Solvation parameters of several different polar solvents

Chemical Name	μ (Debye)	ϵ	δ_H^2	α	β	π^*
Water	1.85	80	549	1.17	0.47	1.09
Methanol	1.70	34	205	0.93	0.62	0.60
Formamide	3.73	110	362	1.17	0.18	1.09
NMF	3.83	184	259	0.62	0.80	0.90
DMF	3.86	37	139	0	0.69	0.88
DMSO	3.90	47	169	0	0.76	1.00
Acetonitrile	3.92	38	138	0.19	0.37	0.75

Imhof and Pine theorized that in order to form a stable non-aqueous emulsion using surfactants, the solvent chosen to replace water should resemble water in its physicochemical properties and ability to solvate the surfactant, noting specifically the importance of a solvent's hydrogen bonding ability. Formamide formed the most stable emulsion with decane, other than water, and indeed

resembles water the closest, based on the metrics of Hildebrand cohesive energy density and Kamlet–Taft solvatochromic parameters, as shown in Table 2.3. NMF was only able to form a stable emulsion for a few minutes and DMF was completely unable to form a stable emulsion. Comparing NMF and DMF with formamide, Imhof and Pine noted that the hydrogen bonding ability and number of potential hydrogen bonding sites on the molecule decreases, correlating to the respective decrease in emulsion stability from formamide to NMF to DMF. However, this observation is at odds with the ability of DMSO to form emulsions with decane that were stable for up to 40 hours, given that DMSO lacks the ability to donate hydrogen bonds, as shown in Table 2.3. Imhof and Pine concluded that the stability of non-aqueous emulsions cannot be described by solvation parameters and hydrogen bonding ability alone. [22]

2.4 Reactive Hybrid Rockets Propellants

Traditional hybrid rocket combustion models, like that developed by Marxman and Gilbert, describe the combustion process as diffusion limited. [23] A liquid or gaseous oxidizer injected into the combustion chamber forms a turbulent boundary layer over the surface of the solid fuel. Upon ignition, the combustion reaction provides the heat required to vaporize the fuel and thus sustain combustion, provided the oxidizer continues to flow. A thin turbulent diffusion flame forms within the boundary layer, where the mixture ratio is limited by the rate of diffusion of vaporized fuel species and oxidizer species into the boundary layer. Fig. 2.2 depicts this simplified hybrid rocket combustion model.

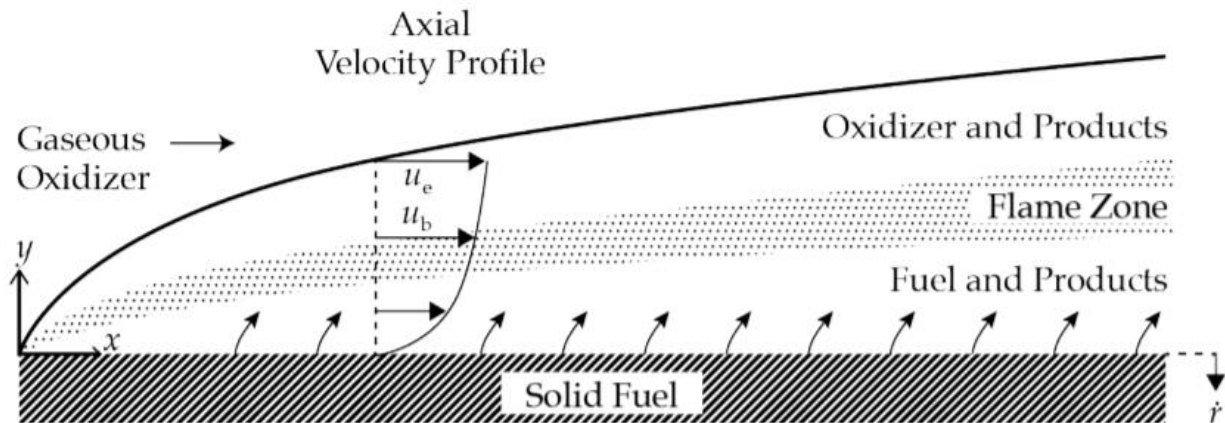


Fig. 2.2 Diffusion-limited combustion of a hybrid rocket motor [24]

The combustion process and mass flowrate of fuel then also depends on the rate of heat transfer from the flame zone to the fuel surface. An increase in the flowrate of oxidizer also increases convective heat transfer to the fuel surface and in turn enhances the rate of fuel vaporization. However, increases in the mass transfer rate of fuel into the flame zone, also termed blowing, can reduce or block the rate of heat transfer to the fuel surface, thus limiting combustion performance enhancements. Marquardt and Majdalani provide a good summary of traditional diffusion-limited hybrid combustion models and their limitations. [24] Liquefying hybrid rocket propellants, such as paraffin wax do not strictly follow the combustion model described by Marxman and Gilbert, as a hydrodynamically unstable, low viscosity melt layer forms on the surface of the fuel during combustion, causing the entrainment of molten fuel droplets, and thus a non-diffusion-limited means of increase the fuel mass flowrate.

Diffusion-limited hybrid rocket propellants, such as HTPB, and liquifying hybrid propellants, such as paraffin wax, could both benefit from the dispersion of a liquid fuel additive within the matrix of each respective solid fuel binder. For polymeric, low regression rate fuels, microexplosions of dispersed liquid droplets could increase the burn surface area and also help to increase the rate of fuel mass transfer to the flame zone. For liquifying hybrid propellants, microexplosions could have the same effects as mentioned for polymeric fuels but could also help to increase mixing and thus improve combustion efficiencies, limiting the amount of unburned fuel leaving the combustion chamber. As mentioned previously however, an increased rate of fuel mass flowrate to the flame

zone can reduce the rate of heat transfer to the fuel surface, and thus microexplosion effects need to be studied further to determine the scope of their benefits to the combustion of hybrid propellants.

An alternative approach to combat the potential drawbacks of blocking the transfer of heat to the fuel surface is to make use of hypergolic propellants. In addition to microexplosions caused by superheating a dispersed volatile hypergolic fuel, the rapid generation of heat at the surface due to spontaneous ignition with a hypergolic oxidizer, could provide further improvements in regression rates and help to disrupt the diffusion-limited combustion regime without a reduction in heat transfer to the solid fuel surface. Hypergolic propellants are defined and described in greater detail below.

2.4.1 Hypergolic Propellants

Hypergolic propellants are combinations of fuel and oxidizer that ignite spontaneously upon contact. Most often, hypergolic propellants are stored as liquids and offer advantages over non-hypergolic propellants due to the simplicity and reliability of ignition. Hydrazine or its derivatives such as monomethyl hydrazine (MMH) and mixed oxides of nitrogen (MON) are common choices for hypergolic fuels and oxidizers, respectively, with reported ignition delays as low as 1 ms and a rich history of use dating back to the 1960s. Benhidjeb-Carayon et al. have studied solid hypergolic fuels as additives to hybrid rocket fuel binders for the purposes of simplifying the ignition system, augmenting regression rate by rapidly generating heat at the fuel grain surface, and demonstrating relight capability in a paraffin-based hybrid rocket motor. [25] A hybrid rocket biphasic dispersion containing a liquid hypergolic fuel dispersed in a solid fuel binder, paired with the use of a hypergolic oxidizer such as nitrogen tetroxide (NTO) or a MON could also be used for the same purposes.

Purdue University has significant experience and knowledge in hypergolic propellants, with over 300 different pairs of fuel and oxidizer tested for hypergolicity and ignition delay. Combining the criteria required for emulsification and our data on hypergolic propellant testing, I selected four hypergolic fuels as potential polar liquid fuel additives to emulsify into paraffin wax and form a hybrid rocket biphasic dispersion that could exhibit augmented combustion performance and help to simplify the ignition scheme of a hybrid rocket system. The fuels chosen include

2,3-dihydrofuran (2,3-DHF), 1,4-dimethylpiperazine (1,4-DMPP), ethylenediamine (ETDA), and triethylamine borane (TEAB). Drop tests are a common means of testing the hypergolicity of propellant combinations and determining their ignition delay. Fig. 2.3 shows a custom optically accessible, temperature controlled, drop test vessel (DTV) created at Purdue University to condense and condition NTO or MON under an inert, pressurized atmosphere for the purposes of testing the hypergolicity of air or moisture sensitive fuels. [26] The DTV dispenses a single drop of oxidizer onto a pool of fuel contained in a small glass vial. Drop tests are filmed using a Vision Research Phantom V1212 high speed camera. Fig. 2.4 shows a series of frames taken from a drop test of MON-25, a mixture of 75 wt.% NTO and 25 wt.% NO, used as an oxidizer, and 2,3-DHF used as a fuel. Time stamps indicate the time from propellant contact. After only 25 ms, the gases produced in the reaction between MON-25 and 2,3-DHF ignite spontaneously and produce a vigorous flame. Table 2.4 shows the molecular structures and ignition delays of all three hypergolic fuels.

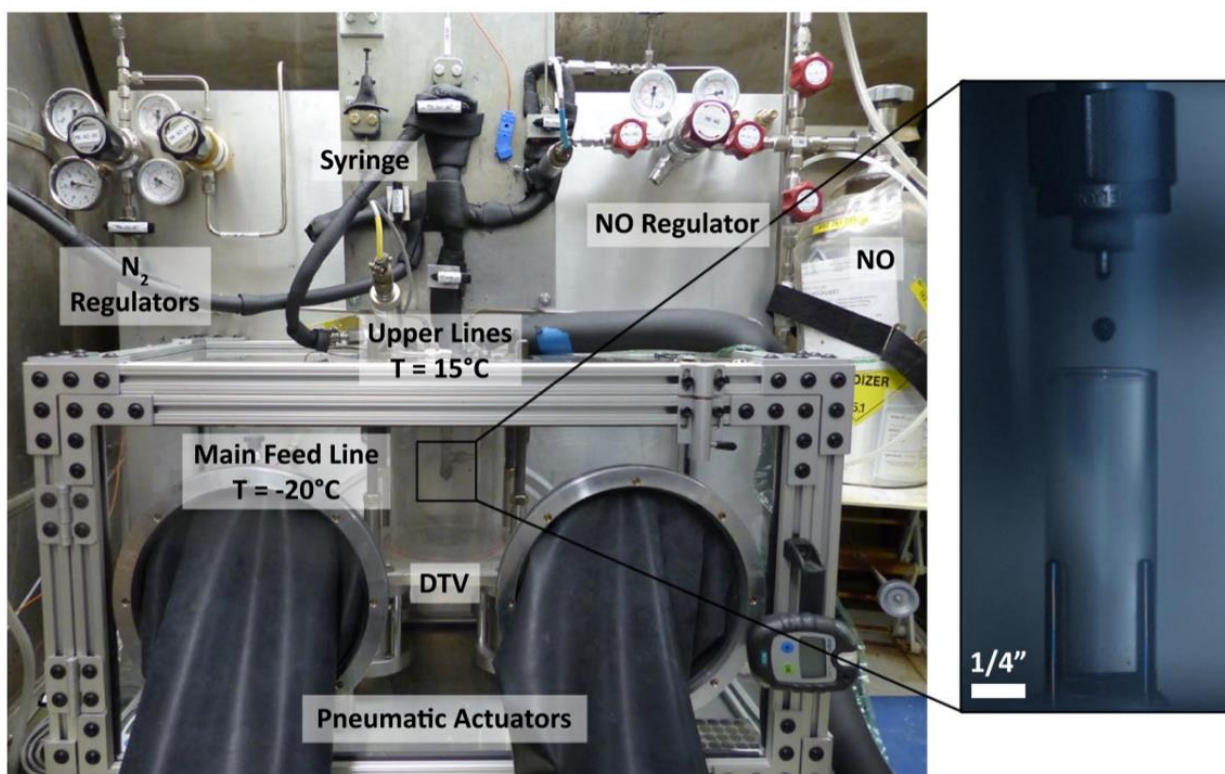


Fig. 2.3 Hypergolic drop test vessel. [26]

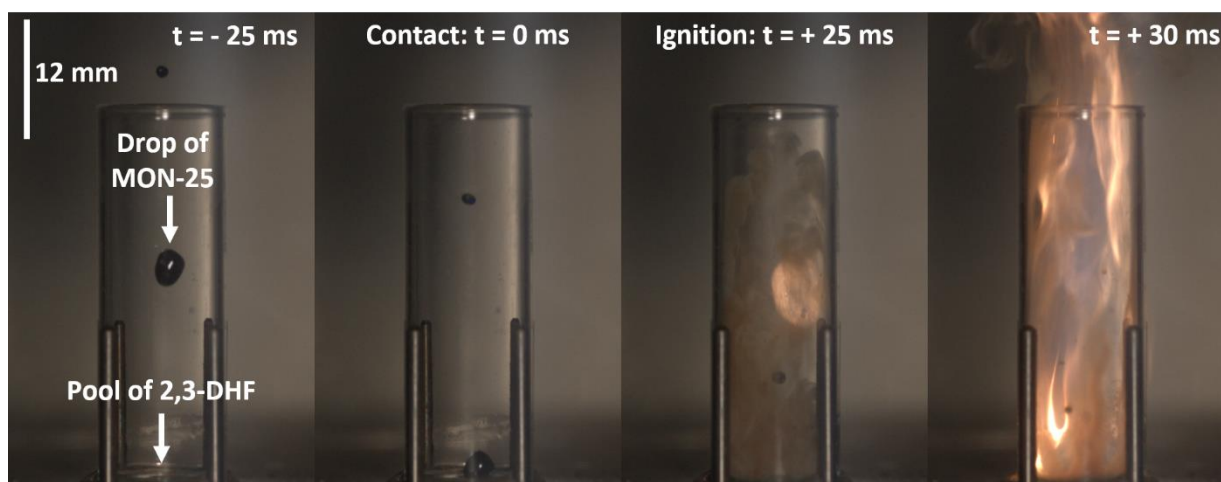
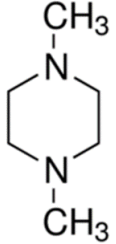
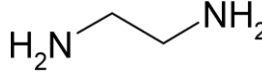
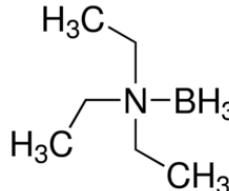


Fig. 2.4 Hypergolic drop test of MON-25 on 2,3-Dihydrofuran. Time stamps indicate time from propellant contact.

Table 2.4 Molecular structure and ignition delay of selected hypergolic fuels.

Chemical Name	Chemical Structure	Minimum Ignition Delay
2,3-Dihydrofuran		20.2 ms*
1,4-Dimethylpiperazine		20.1 ms [‡]
Ethylenediamine		86.6 ms [‡]
Triethylamine Borane		7.5 ms [†]

*Ignition delay tests performed with MON-25 as oxidizer

[‡]Ignition delay tests performed with NTO as oxidizer

[†]Ignition delay tests performed with white fuming nitric acid (WFNA) as oxidizer

2.4.2 Theoretical Performance Gains

In order to compare the theoretical performance of different BDF formulations, I used the NASA Chemical Equilibrium with Applications (CEA) program. For applications to rocket propulsion, CEA is commonly used to predict the performance of various propellant combinations and test conditions [27]. I computed the theoretical performance of seven different hybrid rocket biphasic dispersions and compared them to the baseline performance of neat paraffin wax over a range of mixture ratios, based on the metrics of characteristic velocity, specific impulse, and impulse density. In each test cast, the oxidizer was gaseous oxygen, and fuel formulation consisted of 20 wt.% liquid fuel additive and 80 wt.% paraffin wax. Tests were run for a nominal chamber pressure of 200 psia. Fig. 2.5, Fig. 2.6, and Fig. 2.7 compare the characteristic velocity, sea level specific impulse, and density impulse of each formulation. Table 2.5 compares the peak performance value for each test case. Only three of the liquid fuel additives provide an improvement in propellant characteristic velocity relative to the neat paraffin base case, namely TEAB, ETDA, and 1,4-DMPP. TEAB adds 10 m/s while water and formamide cause significant drops in performance. In terms of sea level specific impulse, the same three liquid additives provide modest improvements in performance while water and formamide reduce performance relative to the base case. However, as Fig. 2.7 shows, a comparison of density impulse between all eight cases tells a different story. Due to the high density of formamide, it is the only experimental case that shows a theoretical boost in performance, with a $5.2 \text{ s} \cdot \text{g}/\text{cm}^3$ increase in density impulse.

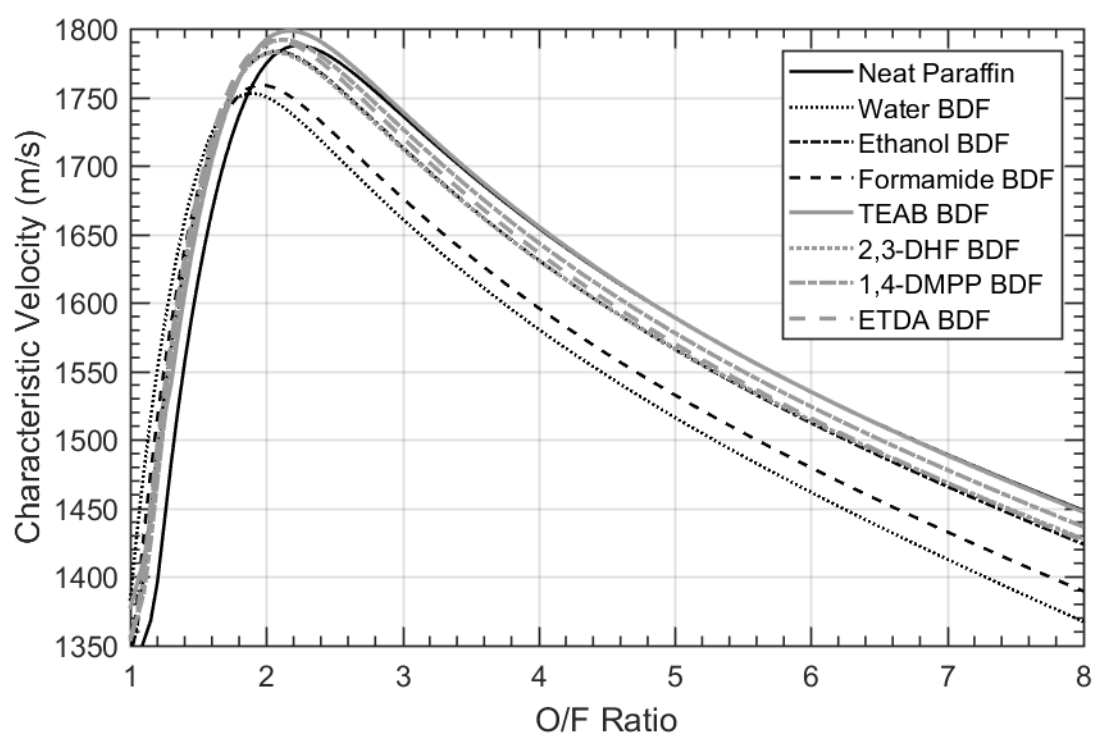


Fig. 2.5 Theoretical characteristic velocities for eight different hybrid fuel formulations.

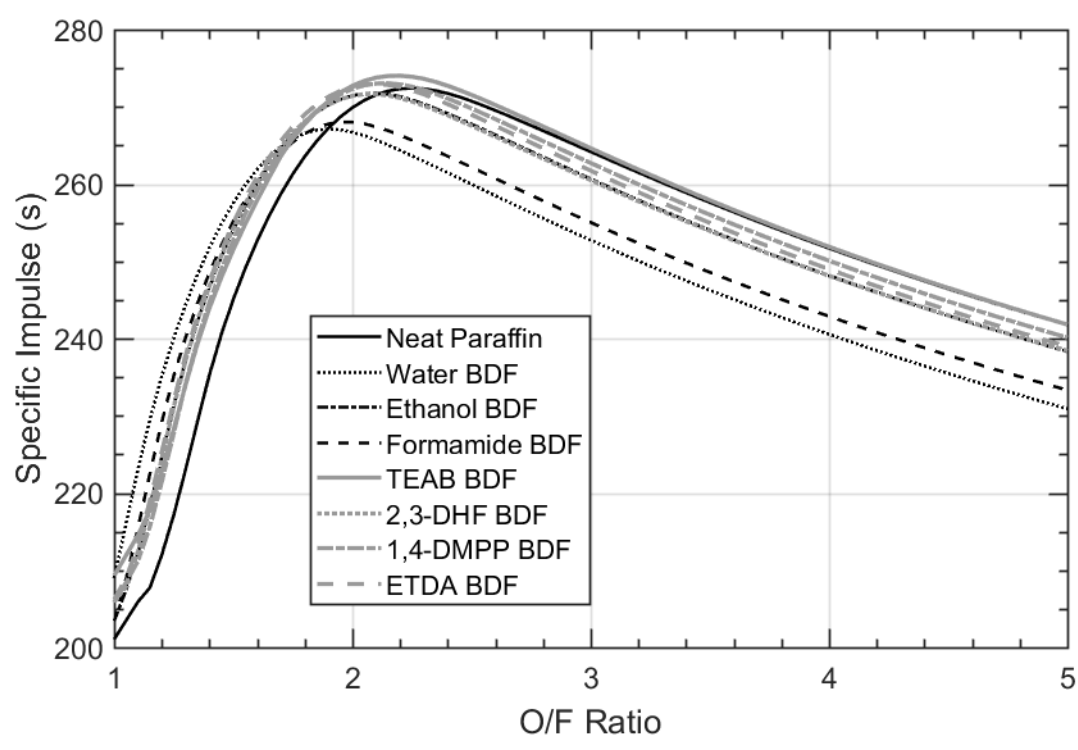


Fig. 2.6 Theoretical sea level specific impulse for eight different hybrid fuel formulations.

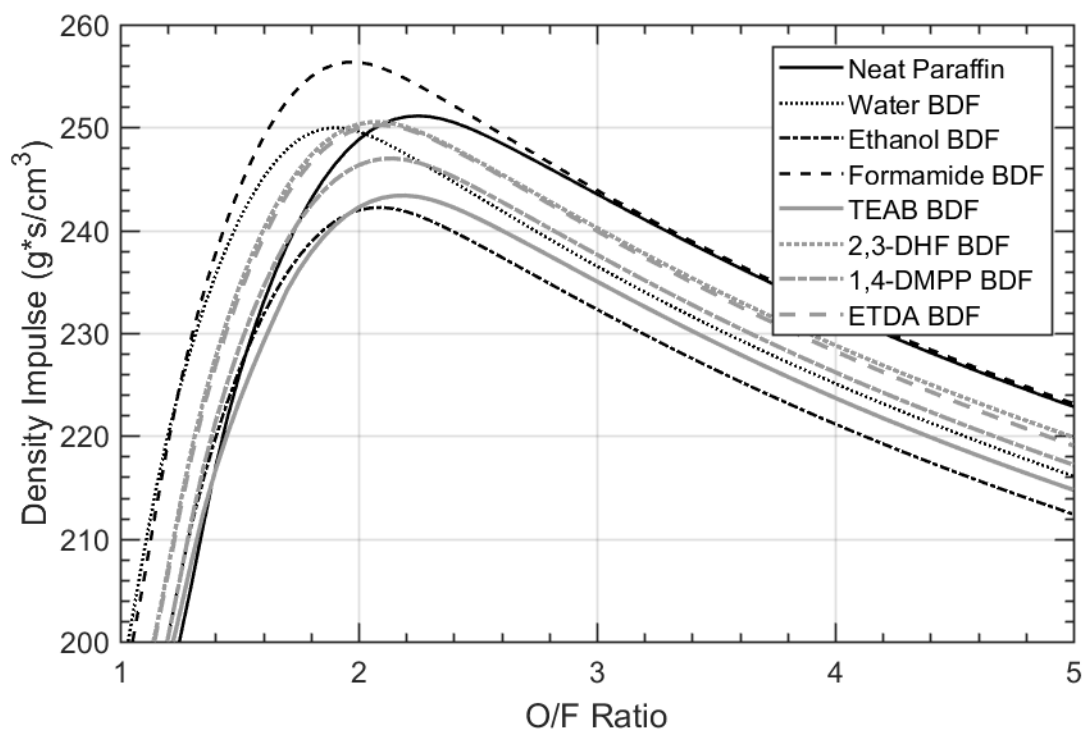


Fig. 2.7 Theoretical sea level density impulse for eight different hybrid fuel formulations.

Table 2.5 Theoretical peak performance values for different BDF formulations. [†]

Liquid fuel additive [‡]	Characteristic Velocity (m/s)	Specific Impulse (s)	Density-Impulse (s·g/cm ³)
None (neat paraffin)	1788	272.4	251.1
Water	1753	267.1	250.0
Ethanol	1783	271.8	242.2
Formamide	1759	268.0	256.3
TEAB	1798	274.0	243.4
2,3-DHF	1783	271.7	250.5
1,4-DMPP	1792	273.1	247.0
Ethylenediamine	1791	273.0	250.2

[†] Peak conditions calculated for sea level, with a nominal chamber pressure of 200 psia

[‡] All BDF formulations calculated assuming 20 wt.% liquid fuel additive and 80 wt.% fuel binder (paraffin wax)

3. EXPERIMENTAL METHDOS

3.1 Component Solubility

As defined previously, emulsions are a specific type of dispersion in which the dispersed and continuous phases are immiscible liquids. For a specific concentration of liquid fuel additive in paraffin wax, the solubility limits determine whether the components will form a solution or a mixture with distinct phases. Thus, the viability of a liquid fuel additive for the purposes of this research is largely dependent on the equilibrium solubility. FR 5560 paraffin wax has a nominal melting point of 69 °C at ambient pressure. [28] Due to the volatility of many of the liquid additives investigated for this research, solubility experiments were performed at elevated pressures to avoid vaporization of the volatile components. I made use of a heavy-walled glass pressure vessel and an acrylic heating bath to maintain the temperature and pressure of the mixtures while also maintaining optical accessibility. An inert gas plumbed into the vial keeps the liquid fuel additives from vaporizing during mixing and a back-pressure regulator maintains a constant pressure. The assembled solubility apparatus is shown in Fig. 3.1.

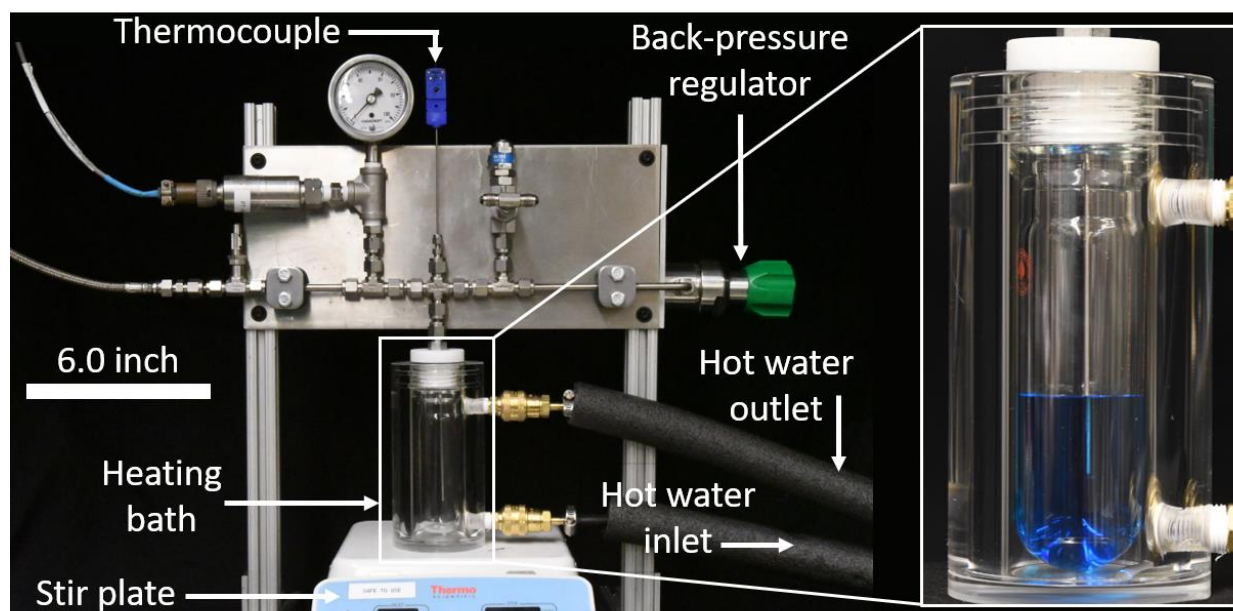


Fig. 3.1 Emulsion component solubility apparatus.

In order to determine the finite solubility ranges of the desired components, incremental changes to the mixture composition and the resulting phase behavior are monitored with photographs. Solubility limits are indicated by the formation of two distinct phases. Below the solubility limit, the bulk phase will completely dissolve the additive, forming one clear solution with no interface. As the solubility limit is approached, the addition of further liquid additive will cause clouding that gradually dissipates with continual mixing. Once the limit is reached, no amount of mixing will reduce the turbidity of the mixture, and eventually droplets of the liquid additive will combine and separate from the bulk, forming an interface and two distinct phases. Solubility experiments were conducted by gradually increasing the concentration of the minor component. Solubility behavior was checked at 1 wt.% increments for each mixture, giving solubility limits with ± 1 wt.% accuracy. Mixtures were maintained at $75 \pm 1^\circ\text{C}$ using an RTE-700 chiller. The temperature was monitored using a type-T thermocouple, with $\pm 2.2^\circ\text{C}$ accuracy (Omega Engineering, Model #: GKMQSS-062G-6) that was immersed in the mixture. Components were mixed by continuous stirring for 30 minutes and checked for solubility. If a clear solution was formed, the concentration of the minor component was increased by 1 wt.%, and the procedures repeated. If the mixture was cloudy or translucent, it was allowed to sit at temperature for up to three hours and checked at 30 minutes intervals for dissolution of the minor component. If an interface formed during this period, the stirring was continued for an additional 30 minutes and the procedures repeated to verify the solubility limit.

3.2 Surfactant Screening and Sample Emulsions

As mentioned previously, finding a surfactant that works well for a specific application requires experimentation. Emulsification of a liquid fuel additive into paraffin wax dictates maintaining an elevated temperature, above the melting point of the wax. This requirement in turn necessitates maintaining an elevated pressure during emulsification to avoid the vaporization and/or boiling of volatile liquid additives. While these requirements have been met for the purposes of synthesizing and casting biphasic dispersion fuel grains, as discussed below in Section 3.5, they increase the complexity and time required for experimental setup, operation, and tear down. In order to more quickly screen for suitable surfactants, I investigated several different oils as potential liquid analogs to paraffin wax. In order to better understand the composition of FR 5560 paraffin wax, I

used gas chromatography mass spectrometry (GC/MS) analysis at the Purdue Institute for Drug Discovery. Analysis indicated an approximately normal distribution of n-alkanes, or fully saturated straight chain hydrocarbons, ranging from $C_{24}H_{50}$ to $C_{41}H_{84}$, with an average carbon number of C_{32} , as shown in Fig. 3.2.

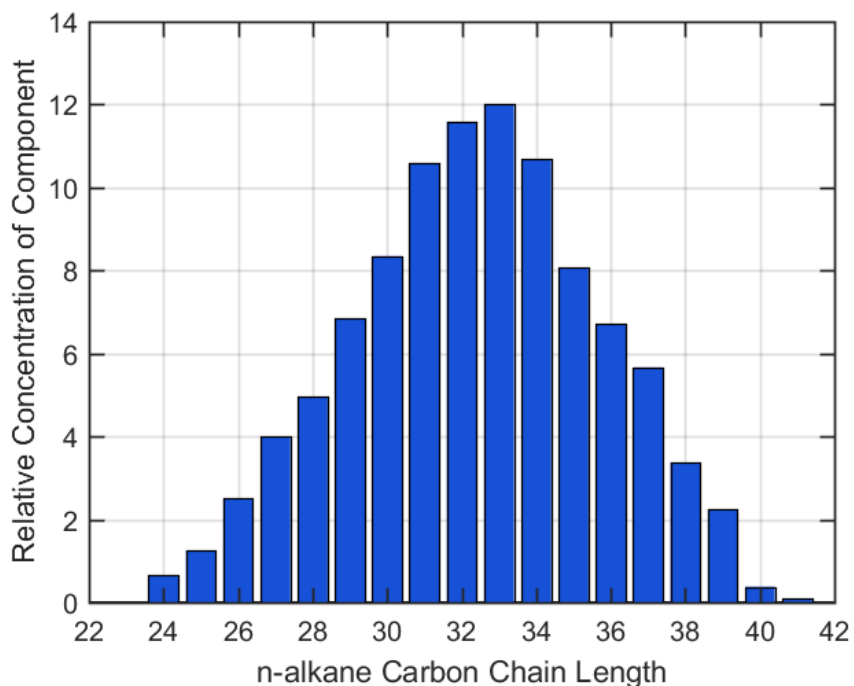


Fig. 3.2 FR 5560 paraffin wax composition as determined by GC/MS analysis

Paraffin oils are liquids that are produced in the process of petroleum distillation, often containing a mixture of light and/or heavy alkanes and branched-chain alkanes that can vary significantly in composition depending on the type of oil used. I purchased two different grades of paraffin oil to test. The first grade of paraffin oil (Sigma Aldrich, CAS #: 8012-95-1) did not come with documentation specifying the chemical composition or source of contaminants. Both GC/GC and GC/MS analysis failed to resolve the individual components and would require a higher temperature GC column to properly analyze the chemical composition. Paraffin oils can contain a significant quantity of naphthenic and/or aromatic compounds that could affect the solubility and other physicochemical properties relevant to emulsions. The second grade of paraffin oil (Resolute Oil, CAS #: 64742-54-7) was a heavy grade paraffin which contained less than 1% aromatics, and

alkanes ranging from C20 to C50. Although this oil came with better documentation, I was again unable to properly resolve the chemical constituents using GC/MS or GC/GC analysis.

I also considered dissolving FR 5560 wax into several different solvents to form mixtures that contained a high percentage of wax to mimic the solubility behavior of neat wax. I purchased Naptha solvent (CAS#: 64742-95-6), Xylene. (CAS# :1330-20-7), Trimethylbenzene (CAS#: 95-63-6), and Toluene (CAS#: 108-88-3). Solvents were heated to dissolve an increasing quantity of paraffin wax, but even at 1 wt.% wax, all mixtures vitrified, completely solidified, or precipitated wax when cooled to room temperature.

Similarly, n-alkanes such as dodecane and hexadecane vitrified at room temperature with only 1 wt.% paraffin wax added. Instead of trying to dissolve paraffin wax into a solvent, I next considered using pure n-alkanes as an analog to paraffin wax. As shown in Figure X, the lowest molecular weight component of FR 5560 is n-tetracosane, C₂₄H₅₀. N-tetracosane has a nominal melting point between 48 and 54°C, and melting point increases as the carbon number of an n-alkane increase. Thus, use of any of the n-alkane constituents of FR 5560 would also require maintaining elevated temperatures while emulsifying components, providing the same difficulties as with the use of the paraffin wax. N-alkanes with lower molecular weights than n-tetracosane would provide an analog to FR 5560 with lower temperature requirements and could even be used at room temperature in the case of n-hexadecane. Unfortunately, pure n-alkanes are expensive, prohibiting the use of large quantities to quickly test different surfactants. For example, hexadecane costs \$70 for 100 mL, octadecane costs \$ 60 for 100 g, and FR 5560 costs \$87.10 for 50 lbs. The recommended minimum mixture volume for the use of an IKA T25 Digital Ultra Turrax homogenizer, which I used to form emulsions as discussed below, is 100 mL. Using octadecane as a liquid analog to paraffin wax would cost roughly \$600 to test ten different surfactants. Additionally, the solubility behavior of liquid fuel additives, such as ethanol, in low molecular weight n-alkanes vary significantly from their behavior in FR 5560. For instance, French et al. reported on the mutual solubility of ethanol and hexadecane at various temperatures. They reported that at 298 K, 31.5 wt.% ethanol dissolved into hexadecane, and that 4.3 wt.% hexadecane dissolved into ethanol [29].

Squalane is a branched, acyclic saturated hydrocarbon with the chemical formula $C_{30}H_{62}$, which is a liquid down to $-38^{\circ}C$ and is significantly cheaper than n-alkanes of a similar molecular weight. In contrast to paraffin oils that contain a wide variety of different compounds, squalane was purchased as a single component, with 99.7% purity (CAS #: 111-01-3). I chose to move forward using squalane as a liquid analog to paraffin wax in order to acquire as much data as possible on the efficacy of different surfactants to stabilize emulsions formed between different polar liquid additives. Emulsions formed between squalane oil and liquid additives were termed sample emulsions to distinguish them from the final formulations that would contain FR 5560 paraffin wax as a continuous phase. The goal was to quickly test all surfactants with each liquid additive, compare their performance, and choose the most effective surfactant to use in the synthesis of hybrid rocket biphasic dispersion fuels.

Sample emulsion were prepared in a similar manner to the biphasic dispersions, with dropwise addition of the liquid additive to the continuous phase while mixing. The procedures are simplified by the fact that squalane is a liquid at room temperature, thus removing the need to work in a heated and pressurized environment. Pictures taken periodically with an LED backlight and analyzed with a photo processing MATLAB code track the interface between emulsified liquid additive droplets and the oil. Fig. 3.3a shows a sample emulsion containing 89.5 wt.% squalane, 10 wt.% water, and 0.5 wt.% of polyethylene glycol oleyl ether used as a surfactant. Note that this surfactant was not effective at preventing emulsion breakdown. In two hours, all the water had separated to the bottom of the glass vessel. In contrast, Fig. 3.3b shows an emulsion prepared in similar fashion, containing the same relative quantities of water and oil, but a more effective surfactant, namely sorbitan monooleate. Emulsified water droplet took six hours to settle one inch through the continuous phase. Samples emulsion components were checked for mutual solubilities in a similar manner to what was described for component solubilities with paraffin wax in Section 3.1.



Fig. 3.3 Sample emulsions formed between water and squalane oil using different surfactants. a) Polyethylene glycol oleyl ether used as a surfactant. b) Sorbitan monooleate used as a surfactant.

3.3 Fuel Binder Emulsions

In order to visually inspect emulsions formed between paraffin wax and different liquid additives, an optically accessible and temperature-controlled apparatus was designed, as shown in Fig. 3.4. All wax emulsions were prepared in a heated and pressurized mixing vessel, as described in greater

detail below. Once mixed, the emulsions were injected into a temperature-controlled glass vessel at elevated pressure to keep all constituents in the liquid phase. Emulsion phase behavior and droplet settling rates were monitored with backlight photography, similar to what was described above for squalane oil sample emulsions. In addition to visually determining which surfactants were most effective in preventing emulsion breaking, the emulsion visualization apparatus provided information on approximately how long I would have to cool and cast biphasic dispersion fuel grains before the components would separate.

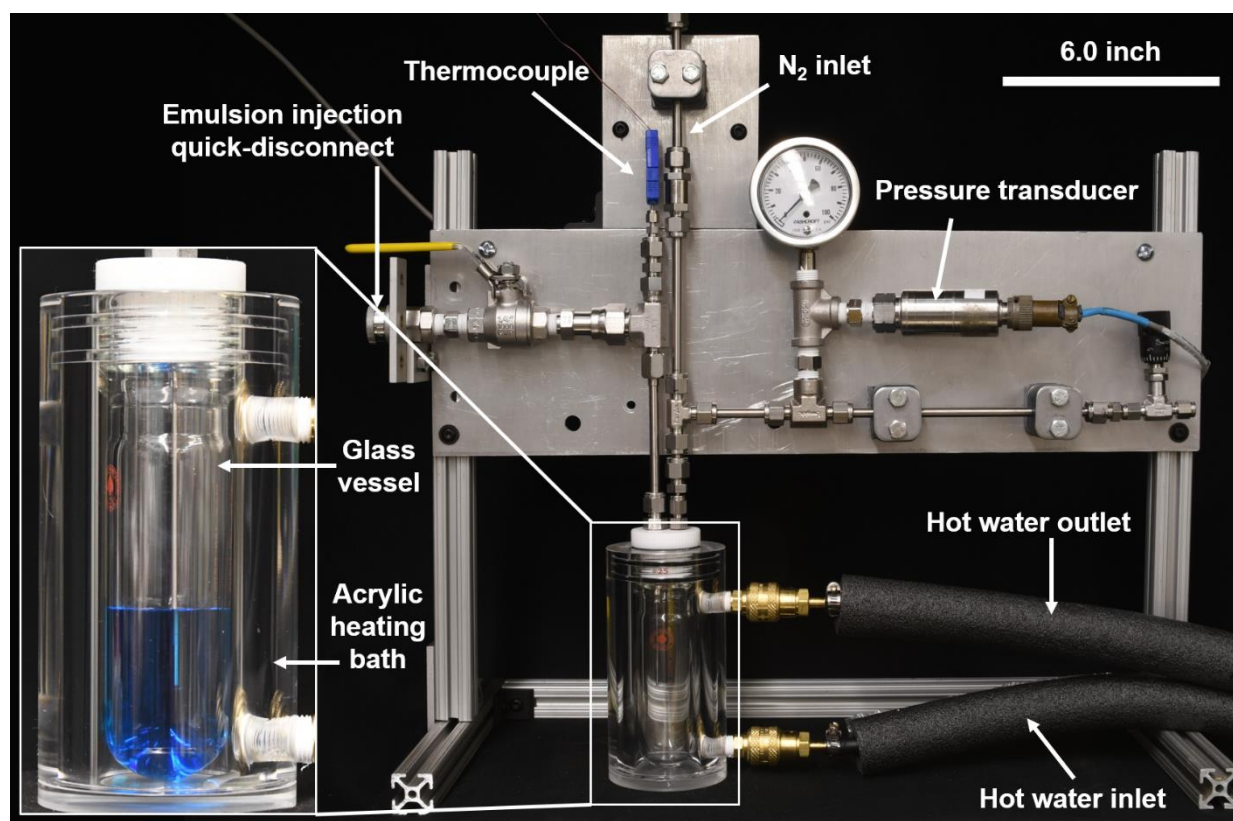


Fig. 3.4 Optically accessible emulsion visualization apparatus.

3.4 Droplet Size Diagnostics and Internal Droplet Structure

Several different techniques have been proposed for the measurement and comparison of emulsion and biphasic dispersion droplet size distributions. From a qualitative standpoint, the use of backlit photography is good for visualizing the changes in emulsion stability over time. In the case of very dilute emulsions, where the dispersed phase comprises less than one percent of the total emulsion volume, or has a volume fraction, ϕ less than 0.01, the dispersed droplet sizes can be estimated

using Stokes' law. Stokes' law describes the motion of a spherical object subject to hydrodynamic and gravitational forces as it travels through a medium. The settling velocity of a spherical object or emulsion droplet, v_o , can then be approximated for low Reynolds number flows as a function of droplet radius, r , continuous phase viscosity, η_c , the local gravitational acceleration, g , and the density difference between the dispersed and continuous phases, $\Delta\rho$, as shown in Eq. 2.

$$v_o = \frac{2 \Delta\rho g r^2}{9 \eta_c} \quad (2)$$

For more concentrated emulsions with dispersed volume fractions between 0.1 and 0.2, Tadros explains that the interaction between droplets causes a deviation from Stokes' law, effectively reducing the droplet settling rate. [19] The adjusted Stokes' settling rate, v , is a function of the emulsion volume fraction, ϕ , and an empirical constant, k , as shown in Eq. 3, where

$$v = v_o (1 - k\phi) \quad (3)$$

Tadros claims that k is on the order of 6.5, meaning that for an emulsion volume fraction of 0.1, the hydrodynamic interaction between droplets reduces the settling velocity by approximately 65%. [19] Souza et al. uses a slightly different empirical correlation developed by Richardson and Zaki to describe the adjusted Stokes' settling velocity for W/O emulsions formed between water and mineral oil at different volume fractions and temperatures, as described by Eq. 4, where n is an empirical exponent with values between 2.3 and 5 [30], [31].

$$v = v_o (1 - \phi)^n \quad (4)$$

In their work, Souza et al. formed emulsions and periodically measured the distance over which the interface between emulsified water droplets and the oil supernatant that formed on top had settled. [30] Samples were imaged on an optical microscope to determine the average droplet size at each period. Using the period over which emulsions settled linearly, Souza et al. determined the empirical exponent, n , and adjusted Stokes' settling velocity, v , for different temperatures and emulsion volume fractions. For instance, emulsions formed between water and mineral oil at 25°C, with a volume fraction of 0.1 exhibited settling velocities 29% lower than that predicted by Stokes'

law for the mean droplet diameters measured using microscopy. A 29% reduction in settling velocity corresponds to an n of 3.22. Such an analysis provides an estimation of the droplet sizes in an emulsion, but still fails to take into account the complex physics and surface chemistry of real emulsions.

In the literature several other techniques are used to determine average emulsion droplet sizes and droplet size distributions. Optical microscopy, briefly mentioned above, provides a straightforward measurement of emulsion droplet sizes. Concentrated emulsions diffract light significantly and in many cases are completely opaque, requiring dilution in order to visualize on an optical microscope. Additionally, emulsion droplets visualized via optical microscopy must be counted and sized manually, or sized using a custom image processing code, which is more tedious than other forms of emulsion droplet sizing. One of the benefits of optical microscopy, in reference to biphasic dispersions, is that a sample can be synthesized, cast, cooled, and then subsequently melted down and diluted with an oil for droplet sizing later. For the present work, emulsion samples were imaged on a HIROX KH-8700 digital microscope with an OL-700 II lens. Individual droplets were counted and sized relative to a calibration scale using a MATLAB image processing code.

Dynamic light scattering (DLS) techniques are commonly used for emulsion droplet sizing and determine the distribution of droplet sizes in an emulsion. Droplet size measurement techniques via DLS quantify the diffusion coefficient of dispersed droplets through the bulk. The diffusion rate of droplets is influenced by their size and the temperature and viscosity of the continuous phase. A detector measures time-dependent laser backscatter from the sample and correlates droplet sizes via an autocorrelation function and the Stokes-Einstein equation (i.e. smaller particles will diffuse faster than larger particles). Similar to the use of an optical microscope for emulsion droplet sizing, DLS techniques require sample dilution. I attempted to make use of a Malvern Nano ZS Zetasizer to determine the average droplet diameter and droplet size distribution of several biphasic dispersions formed between liquid additives and paraffin wax. Samples were melted down and diluted 100 times in squalane oil, and maintained at 60°C. The Nano ZS lists a measurable size range of 0.3 nm to 10 μ m and requires a low polydispersity index (PDI) in order to accurately determine droplet size distributions. The PDI is a dimensional value, often between

0 and 1, that represents the broadness of the size distribution of a sample, formed by fitting the backscatter intensity data to the instrument's autocorrelation function. Small values represent a monodisperse sample, while values larger than 0.7 suggest a broad size distribution and is most likely not well suited to DLS measurements. The Peclet number is a non-dimensional number relevant to emulsions, which expresses the relative influence of gravitational effects and diffusion effects on the behavior of emulsions droplets. Values less than one indicate that diffusion effects and Brownian motion dominate while values greater than one indicate that buoyancy forces dominate. Fig. 3.5 shows a plot of the Peclet number as a function of droplet radius for a biphasic dispersion sample of water in wax, diluted 100 times in squalane, and maintained at a temperature of 60°C. As the plot indicates, hydrodynamic effects quickly exceed diffusion effects as the droplet radius increase beyond 3 μm . DLS measurements did not pass the instrument's quality control due to issues with both a high degree of polydispersity and droplet sedimentation. Droplet images of the same wax samples diluted in squalane, taken on the HIROX microscope indicate a mean droplet diameter of 5 μm , but a high degree of polydispersity, with some droplets as large as 20 μm , which explains why DLS experiments were unsuccessful at providing an accurate measurement.

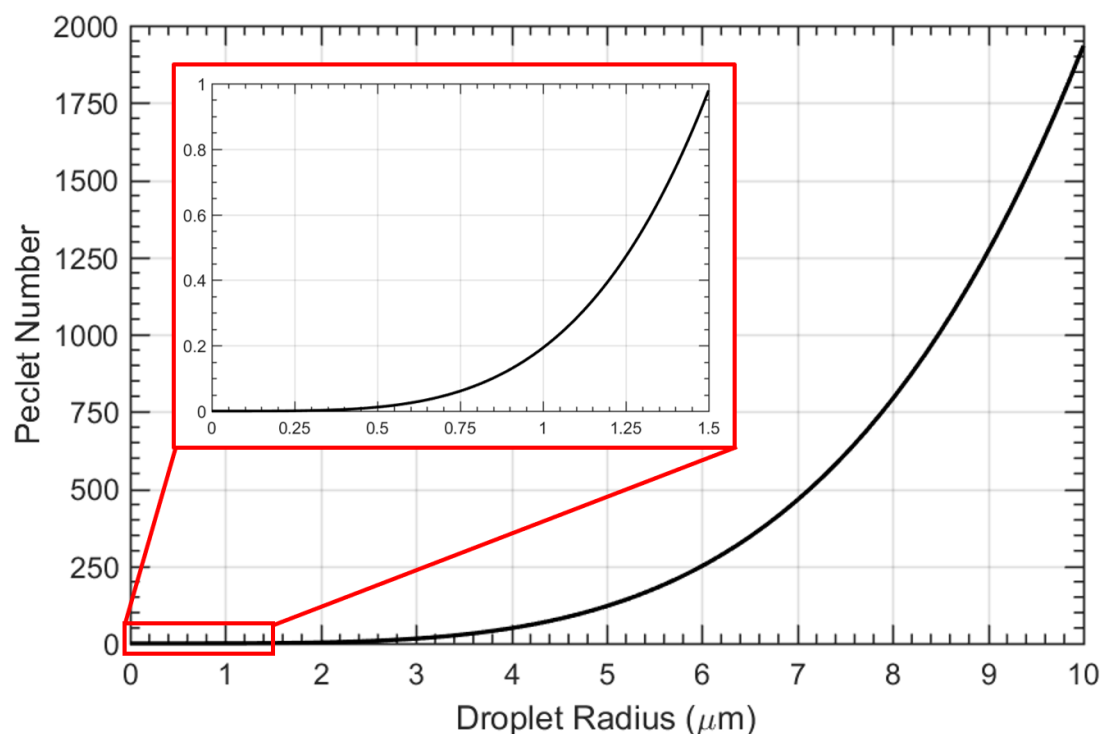


Fig. 3.5 Peclet number as a function of droplet radius for an emulsion of water in squalane oil.

3.5 Biphasic Dispersion Fuels Synthesis and Casting

BDF formulations were prepared by the dropwise addition of the liquid fuel additive into the continuous phase while mixing with an IKA T25 Digital Ultra Turrax homogenizer equipped with a S25KV-25F dispersing tool. A NESLAB RTE-700 chiller was used with a circulating bath to maintain the mixture temperature at 75°C while homogenizing. The continuous phases were prepared by the addition of a surfactant (if any was added) to paraffin wax and continuous stirring at 75°C until all components were dissolved. The dispersed phases were prepared by the addition of surfactant (if any was added) to a liquid fuel additive and continuous stirring at room temperature until all components were dissolved. The continuous phase was added to a mixing vessel and pressurized with nitrogen. Liquid fuel additives were drawn into a 100 mL stainless steel syringe (Harvard Apparatus, Model#: 70-2261), fixed to a test stand, and wrapped with a constant wattage wrap heater (BriskHeat, Model#: BSAT 101008) equipped with a temperature controller to maintain the temperature at 75°C. Liquids fuels were injected from the syringe into the mixing vessel at a constant rate of 20 mL/min using a pneumatic actuator, while stirring the mixture at 10,000 rpm. After injection, the mixture was stirred for an additional five minutes at

15000 rpm. All mixing operations took place at 75°C and 50 psi. Fig. 3.6 shows the plumbing and instrumentation diagram for the BDF synthesis apparatus and Fig. 3.7 shows the assembled test stand.

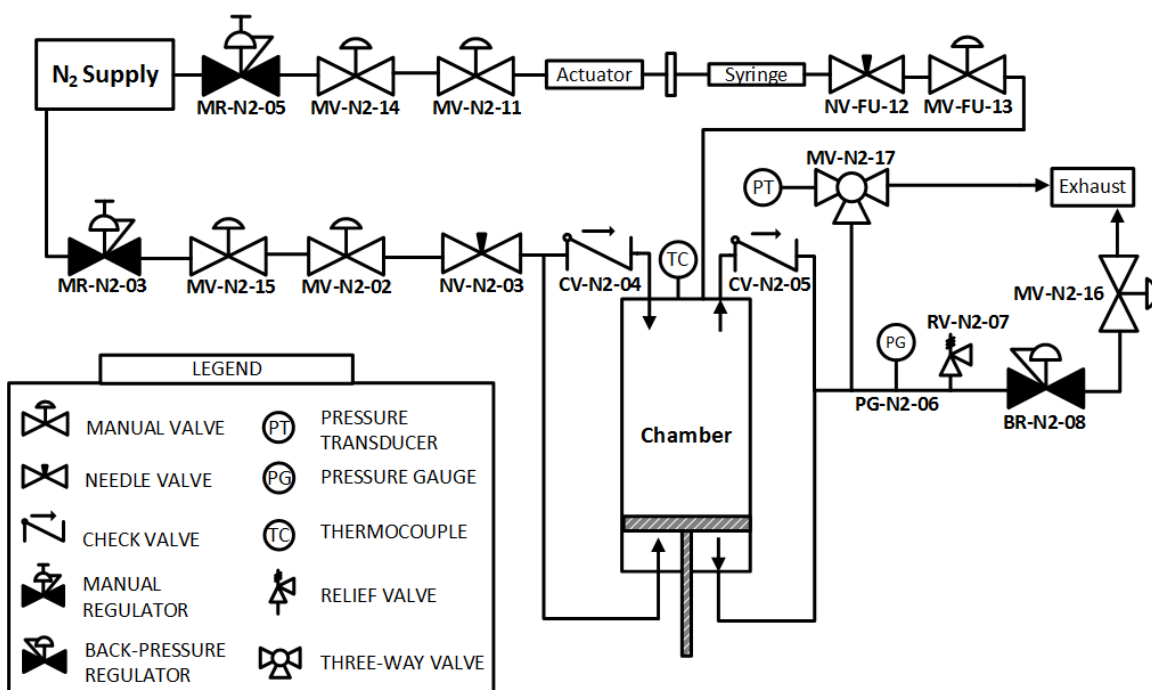


Fig. 3.6 Biphasic dispersion fuel synthesis system plumbing and instrumentation diagram.

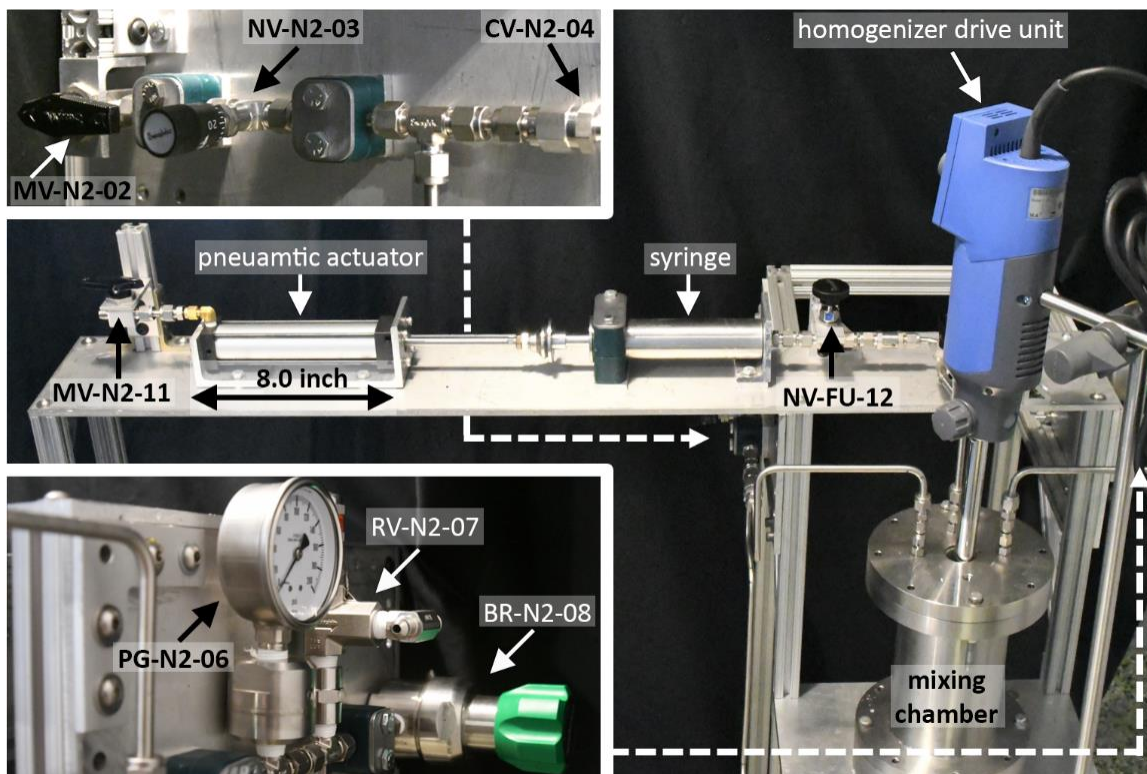


Fig. 3.7 Biphasic dispersion fuel synthesis system. Instrumentation labels match those found in fuel synthesis system plumbing and instrumentation diagram above.

3.5.1 Batch Mixing Vessel and Fuel Grain Synthesis - Design One

One of the major components of the BDF synthesis apparatus is the mixing vessel, which is designed to operate at elevated pressures and temperatures under an inert environment in order to accommodate a wide range of potential volatile and/or moisture sensitive additives. The initial design featured a large, 1 L stainless-steel pressure vessel and a piston fitted with six threaded rods around which fuel grains could be cast. Many of the components for this tube and piston type design are shown in Fig. 3.8. The top flange of the pressure vessel contained five ports to accommodate an inert gas inlet and outlet, a thermocouple, liquid fuel injection, and the homogenizer tool. The piston could be translated upwards to decrease the mixing volume or to remove the synthesized fuel mixture from the pressure vessel using a threaded drive shaft.

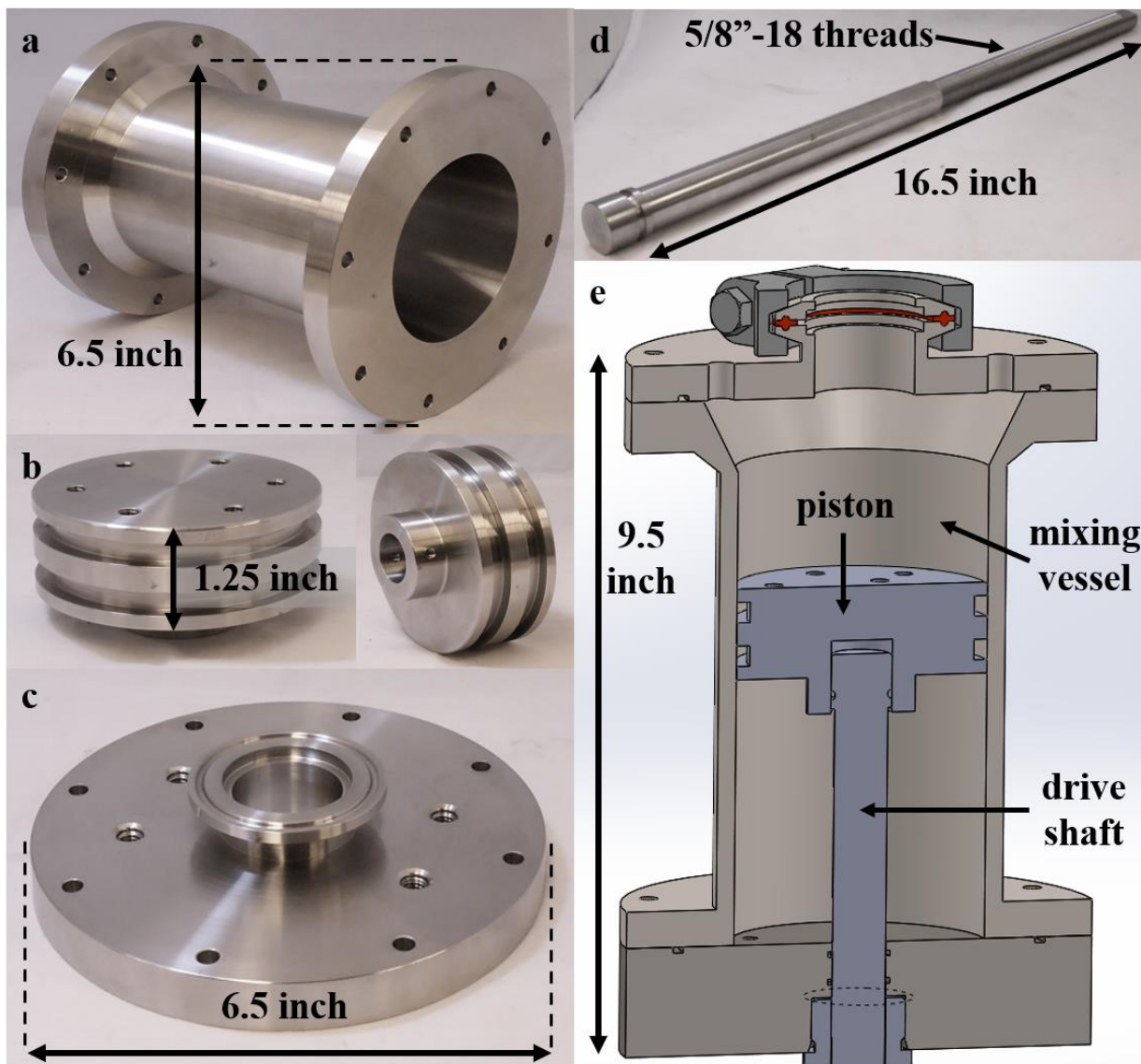


Fig. 3.8 Batch BDF mixing vessel design one. a) Mixing vessel. b) Piston head. c) Top flange. d) Threaded drive shaft. e) CAD rendering of completed assembly.

After all mixing operations were completed, the fuel mixture was cooled to 45° C and the vessel was depressurized. The top flange was replaced with a cutting plate and the piston head was translated upwards slowly to extrude six fuel grains per batch, as shown in Fig. 3.9. However, the extrusion process was difficult to control. During the extrusion process, the mixture continued to cool, requiring an increasing amount of force to translate the piston head upwards. The cutting plate was heated to form a melt layer of wax around the cutting edges and decrease the required

force for extrusion. Ultimately, this process produced non-uniform grains that required reshaping with a heated mold, or in some cases, unusable fuel grains, as shown in Fig. 3.10.

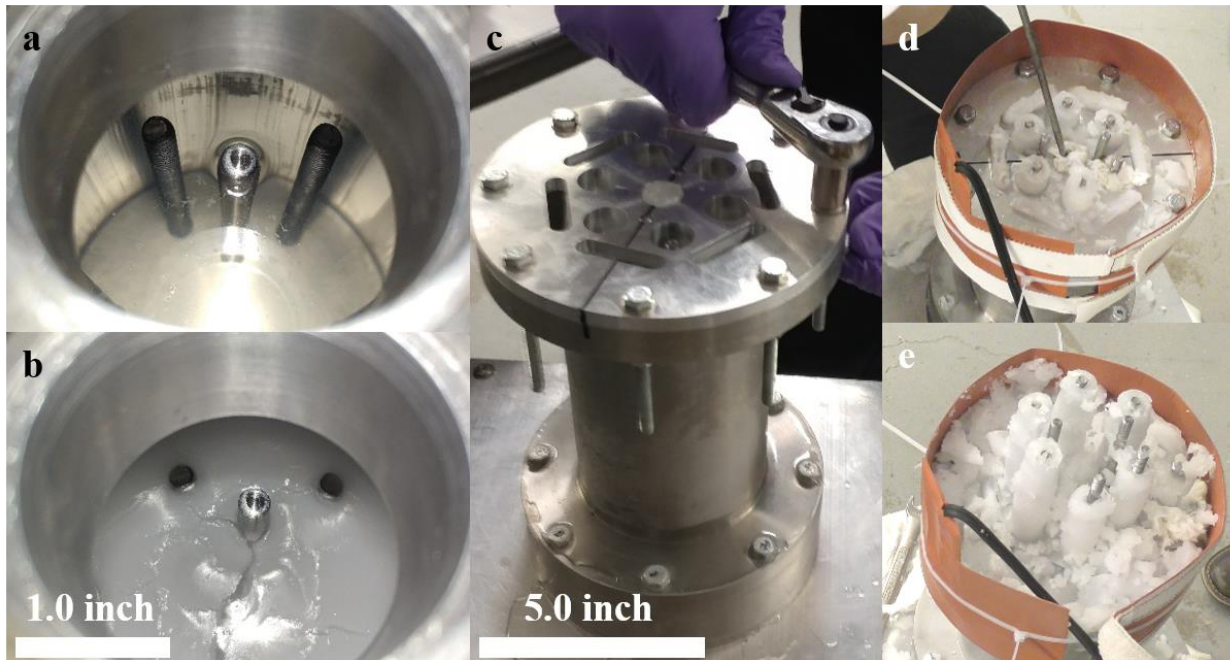


Fig. 3.9 Neat paraffin fuel grain extrusion process. a) Molten paraffin wax in vessel. b) Wax cooled to 45°C in vessel. c) Top flange replaced with cutting plate. d) First inch of fuel grain extrusion. e) Last inch of fuel grain extrusion.

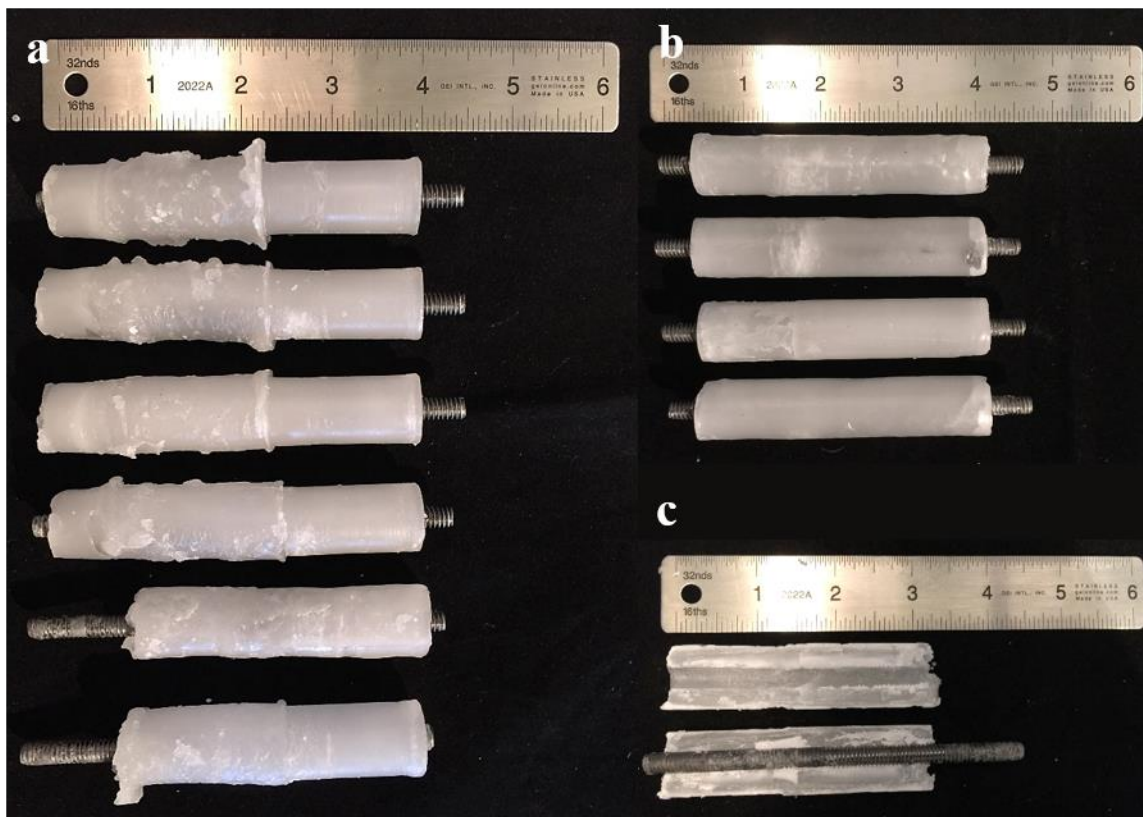


Fig. 3.10 Neat paraffin fuel grains. a) Fuel grains after extrusion. b) Fuel grains after reshaping with a heated mold. c) Cut-view of an extruded fuel grain.

3.5.2 Batch Mixing Vessel and Fuel Grain Synthesis - Design Two

To simplify the fuel grain casting, the second design used individual coring cylinders that could be preheated and hammered into the cooled fuel mixture instead of extruding all six fuel grains at once. The coring cylinders and guide plate are pictured in Fig. 3.11. Note that all synthesis procedures were unchanged between the first and second designs.

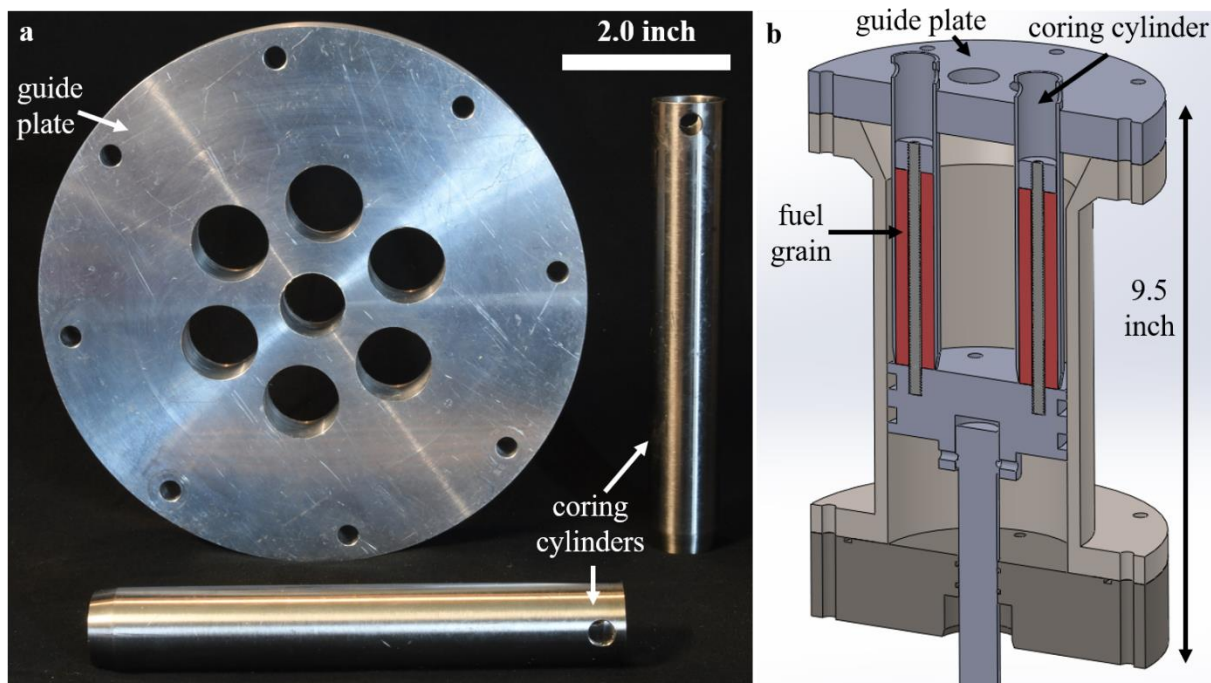


Fig. 3.11 Mixing vessel design two with coring cylinder. a) Guide plate and coring cylinders. b) CAD assembly of mixing chamber with guide plate and coring cylinders in place.

The coring cylinders were more effective at producing uniform, cylindrical fuel grains without additional reshaping, relative to the extruded fuel grains. However, the overall design and operation of the biphasic dispersion fuel synthesis apparatus was complex and inefficient. Each batch operation took several hours to setup, tear down, and clean up for the next test. The heavy-walled pressure vessel and large volume of propellant mix took hours to reach the desired mixing temperature and up to two hours to achieve a uniform temperature during the cooling process. Fuel grain casting was similarly complex in both designs, often resulting in unusable or non-uniform fuel grains. The largest issue with both designs was the time required to cool the fuel mixture to a uniform temperature below the melting point of the paraffin wax. For the purposes of this work, stability is defined as a fuel mixtures ability to resist separation into two distinct phases. Therefore, the time required to adequately cool fuel mixtures to solidify the wax and prevent separation of the dispersed fuel additive is critical. A third batch mixing vessel and casting process was designed in order to simplify fuel grain synthesis, make more efficient use of material, and accelerate the cooling process.

3.5.3 Batch Mixing Vessel and Fuel Grain Synthesis - Design Three

Like the first and second designs, the new mixing vessel was designed to operate in batches, producing multiple fuel grains per batch of fuel mixture. However, rather than in-situ casting, the biphasic dispersion fuel grains are cast by injecting synthesized liquid-fuel-in-wax emulsions directly into a heated and pressurized casting mold. Fig. 3.12 shows the new batch mixing vessel. The new pressure vessel is designed to mix 300 mL per batch, in contrast to the previous 1 L, and uses commercial off the shelf sanitary fittings and compression tube fittings instead of custom-made parts, reducing both the cost and complexity of set-up and cleaning. A stainless-steel ball valve at the bottom of the mixing vessel allows for injection of the fuel mixture into the casting molds after mixing operations.

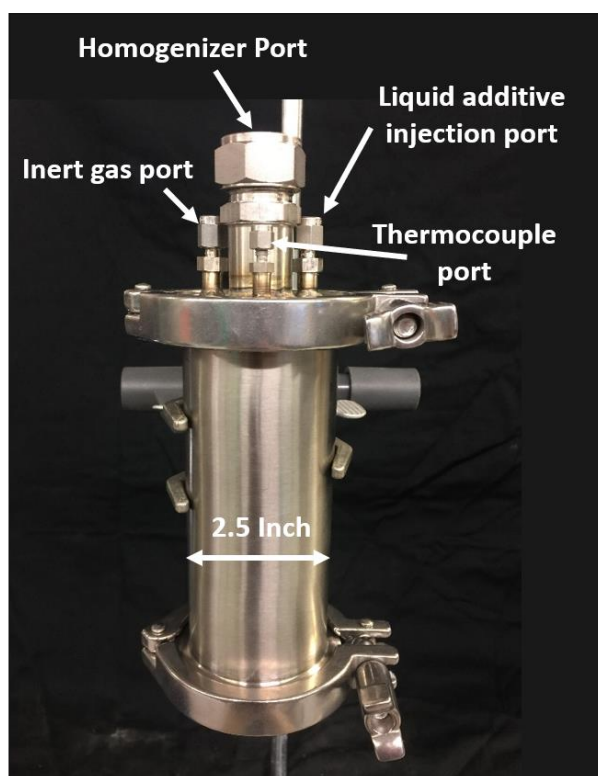


Fig. 3.12 Batch BDF mixing vessel design three.

The new casting mold features two separate grain mold assemblies manifolded together. Prior to mixing, the casting mold assembly is heated and pressurized. Once the fuel components are emulsified, the casting mold assembly is connected to the pressure vessel via quick-disconnect fittings, and the casting mold assembly is slowly vented through a needle valve. The pressure

differential between the casting mold assembly and the mixing vessel draws the liquid fuel mixture into the casting molds. Subsequently, the casting assembly is disconnected from the mixing vessel and plunged into an ice bath to rapidly cool the mixtures. The final version of the casting mold assembly and corresponding plumbing and instrumentation diagram are shown in Fig. 3.13.

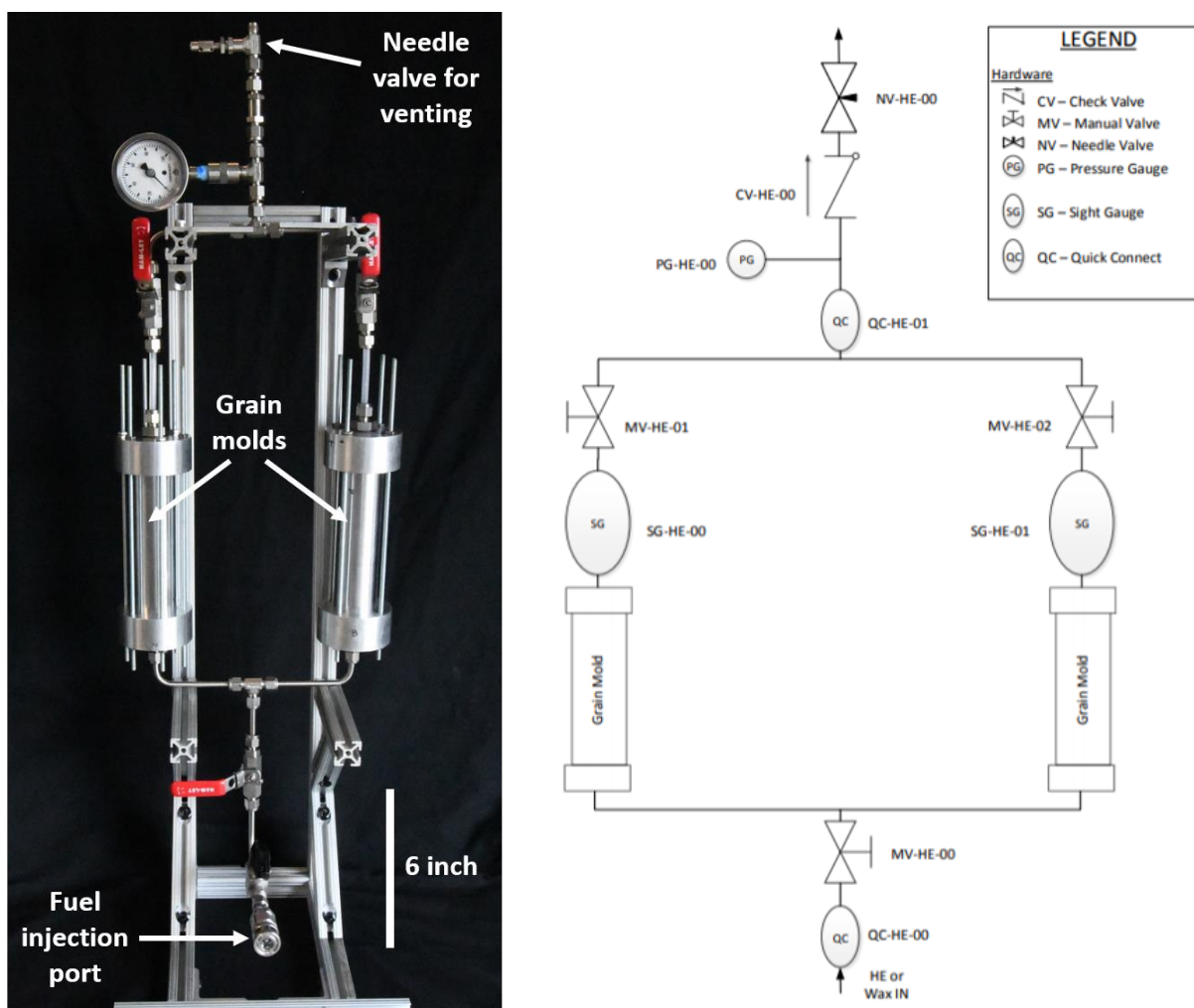


Fig. 3.13 Injection-style fuel grain casting mold assembly.

Void formation due to trapped gases is an inevitable part of casting injected wax-based fuels. The first test cast revealed an issue with the rate of cooling and the orientation of the grain mold during injection and cooling. Liquid paraffin wax was injected into the grain mold assembly horizontally. Despite cooling the wax in a vertical orientation, the time required to fully inject and disconnect the assembly from the mixing vessel was enough to begin solidifying the wax, trapping gas bubbles along the entire surface of the fuel grain, as shown in Fig. 3.14.

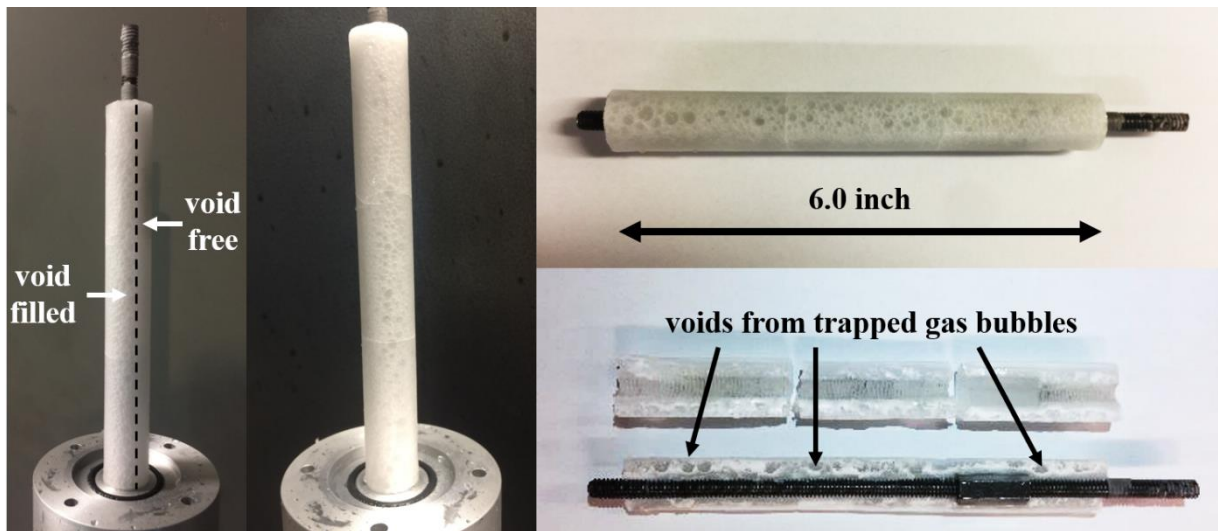


Fig. 3.14 Test cast one. Trapped gas bubbles formed voids during the cooling process.

To prevent void formation, the grain mold assembly was heated to a slightly higher initial temperature, and fuel mixtures were injected and cooled in a vertical orientation for all subsequent casts. On the second test cast, an imperfect connection between the batch mixing vessel and the grain mold assembly via quick-disconnect fittings caused a rapid venting of the grain molds. The resulting larger pressure differential caused a rapid injection of wax into the grain mold rather than a controlled fill, filling the grain mold from the top down, and creating gas pockets throughout the grain, as shown in Fig. 3.15. Time stamps indicate the time from connection of the mixing vessel and the grain mold assembly.

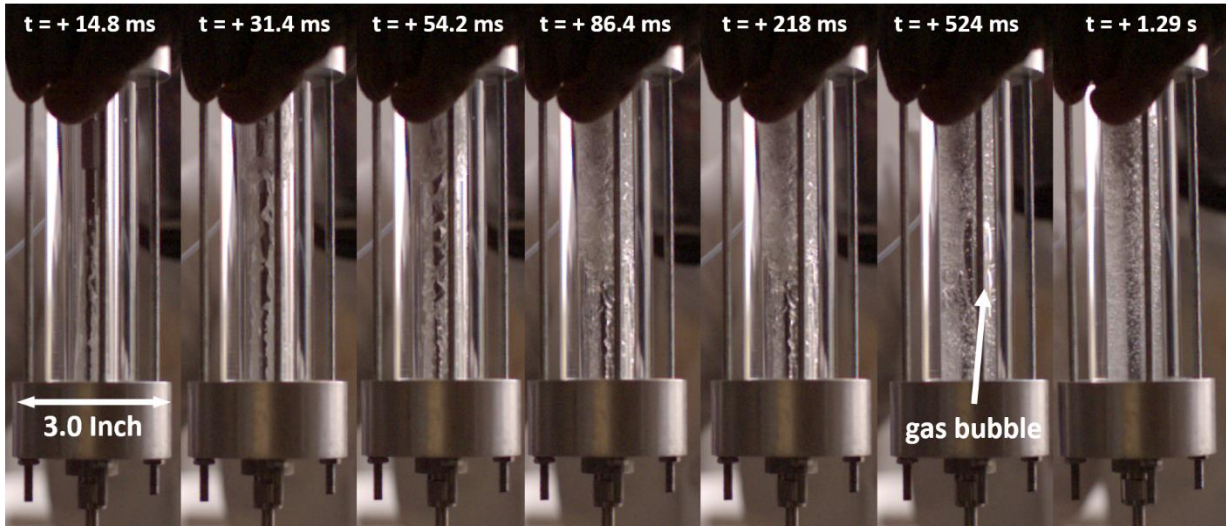


Fig. 3.15 Neat paraffin wax injection test cast two, using an acrylic grain mold for optical accessibility.

To prevent venting pressure from the grain mold assembly prior to filling the mold with an emulsified fuel mixture, I placed a ball-valve between the quick-disconnect fittings and the grain mold. During connection of the grain molds and the mixing vessel, the ball-valve is closed. After a secure connection is made, the ball-valve is opened and the grain molds are slowly vented to fill. Fig. 3.16 shows a neat paraffin fuel grain cast using this new design of the grain mold assembly. The density of the fuel grain was measured as 882 kg/m^3 , or 95.6% of the theoretical density of FR5560 paraffin wax, after the top section containing voids was removed.

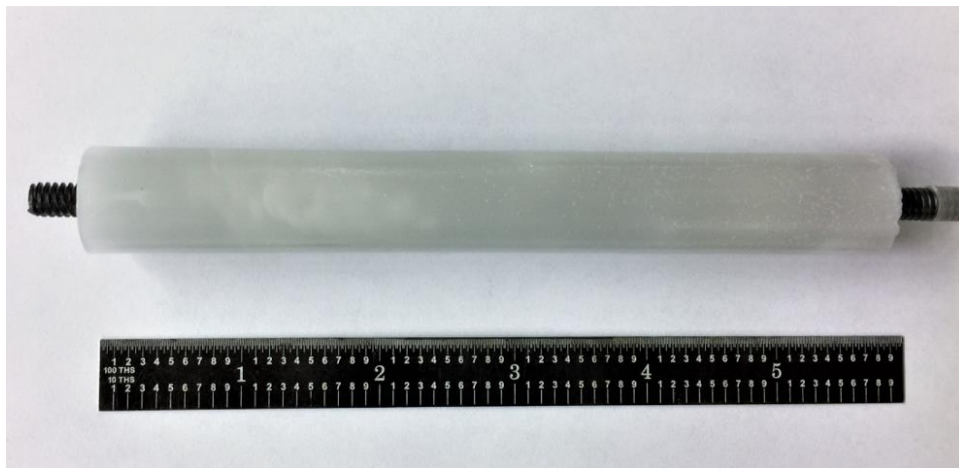


Fig. 3.16 Neat paraffin fuel grain cast using the final design iteration of the injection-style grain mold assembly.

In addition to the plumbing and instrumentation, I performed several design iterations on the casting mold. Experimentation with stainless-steel and aluminum casting molds revealed issues with removing cast fuel grains without deforming their shape. Paraffin wax cooled and adhered to the sides of the mold. Fuel grains needed to be hammered out, sometimes causing cracks or complete separation of the fuel from the center support bolt. Metal grain molds could be heated with a torch to form a thin melt layer to help release the fuel grain. However, it was difficult to control the amount of heat supplied, often resulting in irregular grain shapes, and applying heat to a fuel grain containing a volatile liquid fuel was problematic. Instead, polytetrafluoroethylene (PTFE) grain molds were machined to aid in the release of cast fuel grains. While cast wax did not adhere to the sides of the PTFE molds, the low thermal conductivity of PTFE limited the rate at which fuel grains could be solidified, and PTFE's low buckling strength necessitated the use of a rigid outer aluminum sleeve. With continued issues in forming stable emulsions between liquid additives and paraffin wax, I returned to the use of aluminum casting molds to more quickly solidify fuel grains. Aluminum has a nominal thermal conductivity 600 times greater than that of PTFE. In order to prevent wax adherence, I used a silicone release spray on the interior of the casting mold and machined a slight taper on the inner diameter to aid in fuel grain release. A one-dimensional heat transfer model, built in COMSOL Multiphysics® compares the performance of a PTFE grain mold and an Aluminum 6061 grain mold in their ability to cool and solidify a neat paraffin wax fuel grain, as shown in Fig. 3.17. The heat transfer analysis assumes that all sections of the grain mold are held at 75°C prior to filling, and that the exterior of the mold experiences natural convective cooling in a 0°C ice bath once filled. FR 5560 paraffin wax exhibits significant changes in both density and thermal conductivity during the cooling process from 75°C to room temperature, which is captured in the model using spline interpolation functions. The PTFE grain mold took 12 minutes to solidify the wax and over one hour to bring the wax to room temperature. However, as shown in Fig. 3.17, the aluminum mold cooled the wax below the melting point in under two minutes and brought the fuel grain to room temperature in seven minutes.

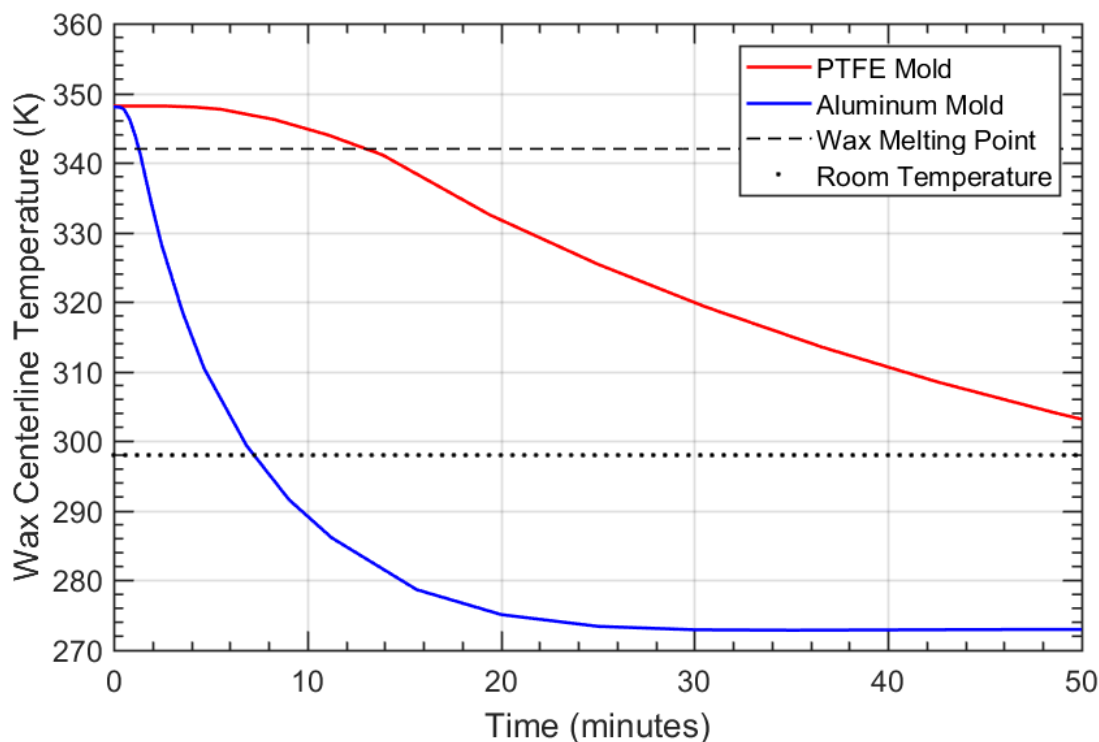


Fig. 3.17 One-dimensional heat transfer analysis of injection-style casting mold design

3.6 Combustion Performance and Data Analysis

The regression rates and combustion efficiencies of biphasic dispersion fuel grains were obtained using an optically accessible hybrid rocket combustor (OCC). The OCC, described in detail by Shark et al. [32], makes use of a water-cooled nozzle assembly and quartz lined acrylic combustion chamber capable of operating at steady-state chamber pressures of up to 250 psia, as well as a Flowmaxx Engineering sonic orifice to control the oxidizer mass flowrate. The optical accessibility allows for instantaneous measurement of the fuel grain diameter throughout each test, with the use of a Vision Research Phantom V1212 coupled with an Infinity DistaMax K2 lens. A CAD drawing of the OCC assembly is shown in Fig. 3. A National Instruments LabVIEW virtual instrument (VI) controls all valves and instrumentation. The flow of gaseous oxygen begins one tenth of a second prior to the ignition of an electronic match (MJG Firewire Initiator) and the oxygen run valve closes one second after ignition. Each fuel grain measures 0.75 inches in diameter and 3.5 inches in length, nominally. The fuel grains are cast around steel bolts and

threaded into the oxidizer injector face. Application of a high-temperature silicone caulk inhibits fuel grain end burning. The oxygen feed pressure is measured upstream of the sonic orifice with a 0-3000 psi high accuracy pressure transducer, with $\pm 0.05\%$ full scale output (FSO) accuracy (GP:50 NY Ltd., Model #: 241). The oxygen injection pressure is measured upstream of the injector face with a 0-500 psia pressure transducer, with $\pm 0.04\%$ FSO accuracy (GE, Model #: UNIK 5000). Chamber pressure measurements are made with a 0-500 psia pressure transducer, with $\pm 0.04\%$ FSO accuracy (Druck, Model #: PMP 1260). A 1/16-inch type K thermocouple measures the temperature of the oxygen fed into the system, upstream of the sonic orifice, with $\pm 2.2^\circ\text{C}$ accuracy (Omega Engineering, Model #: CASS-116K 12). Thrust measurements are made using an Interface 1210, 0 to 1000 lbf load cell with $\pm 0.04\%$ FSO accuracy. All pressure, temperature, and thrust data are recorded at a 1000 Hz sampling rate.

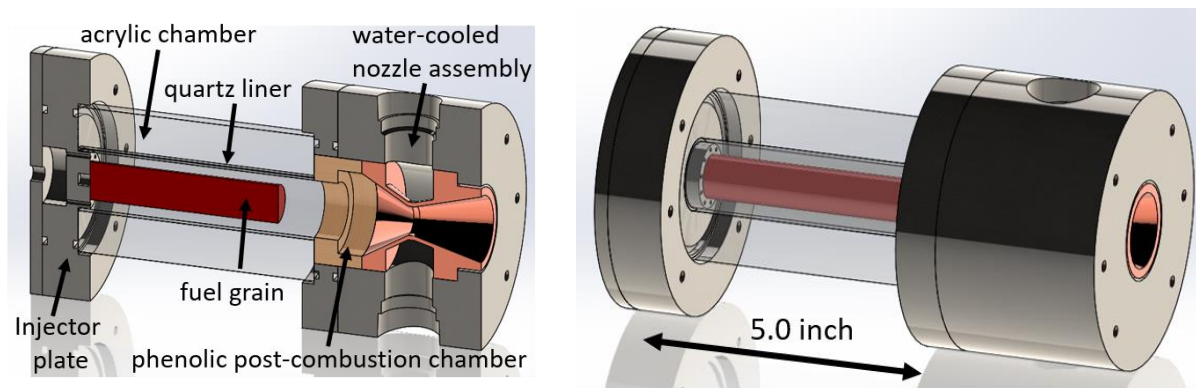


Fig. 3.18 Optically accessible hybrid rocket motor design and components

High-speed videos are recorded at frame rates between 10000 and 15000 frames per second and processed using a MATLAB code to determine the time and spatially averaged fuel grain diameter at prescribed time intervals. The space-time-average regression rate over the duration of the test is calculated as half of the change in fuel grain diameter over the tracked test duration. Calibration images taken prior to each test set the scale for each video in terms of millimeters per pixel. Fig. 3.19 depicts a neat paraffin combustion test in the OCC. Recirculation near the injector face causes the fuel grains to burn more quickly near the head end, as shown in Fig. 3.20. To avoid errors associated with non-uniform combustion, all reported regression rates are measured downstream of the recirculation zone.

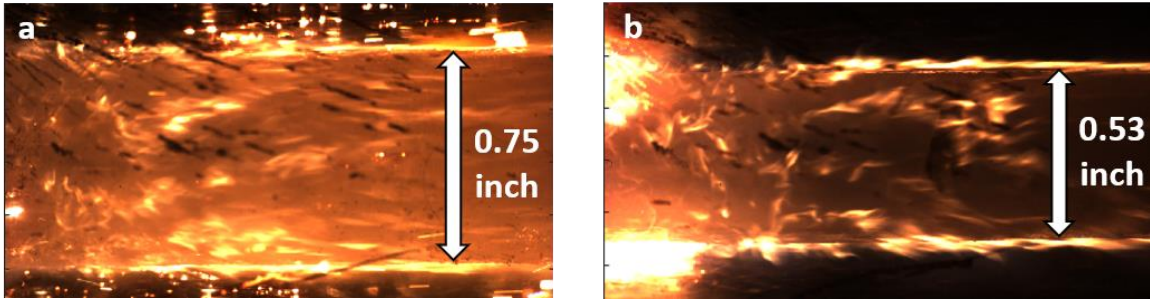


Fig. 3.19 Combustion of a neat paraffin fuel grain in the OCC. Flow is from left to right. a) 0.025 seconds after ignition. b) 0.950 seconds after ignition.

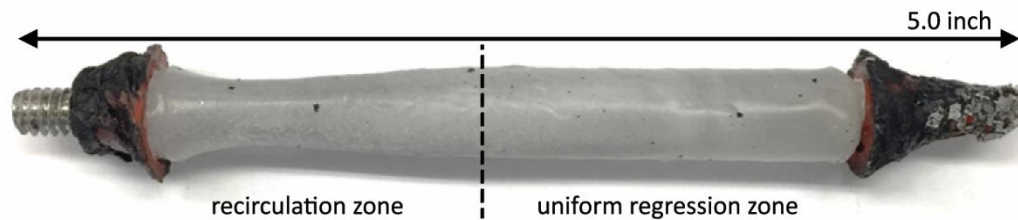


Fig. 3.20 Neat paraffin fuel grain after a combustion test in the OCC. Flow is from left to right

Oxygen stagnation properties, P_0 and T_0 , measured upstream of the sonic orifice, in addition to the known orifice discharge coefficient C_D , and throat diameter, D_t were used to calculate the oxidizer mass flowrate according to Eq. (3 24), as described in the work of Sutton et al. [33]. The ratio of specific heats for oxygen, γ , is calculated using the NIST Webbook Thermophysical Properties library at the measured upstream conditions. [17] In addition to calculating the fuel regression rate, characteristic velocity values were calculated for each test according to Eq. (5), where A_t represents the nozzle throat area, \bar{P}_c is the average chamber pressure, t_b is the burn duration, and Δm_{ox} and Δm_f represent the total mass of oxidizer and fuel consumed during a test.

$$C^* = \frac{A_t \bar{P}_c}{(\Delta m_{ox} + \Delta m_f)} t_b \quad (5)$$

Theoretical maximum characteristic velocities are calculated at the test conditions using the NASA Chemical Equilibrium Analysis code (CEA) [27]. CEA calculates the maximum theoretical characteristic velocity as a function of the oxidizer-to-fuel (O/F) ratio. In this application, the O/F ratio represents the ratio of the total mass of oxidizer fed into the combustor and the total mass of

fuel consumed for the burn duration. A ratio of the calculated characteristic velocity and maximum theoretical value serves as a measurement of the combustion efficiency for each test. Two different methods were used to measure the fuel mass flowrate, depending on the test. For nominal conditions, the fuel grains were massed before and after testing. The difference in mass, or total mass of fuel consumed, divided by the burn duration of each test serves as a measure of the fuel mass flowrate that accounts for the non-uniform regression rate, as shown in Fig. 3.20. However, in some situations, the fuel remaining after a given test retained sufficient heat to melt off of the center support bolt, preventing an accurate post-test weight. In this situation, the total mass of fuel consumed during the burn duration, Δm_f , was calculated using the measured fuel density and the change in fuel diameter, as recorded in the high-speed videos, assuming a uniform regression along the entire surface of the fuel grain. Due to the uncertainty associated with measuring the fuel mass flowrate and accounting for the non-uniform regression, the combustion efficiency measurements serve only as a relative comparison between different fuel formulations.

For the present work, all error bars were determined following the uncertainty analysis procedure described by Coleman and Steele. [34] As an example, the experimental measurement of the oxidizer mass flowrate, \dot{m}_{ox} , can be described as a function of five measured or calculated variables, C_D , P_0 , T_0 , A_t , and k . The relative uncertainty of \dot{m}_{ox} is then calculated using the uncertainty magnification factor and relative uncertainty of each of the five measured variables. All error bars are displayed as calculated uncertainties, which can be defined as the relative uncertainty multiplied by the measured value of the experimental result.

4. RESULTS AND DISCUSSION

4.1 Liquid Fuel Additives and Surfactant Screening

Three different liquid fuel additives were chosen for the purposes of forming biphasic dispersion fuel grains with FR 5560 paraffin wax in order to study the effect of dispersed liquid fuel droplets on the combustion performance of hybrid fuels, relative to neat hybrid fuel binders. Despite the theoretical promise of volatile, hydrogen-rich hypergols such as 2,3-dihydrofuran and ethylenediamine for use in a hybrid rocket BDF, safety and cost concerns limited the scope of the current research to include water, ethanol, and formamide as three potential additives. These three additives were chosen to provide a baseline combustion performance comparison between neat paraffin fuels and paraffin based BDFs. Water provides a useful non-reactive comparison to ethanol and formamide, helping to isolate the effect of microexplosions on the combustion performance of hybrid rocket fuels, without the added benefit of a liquid fuel additive's heat of combustion. Ethanol was chosen due to its low cost, low superheat limit, and its capacity to exhibit microexplosions, as was shown by Lasheras et al. when emulsified into various n-alkanes. [11] While formamide does possess some toxicity relative to water and ethanol, its vapor pressure is low, even at the nominal mixing temperature of 75°C, reducing the likelihood of exposure and the necessary precautions. [35] Formamide is inexpensive, has been shown to produce stable non-aqueous emulsions in various n-alkanes [22], [36] and also possesses the highest theoretical density-specific impulse of any liquid fuel additive considered for this research. Thus water, ethanol and formamide were chosen to gain a knowledge base surrounding biphasic dispersion synthesis, casting, and testing prior to moving forward with more exotic additives.

4.2 Liquid Fuel Additive Solubility Experiments

Water, ethanol, and formamide were tested for their mutual solubilities with paraffin wax at 75°C. The results of the solubility tests for water, ethanol, and formamide are shown in Fig. 4.1, Fig. 4.2, and Fig. 4.3 respectively. Data points indicate the specific concentrations of liquid fuel additive tested using the solubility apparatus. Solubility behavior was checked at 1 wt.% increments for each mixture. The shaded region indicates the concentration ranges in which the components are no longer soluble. 1 wt.% water added to paraffin wax did not completely dissolve and individual

water droplets coalesced, forming a clear interface between the water and wax after three hours. Similarly, 1 wt.% wax did not completely dissolve into water, forming a clear interface after mixing the two components.

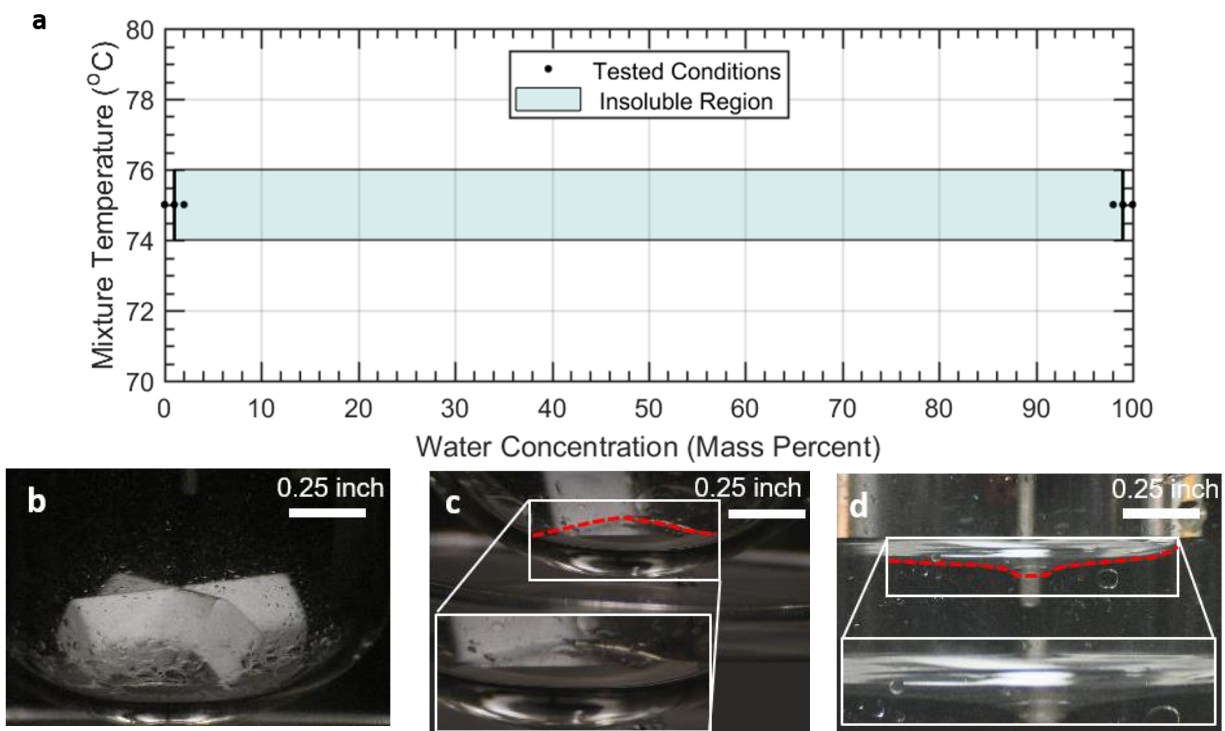


Fig. 4.1 Mutual solubilities of FR 5560 paraffin wax and water at 75°C. a) Solubility plot. b) 1 wt.% water in wax, after stirring. c) 1 wt.% water in wax after three hours. d) 1 wt.% wax in water after stirring and waiting three hours.

Ethanol solubility was monitored, starting with a 1 wt.% addition of ethanol to wax. Each incremental increase in the ethanol concentration, through 7 wt.% ethanol, formed a clear solution. 8 wt.% ethanol in wax, after mixing, formed a cloudy mixture that cleared after 3 hours of storage. The addition of more ethanol formed cloudy mixtures that did not completely clear, and eventually formed an interface at the top of the vial. 1 wt.% wax added to ethanol completely dissolved, but a clear interface was formed after the addition of further wax.

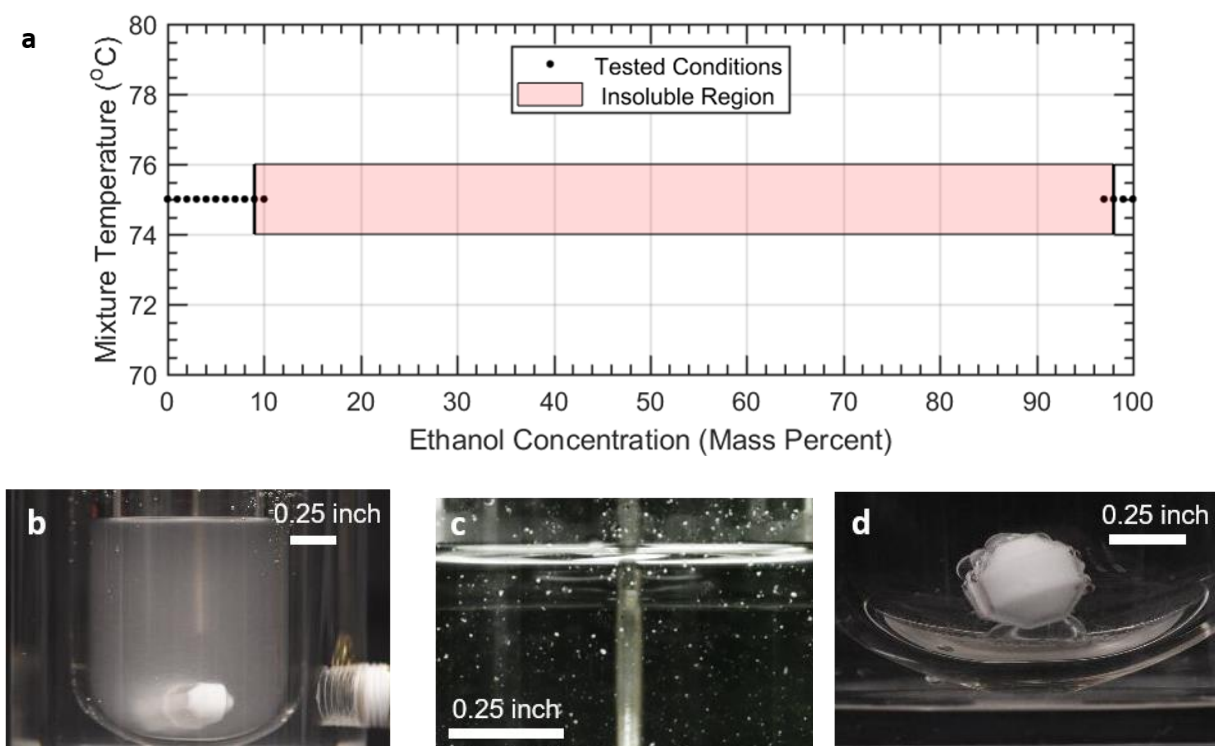


Fig. 4.2 Mutual solubilities of FR 5560 paraffin wax and ethanol at 75°C. a) Solubility plot. b) 9 wt.% ethanol in wax, after stirring. c) 9 wt.% ethanol in wax after three hours. d) 2 wt.% wax in ethanol after stirring.

Formamide solubility experiments were conducted in similar fashion. 1 wt.% formamide completely dissolved into wax, but 2 wt.% formamide in wax did not form a solution. Formamide droplets coalesced and settled to the bottom of the vessel after one hour of storage. 1 wt.% wax in formamide did not form a solution, but instead formed a clear interface between the two fluids after mixing.

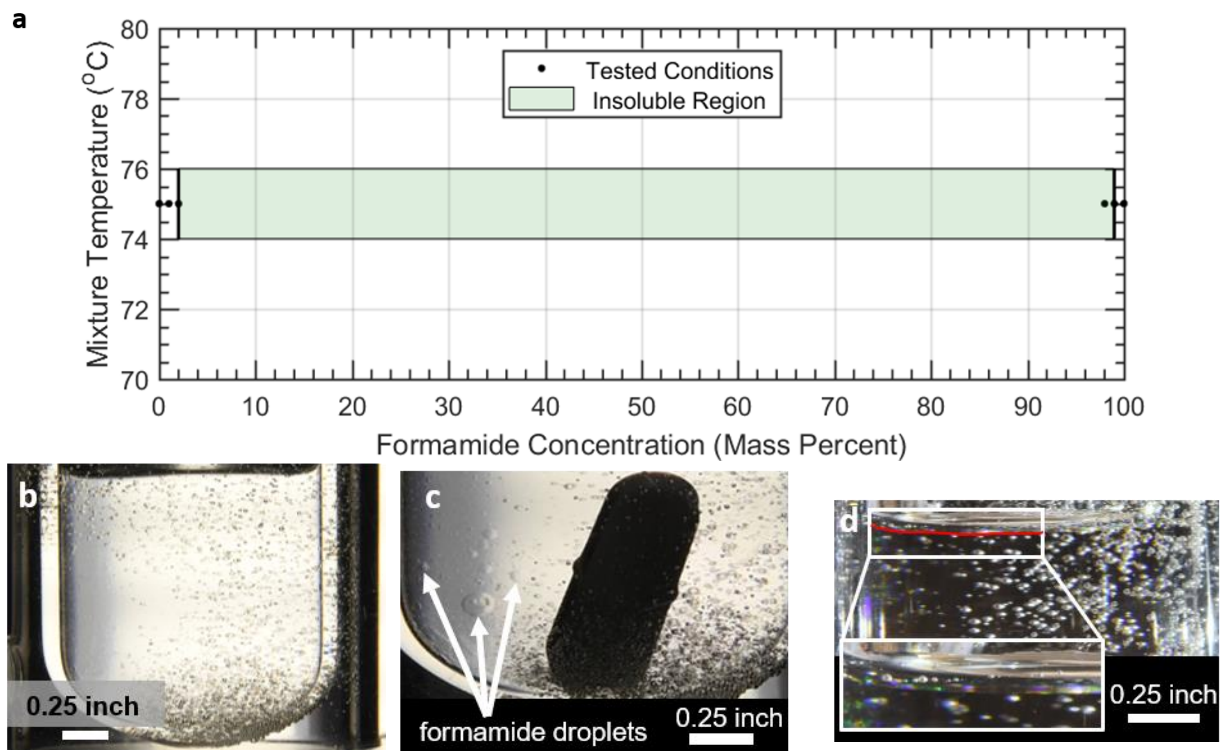


Fig. 4.3 Mutual solubilities of FR 5560 paraffin wax and formamide at 75°C. a) Solubility plot. b) 2 wt.% formamide in wax, after stirring. c) 2 wt.% formamide in wax after one hour. d) 1 wt.% wax in formamide after stirring.

Water and ethanol were tested for their mutual solubilities with squalane at 25°C since squalane was used as a continuous phase for sample emulsions. The results are expressed in Fig. 4.4 and Fig. 4.5. Like the solubility of water and wax, 1 wt.% water added to squalane oil did not form a solution, and 1 wt.% oil added to water did not form a solution. However, both mixtures clouded after mixing, and took several hours for a clear interface to form between the two fluids. 1 wt.% and 2 wt.% ethanol added to oil completely dissolved, but 3 wt.% ethanol did not. After six hours of storage, the mixture did not clear, and shaking produced visible ethanol droplets, as shown in Fig. 4.5b. 1 wt.% and 2 wt.% oil added to ethanol immediately dissolved with mixing. 3 wt.% oil added to ethanol clouded, and after 2 hours of storage, oil droplets were visible at the bottom of the vial, as shown in Fig. 4.5c.

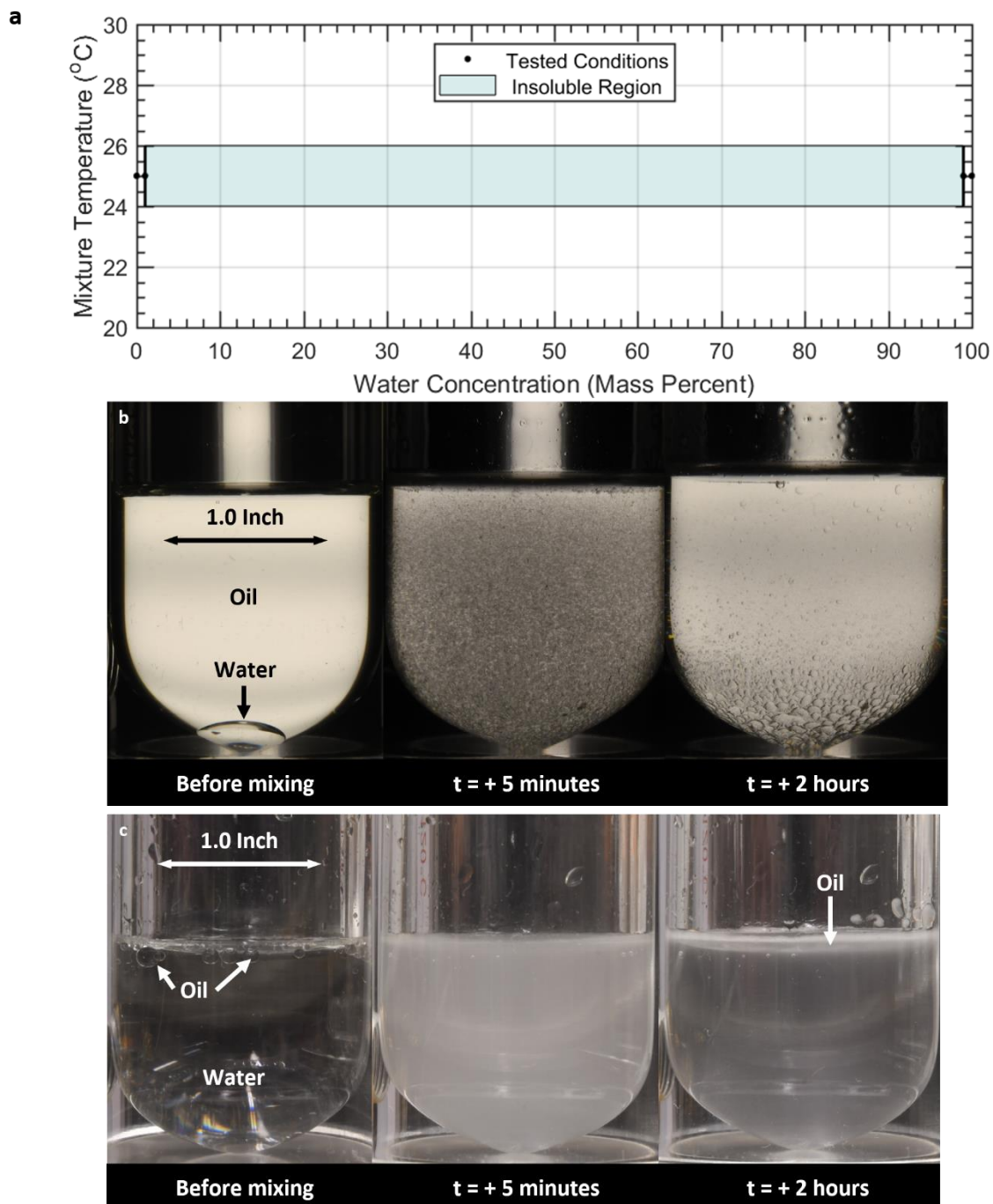


Fig. 4.4 Mutual solubilities of squalane and water at 25°C . a) Solubility plot. b) 1 wt.% water in squalane before and after mixing. c) 1 wt.% squalane in water before and after mixing.

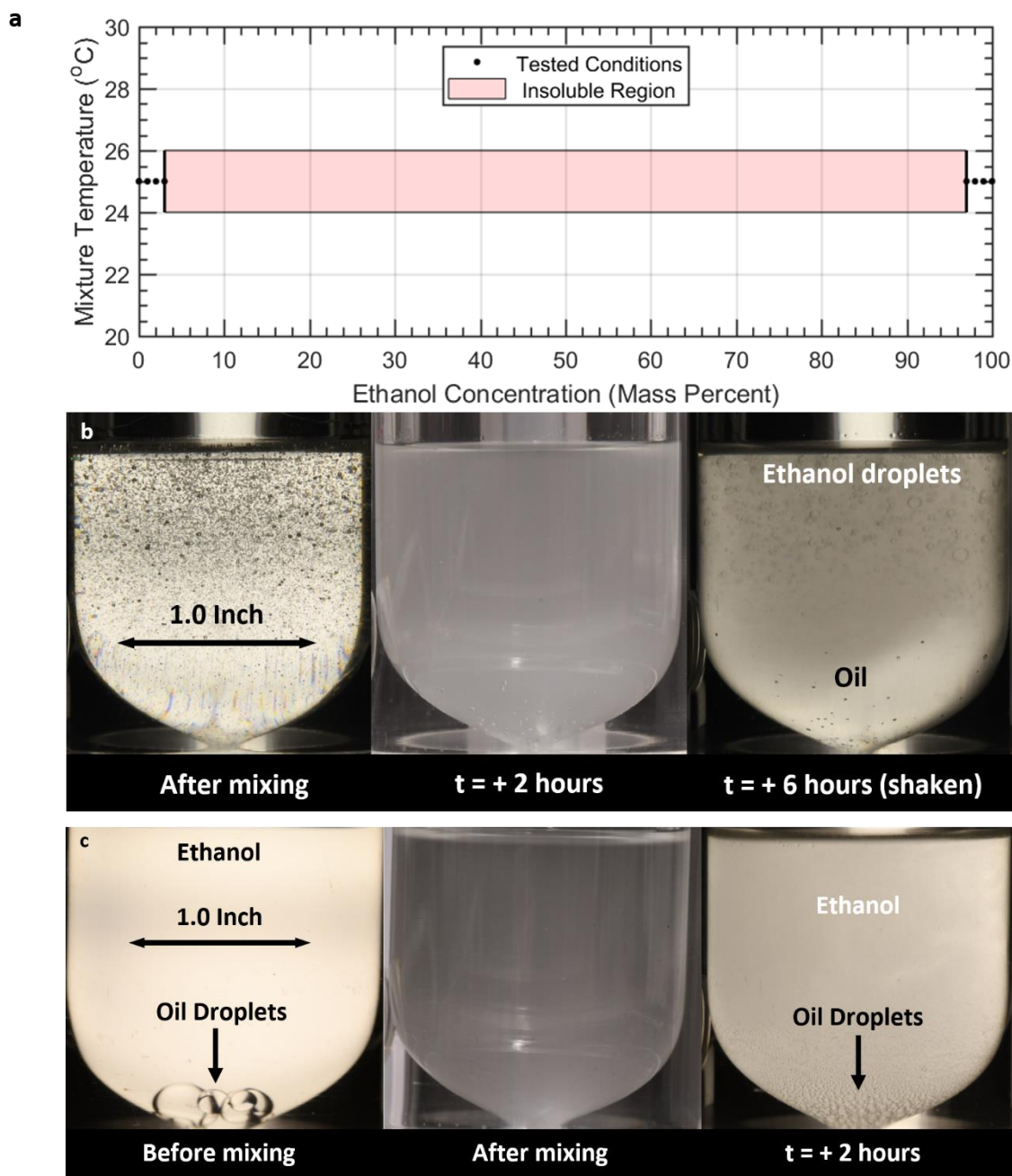


Fig. 4.5 Mutual solubilities of squalane and ethanol at 25°C. a) Solubility plot. b) 3 wt.% ethanol in squalane before and after mixing. c) 3 wt.% squalane in ethanol before and after mixing

4.3 Surfactant Screening Experiments

I conducted sample emulsion experiments to test the efficacy of different surfactants at stabilizing emulsified liquid additives by comparing emulsion stabilities against separation relative to control

group emulsions in which no surfactants were added. The sample emulsions were prepared by dissolving surfactants in the continuous or dispersed phase, depending on the solubility of the surfactant used, followed by the dropwise addition of the dispersed phase to the continuous phase while mixing. Ethanol, water, and formamide were all considered for use as a dispersed phase. Squalane oil was used as the continuous phase for sample emulsions formed, at 25°C, using ethanol and water. Paraffin wax was used as the continuous phase for all emulsions formed using formamide due to formamide's high boiling point and low vapor pressure at the required mixing temperature for paraffin wax, 75°C. For reference, squalane has a nominal density of 805 kg/m³ at 25°C, and paraffin wax has a nominal density of 745 kg/m³ at 75°C. Surfactant screening experimental results are discussed below.

4.3.1 Liquid Additive One - Ethanol

At ambient pressure, ethanol boils at 78°C. FR 5560 paraffin wax melts at 69°C and biphasic dispersion fuels synthesis requires a mixing temperature of 75°C. In order to more quickly screen for surfactants that can stabilize ethanol emulsions, without needing to maintain an elevated temperature and pressure as described in Section 3.5, I tested all 18 surfactants listed in Table 2.2 using squalane oil as a liquid analog for paraffin wax. Ethanol is less dense than squalane oil at 25°C, with a nominal density of 784 kg/m³, and thus will rise to the top of the glass vessel. To provide a control group, I first emulsified ethanol into squalane oil without any surfactant, following the procedures discussed in Section 3.2. The mixture was poured into a temperature-controlled glass vessel maintained at 25°C, and pictures were taken periodically to determine how quickly the ethanol would separate from the oil. The results are shown in Fig. 4.6.

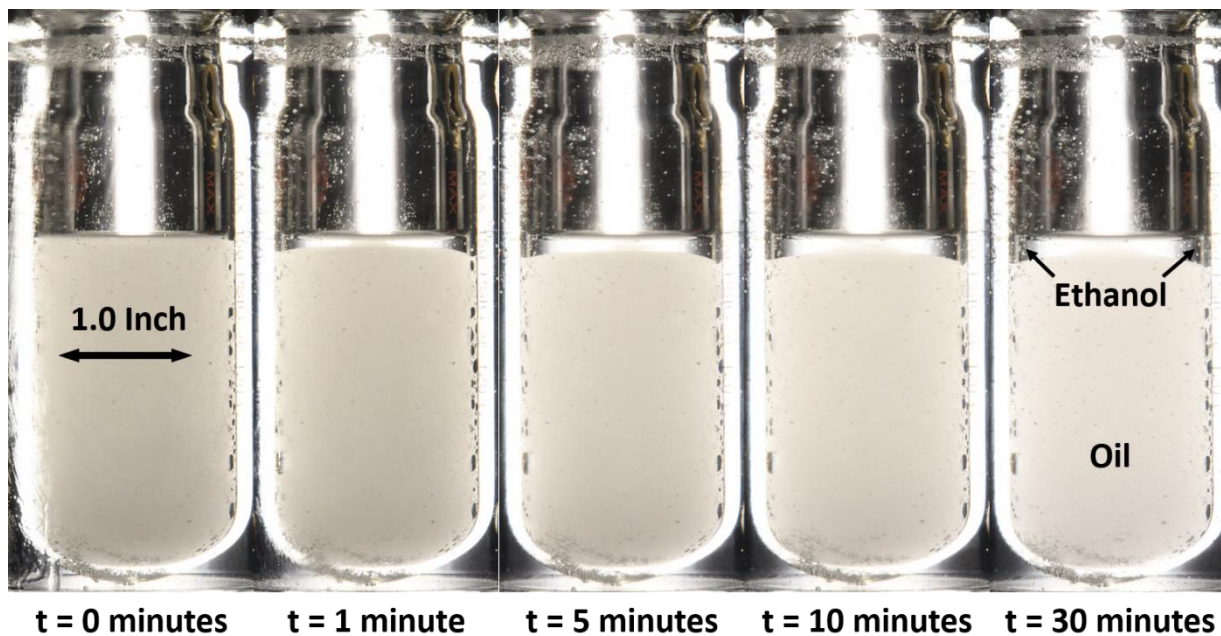


Fig. 4.6 Ethanol-in-oil emulsion control group, formed without a surfactant. Composition is 90 wt.% oil and 10 wt.% ethanol.

The time stamps under each photo represent the time elapsed after pouring the emulsion. After only one minute, the ethanol began to separate from the oil, as evidenced by the clear layer that formed on top. After ten minutes, most of the ethanol had separated from the oil. After this point, the only noticeable change was the gradual decrease in the opacity of the oil phase, as some ethanol dissolved into the oil and the remainder floated to the top. Similar to what was shown in Fig. 4.5, the oil phase never cleared completely due to the finite solubility of ethanol in squalane oil.

All ethanol sample emulsions were formed using 10 wt.% ethanol, 89.5 wt.% squalane oil, and 0.5 wt.% surfactant. However, none of the surfactants tested helped to prevent the coalescence of ethanol droplets, leading to emulsion separation in a matter of minutes. Fig. 4.7 shows an ethanol sample emulsion containing glycerol monostearate used as a surfactant. Like the control group, most of the ethanol quickly separated from the oil, forming a free layer of ethanol on top, and a turbid oil phase on the bottom. The oil phase turbidity gradually decreased for the first 30 minutes but ceased changing subsequently. After two hours, with no visible changes, the mixture was poured out. Fig. 4.8 also depicts similar behavior in an ethanol emulsion formed using Brij® 93 as a surfactant. After only five minutes, a transparent free layer of ethanol formed on the top, with a

turbid oil phase on the bottom. After two hours, with no visible changes, the mixture was poured out.

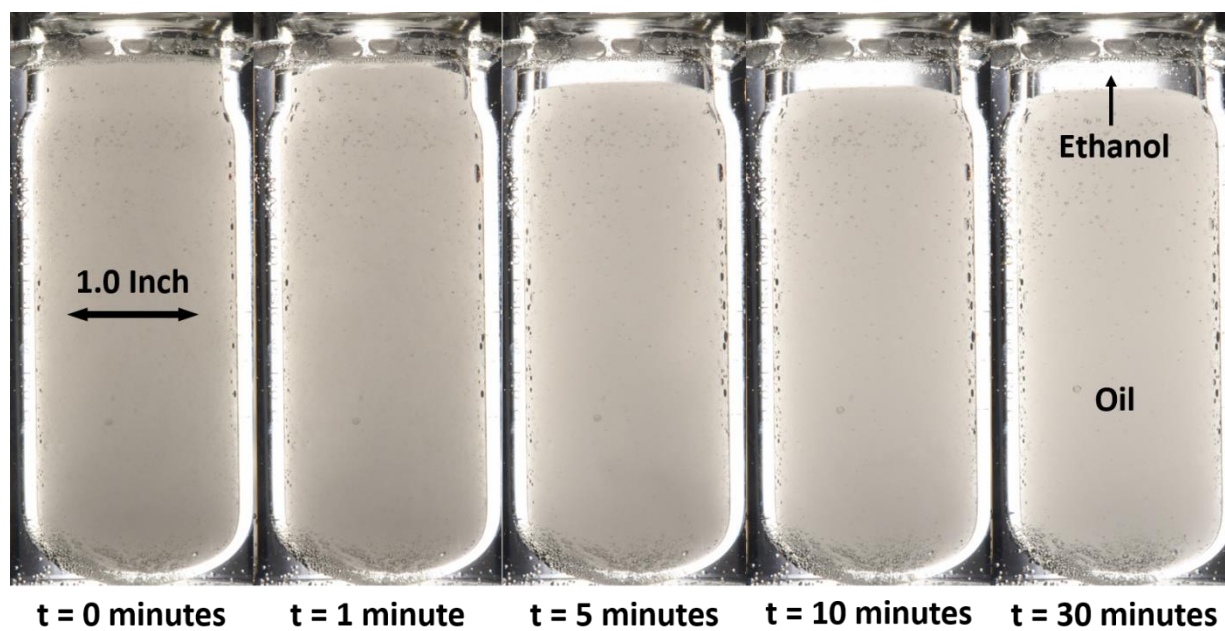


Fig. 4.7 Ethanol-in-oil emulsion formed with glycerol monostearate as a surfactant. Composition is 89.5 wt.% oil, 10 wt.% ethanol, 0.5 wt.% surfactant.

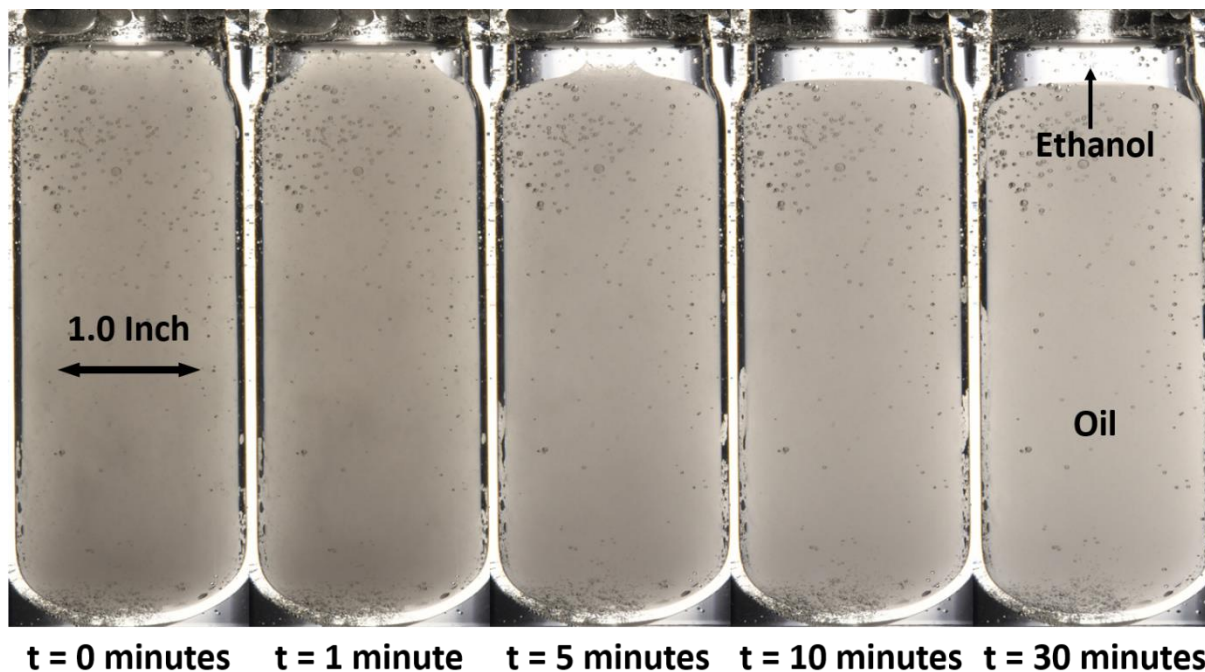


Fig. 4.8 Ethanol-in-oil emulsion formed with Brij® 93 as a surfactant. Composition is 89.5 wt.% oil, 10 wt.% ethanol, and 0.5 wt.% surfactant.

The cloudiness of the oil phase in each of the emulsions is attributed to the finite solubility of ethanol in squalane. Solubility tests of squalane and ethanol, discussed in Section 4.2, indicated that solutions of 2 wt.% ethanol in squalane gradually cleared after several hours of storage, but that additional ethanol added caused an oil turbidity that did not clear within six hours of storage. The surfactants used in the formation of sample emulsion, although added in small quantity, may alter the mutual solubility between ethanol and squalane, and could be tested using the procedures outlined in Section 4.2 for completeness.

Lasheras et al. and a number of other research groups describe similar difficulties in finding a commercially available surfactant to stabilize an emulsion containing ethanol. [11], [37] Xu et al. discuss the formation and instability of ethanol-in-vegetable oil emulsions. [37] Of the 21 different non-ionic surfactants tested in their experiments, only decaglycerol mono-oleate was able to stabilize ethanol-in-oil emulsions, reportedly preventing droplet coalescence and emulsion breakdown for 150 days. Further testing is required to find a surfactant suitable to stabilize emulsions formed between ethanol and squalane and/or ethanol and FR5560 paraffin wax, if ethanol is desired as a liquid fuel additive for use in a hybrid rocket application.

4.3.2 Liquid Additive Two - Water

Water is denser than squalane oil at 25°C, with a nominal density of 999 kg/m³, and thus will settle to the bottom of the vessel. Surfactants were screened in a similar manner for emulsions formed between DI water and squalane oil. A control group emulsion containing 90 wt.% oil and 10 wt.% water, without any surfactant, is shown in Fig. 4.9. After 60 minutes, most of the water had settled to the bottom of the vessel, leaving a translucent water layer at the bottom, and a turbid oil phase on top. After 120 minutes, no further changes were visible and the mixture was poured out. Similar to what was observed in the oil and water solubility experiments, water dispersed in squalane oil caused an oil phase turbidity that took several hours to clear. In the future, for completeness, emulsions formed using surfactants should be left in storage for longer periods to observe any changes that may take place and to observe how surfactant addition changes the mutual solubility of water and oil.

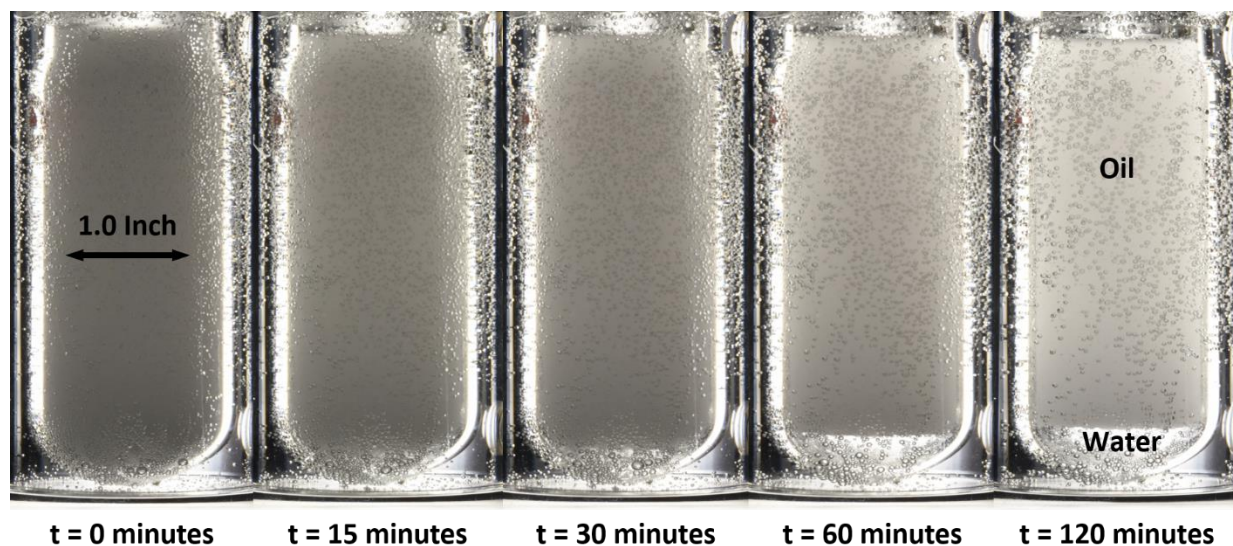


Fig. 4.9 Water-in-oil emulsion control group, formed without a surfactant. Composition is 90 wt.% oil and 10 wt.% DI water.

Many of the sample emulsions formed between water and squalane exhibited similar behavior to the control group despite the use of surfactants, which did not provide significant improvements in stability, if at all. For instance, Fig. 4.10 shows a sample emulsion containing 89.5 wt.% oil, 10 wt.% water, and 0.5 wt.% Brij[®] 52 as a surfactant. Homogenization of the components formed an

opaque, white mixture that gradually decreased in turbidity. After 30 minutes, a translucent water layer formed at the bottom of the vessel and after 180 minutes, no further changes were visible.

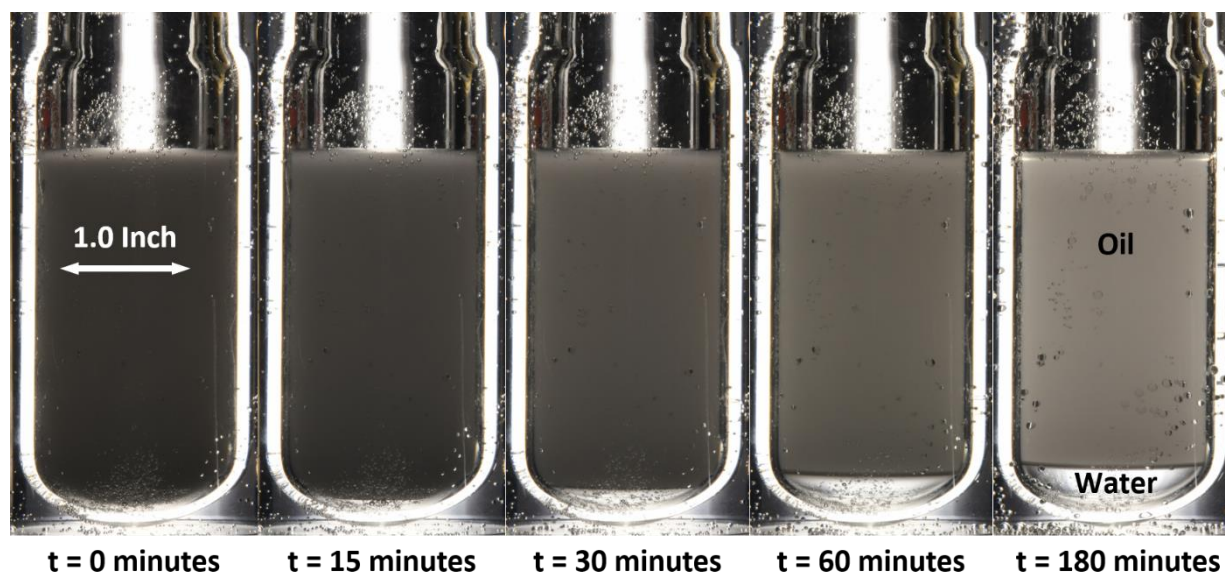


Fig. 4.10 Water-in-oil emulsion formed with Brij® 52 as a surfactant. Composition is 89.5 wt.% oil, 10 wt.% water, and 0.5 wt.% surfactant

However, several of the sorbitan ester-based surfactants provided significant improvements in emulsion stability and showed differed behavior than the control group. Fig. 4.11 and Fig. 4.12 show emulsions formed between water and squalane, using Span® 85 and Span® 80 as surfactants, respectively. Rather than forming a transparent layer of water at the bottom of the vessel, a translucent oil supernatant formed on top of an opaque emulsion layer that gradually settled to the bottom. The difference in emulsion stability suggests that Span® 80 and Span® 85 are active at the interface between water droplets and the oil phase, adsorbing at the interface to form an interfacial film that prevents droplet coalescence and emulsion breakdown via steric stabilization. The emulsion containing Span® 85 took two hours for emulsified water droplets to settle half of the total initial emulsion height, or roughly 1.4 inches, as shown in Fig. 4.11. The emulsion containing Span® 80 took seven hours for water droplets to settle half of the total initial emulsion height, or roughly 1.25 inches, as shown in Fig. 4.12. Of the 18 different non-ionic surfactants studied, Span® 80 was found to be the most effective surfactant at preventing the separation of emulsions formed between water and squalane oil.

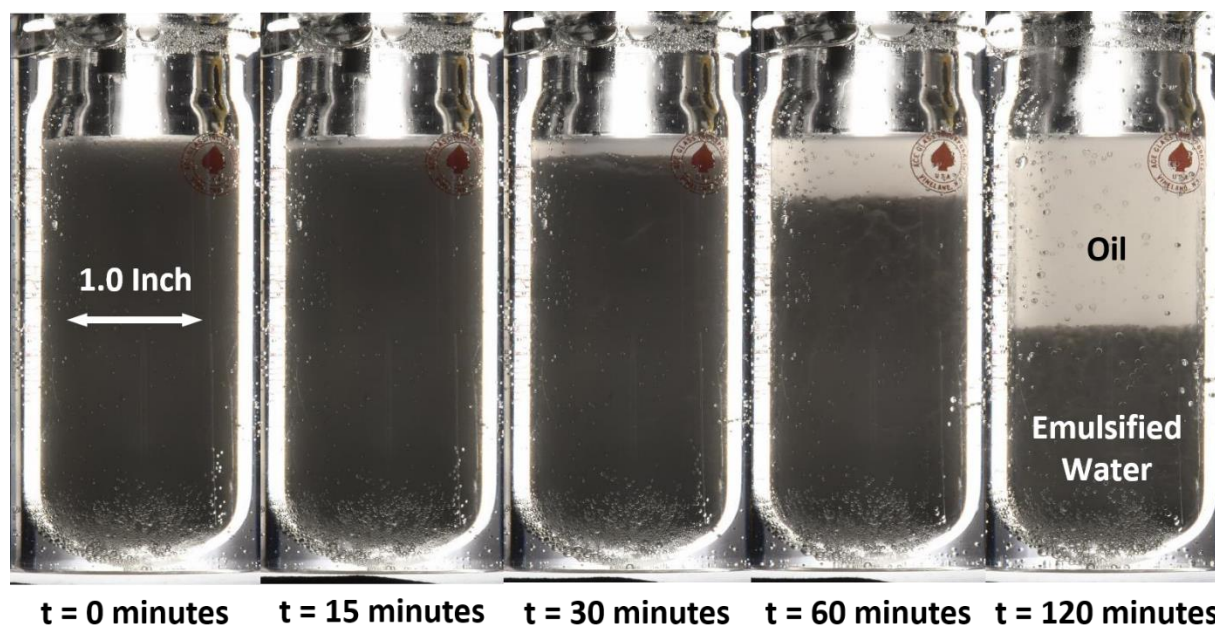


Fig. 4.11 Water-in-oil emulsion formed with Span[®] 85 as a surfactant. Composition is 89.5 wt.% oil, 10 wt.% water, and 0.5 wt.% surfactant.

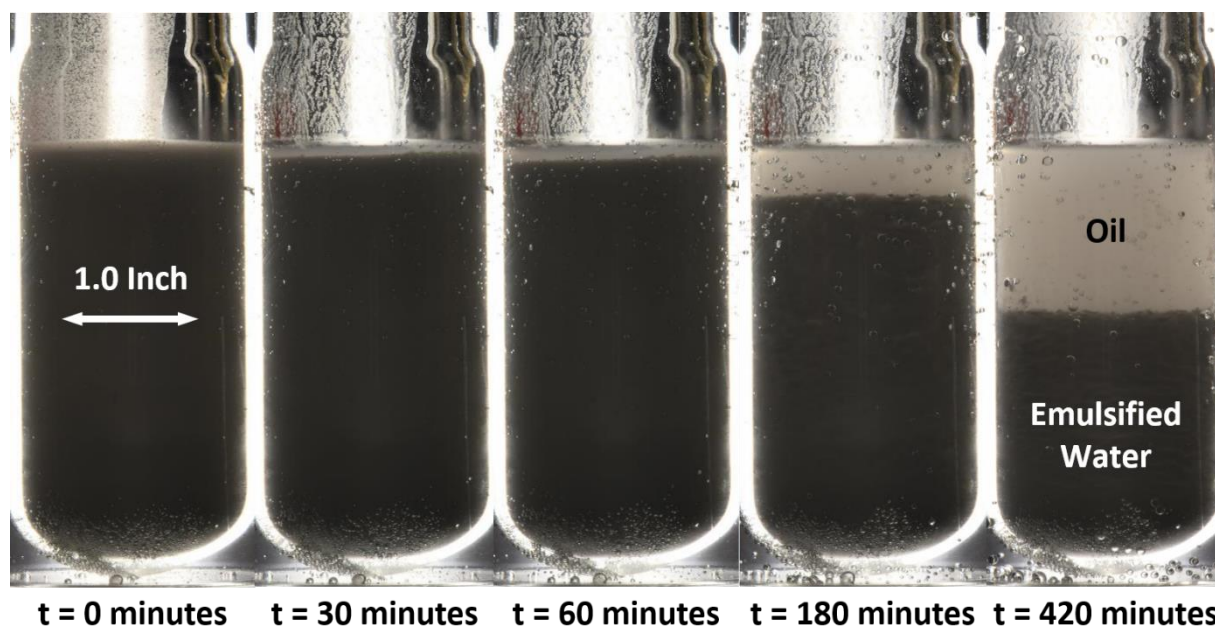


Fig. 4.12 Water-in-oil emulsion formed with Span[®] 80 as a surfactant. Composition is 89.5 wt.% oil, 10 wt.% water, and 0.5 wt.% surfactant.

Using the knowledge gained from forming sample emulsions with water, I began to form the fuel binder emulsions using FR 5560 paraffin wax in place of the squalane oil. In order to maintain the required temperatures and pressures, I used the optically accessible emulsion visualization apparatus described above in Section 3.3. All wax emulsions were formed and stored for visualization at 75°C and 50 psia.

To provide a control group, I first emulsified water into paraffin wax without any surfactant and took pictures to determine how long it would take the water to migrate through the wax and settle to the bottom of the vessel. The results are shown in Fig. 4.13. After five minutes, most of the water had settled towards the bottom of the vessel, leaving a turbid wax layer on top. After 30 minutes, most of the water had completely settled. After two hours, no further changes were visible and the mixture was poured out. Similar experiments were performed using sorbitan ester-based surfactants due to their ability to slow the breakdown of emulsions formed between water and squalane oil, as described above.



Fig. 4.13 Water-in-wax emulsion control group, formed without a surfactant. Composition is 90 wt.% wax and 10 wt.% DI water.

In contrast to the behavior of the water-in-oil emulsion containing Span[®] 85 as a surfactant, the water-in-wax emulsion containing Span[®] 85 quickly separated, as shown in Fig. 4.14. After only five minutes, an opaque layer of water had formed at the bottom of the vessel, leaving a turbid wax phase on top. After 20 minutes, most of the water had settled, and a thin transparent layer of wax formed at the very top.

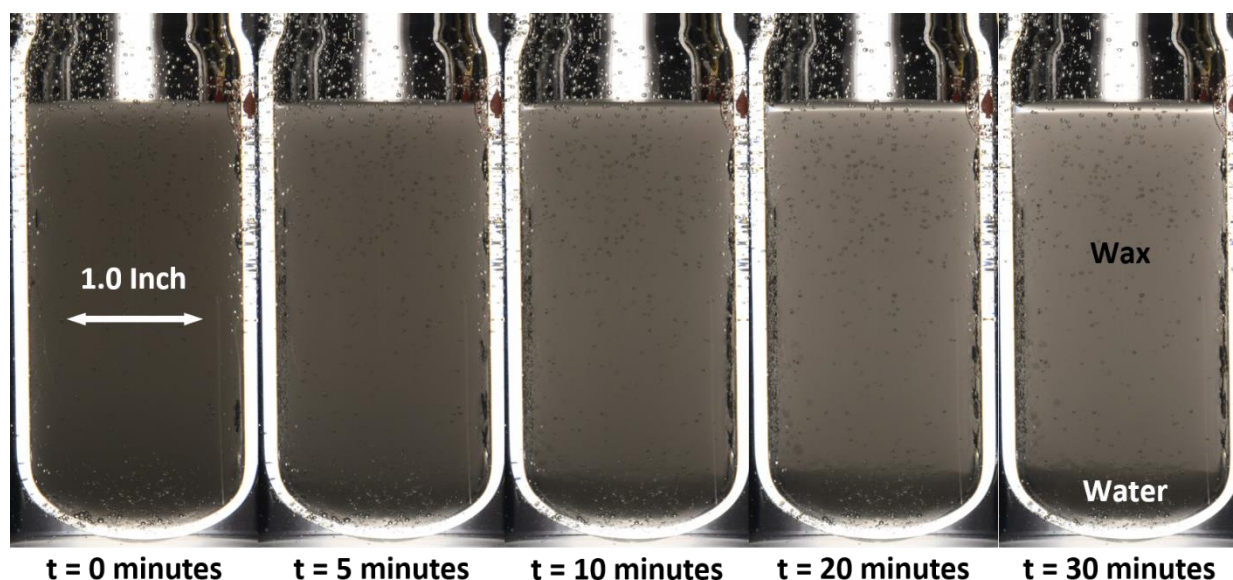


Fig. 4.14 Water-in-wax emulsion formed with Span[®] 85 as a surfactant. Composition is 89.5 wt.% wax, 10 wt.% water, and 0.5 wt.% surfactant.

Emulsions formed between water and wax using Span[®] 80 as a surfactant were far less stable than water-in-oil emulsions formed using Span[®] 80, as shown in Fig. 4.15. Immediately after mixing and pouring the emulsion into the glass vessel, water droplets rapidly flocculated, forming larger droplet aggregates that settled quickly to the bottom. After only seven minutes, the emulsified water had settled half of the total initial emulsion height, or roughly 1.75 inches. Due to this discrepancy in emulsion stability, I investigated the effect of emulsion formation and storage temperature on the stability of a water-in-oil emulsion using the same proportion of water, squalane oil, and Span[®] 80 as the emulsion shown in Fig. 4.12.

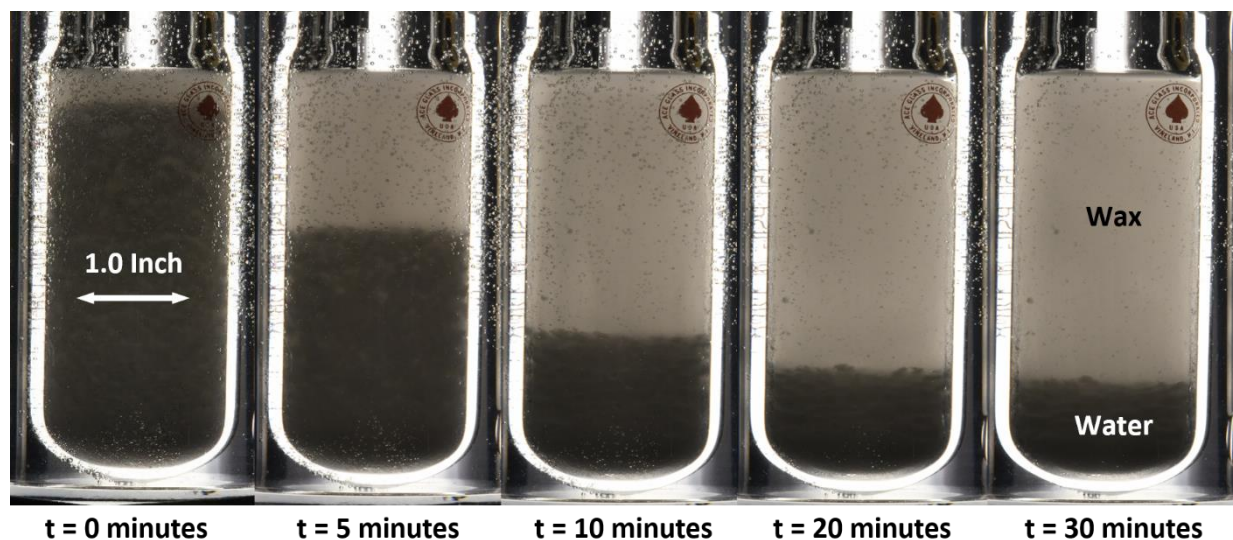


Fig. 4.15 Water-in-wax emulsion formed with Span® 80 as a surfactant. Composition is 89.5 wt.% wax, 10 wt.% water, and 0.5 wt.% surfactant.

At 75°C, FR 5560 paraffin wax has a viscosity of 4.9 mPa·s, and the density difference between water and wax is 252 kg/m³. In contrast at 25°C, squalane oil has a viscosity of 27.9 mPa·s, and the density difference between water and squalane is 195 kg/m³. As described in Section 3.4, the settling velocity of droplets through a medium is proportional to the ratio of the density difference and the continuous phase viscosity. When comparing the physical properties of paraffin wax at 75°C to squalane oil at 25°C, the ratio of the density difference between the dispersed and continuous phases, and the viscosity of the continuous phase is 86% larger for squalane than it is for wax. Although this is a simplified analysis that fails to incorporate complex emulsion behavior such as attractive and/or repulsive forces between droplets and differences in the polydispersity of each emulsion, it provides a first-order comparison between sample emulsion formed with squalane and fuel binder emulsions formed with paraffin wax. Due to these differences, droplets of a similar radius should settle roughly 7.5 times as quickly through the wax at 75°C, as they do through the squalane oil at 25°C. However, experiments showed that water droplets settled 200 times more quickly in wax than in squalane, suggesting that other effects besides buoyancy forces are at play. In order to test the importance of mixture temperature and any effect this may have on the efficacy of surfactants to stabilize an emulsion, I formed an emulsion of water in squalane using Span® 80 as a surfactant, with the same proportions as previously tested, but at 75°C in order to keep the mixing and storage temperature consistent with the wax-based emulsions. The results

are shown in Fig. 4.16. At 75°C, squalane has a viscosity of 5.3 mPa·s and the density difference between water and squalane is 223 kg/m³. Now comparing the physical properties of paraffin wax at 75°C to squalane oil at 75°C, the ratio of the density difference between the dispersed and continuous phases, and the viscosity of the continuous phase is 22% larger for wax than it is for squalane, suggesting that droplets of a similar radius should settle roughly settle 1.2 times as quickly through the squalane as they do through the wax.

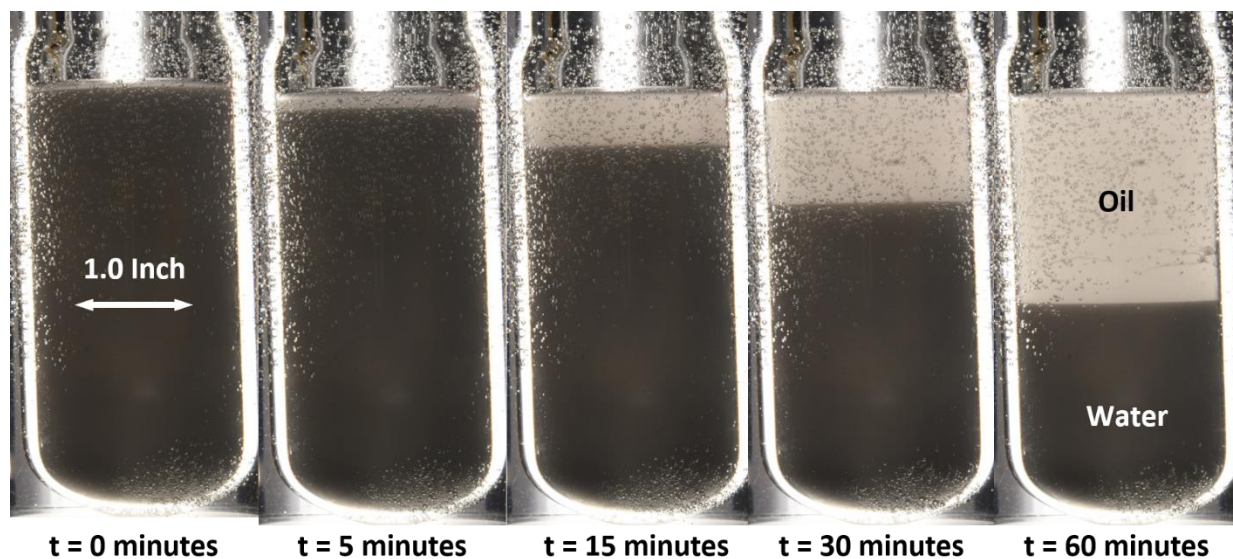


Fig. 4.16 Water-in-oil emulsion formed at 75°C with Span® 80 as a surfactant. Composition is 89.5 wt.% oil, 10 wt.% water, and 0.5 wt.% surfactant

A comparison of Fig. 4.15 and Fig. 4.16 indicate that at the same temperature, water droplets settled 8.7 times more quickly in wax than in squalane. Given these results, further testing is required to determine whether squalane provides a suitable liquid analog to paraffin wax. All further surfactant screening experiments were conducted with paraffin wax.

4.3.3 Liquid Additive Three - Formamide

Formamide is denser than paraffin wax at 75°C, with a nominal density of 1088 kg/m³, and thus will settle to the bottom of the vessel. To provide a control group, I first emulsified formamide into paraffin wax without any surfactant and took pictures to determine how long it would take the formamide to separate from the wax and settle to the bottom of the vessel. The results are shown

in Fig. 4.17. Neither the wax nor the formamide phases clouded, and immediately after pouring the mixture, formamide began to settle to the bottom. After five minutes, no further changes were visible.

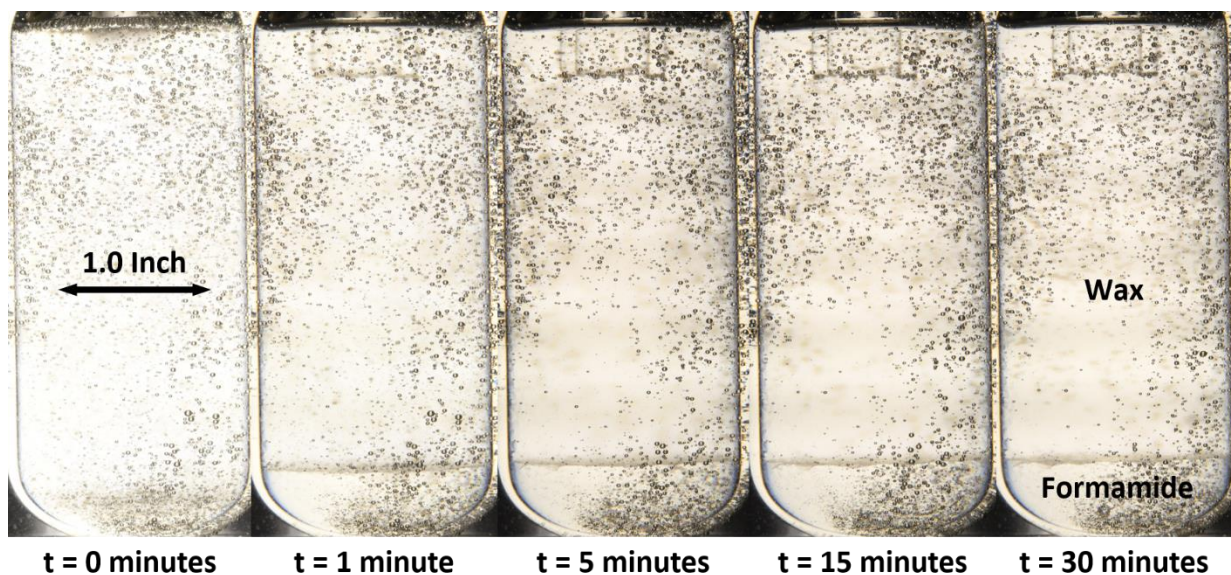


Fig. 4.17 Formamide-in-wax emulsion control group, formed without a surfactant. Composition is 80 wt.% wax and 20 wt.% formamide.

None of the surfactants tested showed an ability to stabilize emulsions formed between formamide and paraffin wax. Early on in my research, I experimented with formamide as a potential liquid fuel additive and formed several emulsions between formamide and paraffin oil (Sigma Aldrich, CAS #: 8012-95-1) using non-ionic surfactants. Fig. 4.18 shows a control group experiment in which formamide was emulsified into paraffin oil without added surfactant. The control group emulsion composition was 90 wt.% paraffin oil and 10 wt.% formamide. In less than one hour, the formamide had completely settled to the bottom of the glass vessel, and no further changes were observed over a 24-hour period. Fig. 4.19 shows an emulsion formed between formamide and paraffin oil using Span® 80 as a surfactant. The emulsion composition was 89 wt.% paraffin oil, 10 wt.% formamide, and 1.0 wt.% surfactant. This emulsion took more than two hours for there to be a noticeable change in the emulsion height. At six hours, a clear layer of oil had formed on top of the emulsion as formamide droplets settled. At 24 hours, the formamide droplets had settled roughly one half of the total initial emulsion height, or 3.0 inches.

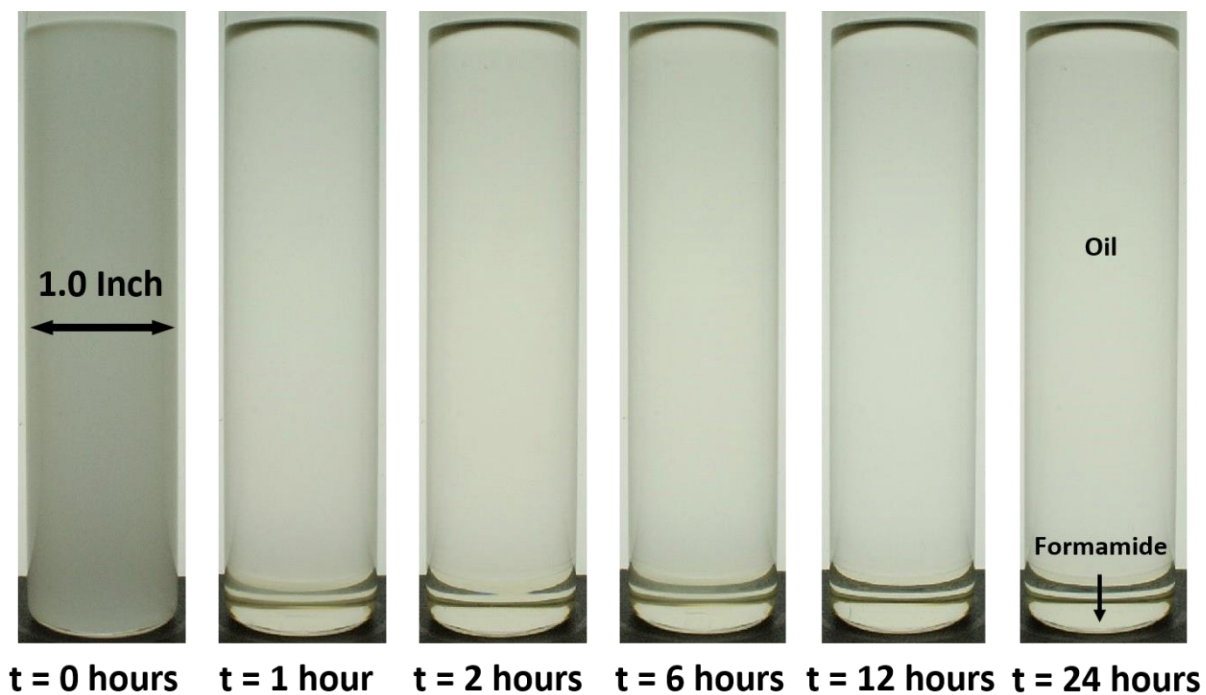


Fig. 4.18 Formamide-in-paraffin oil emulsion control group, formed without a surfactant. Composition is 90 wt.% oil and 10 wt.% formamide.

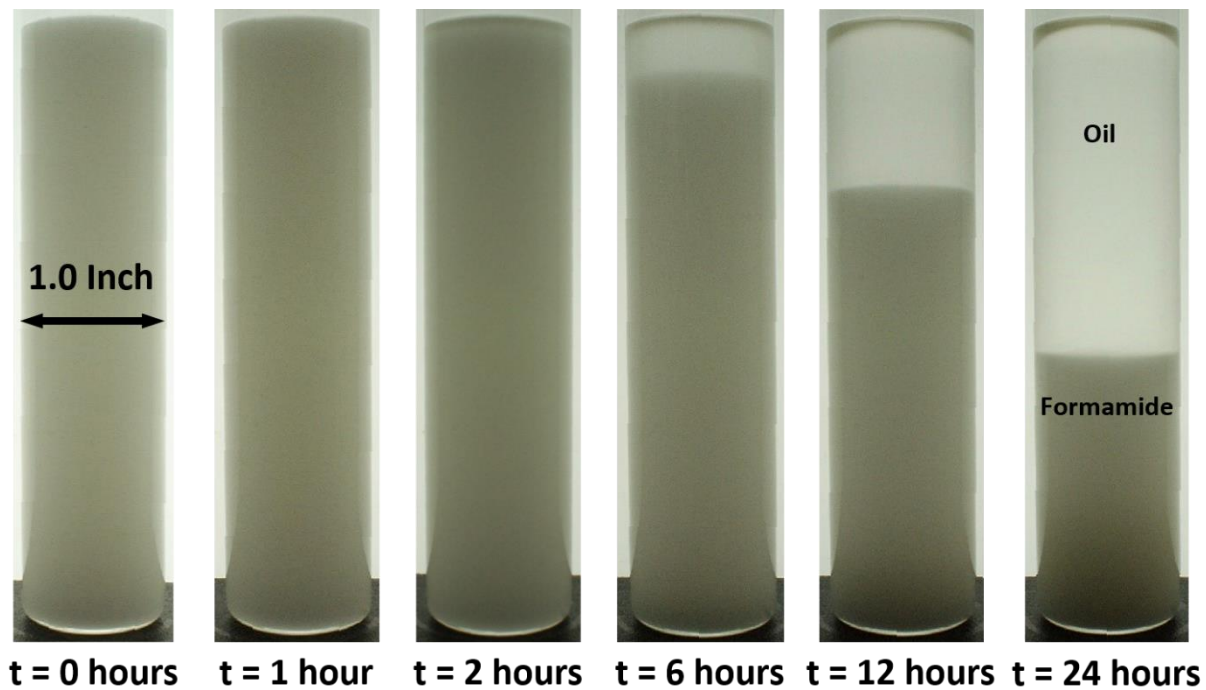


Fig. 4.19 Formamide-in-paraffin oil emulsion formed with Span[®] 80 as a surfactant. Composition is 89.0 wt.% oil, 10 wt.% formamide, and 1.0 wt.% surfactant.

In contrast to these results, all attempts to emulsify formamide in paraffin wax were unsuccessful, as shown in Fig. 4.20, Fig. 4.21, and Fig. 4.22. Fig. 4.20 shows a formamide emulsion containing 79.5 wt.% wax, 20 wt.% formamide, and 0.5 wt.% Span[®] 80 . Unlike the more stable emulsion formed with paraffin oil, formamide quickly settled to the bottom of the vessel.

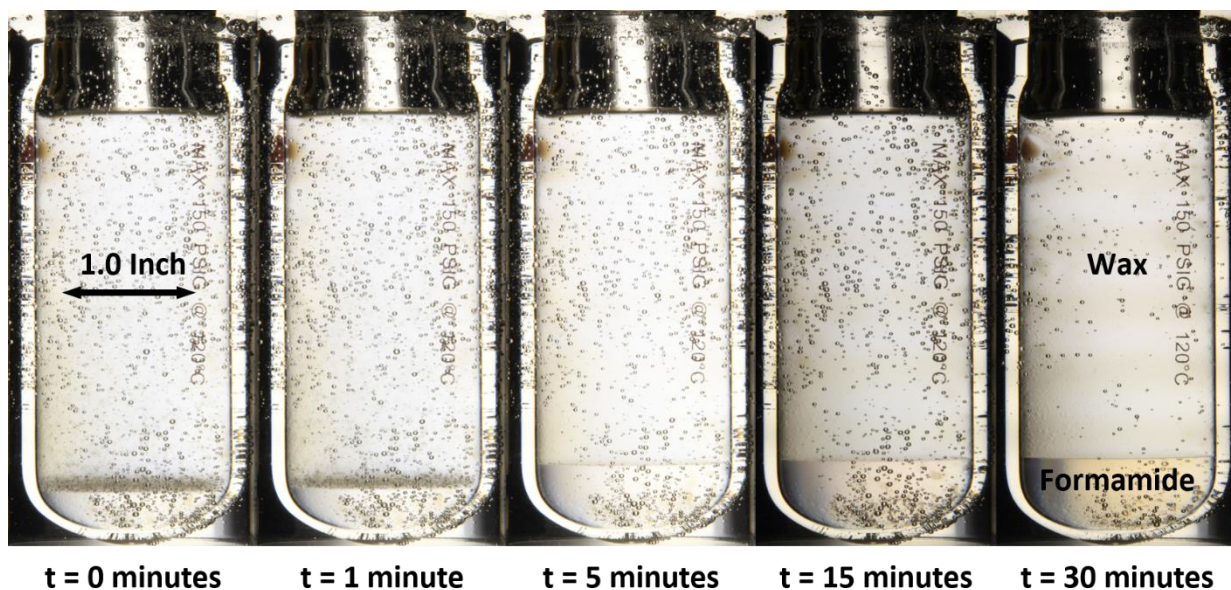


Fig. 4.20 Formamide-in-wax emulsion, formed with Span[®] 80 as a surfactant. Composition is 79.5 wt.% wax, 20 wt.% formamide, and 0.5 wt.% surfactant.

Imhof and Pine discussed the ability to form stable nonaqueous emulsions between formamide and decane using a number of different surfactants, including Triton[™] X-100 and Brij[®] 52. [22] I attempted to form emulsions between formamide and FR 5560 paraffin wax using these same surfactants, but in each case formamide settled to the bottom of the vessel immediately upon pouring the mixture, as shown in Fig. 4.21 and Fig. 4.22. In five minutes, the majority of the formamide had completely settled, and after 30 minutes, no noticeable changes in the emulsions took place.

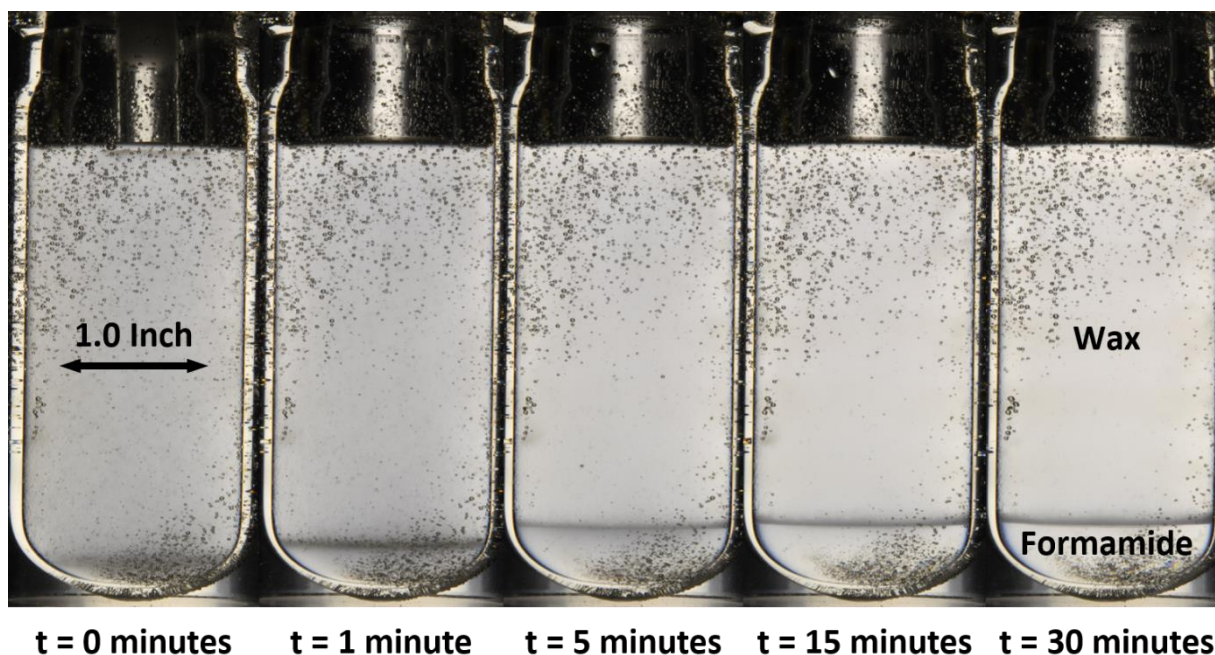


Fig. 4.21 Formamide-in-wax emulsion, formed with Triton™ X-100 as a surfactant. Composition is 79.5 wt.% wax, 20 wt.% formamide, and 0.5 wt.% surfactant.

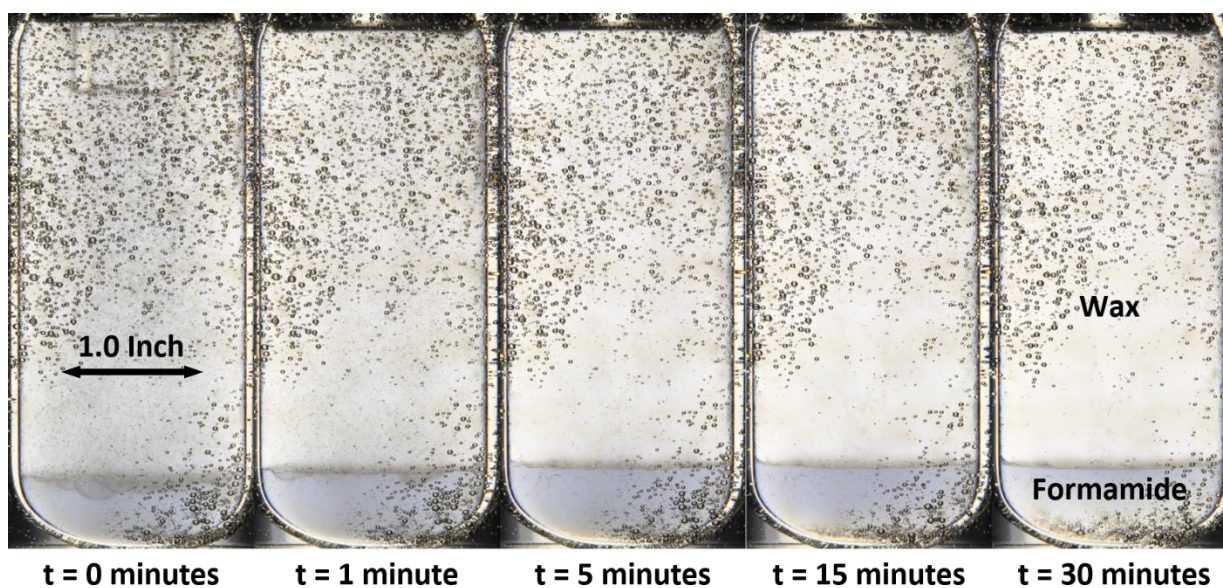


Fig. 4.22 Formamide-in-wax emulsion, formed with Brij® 52 as a surfactant. Composition is 79.5 wt.% wax, 20 wt.% formamide, and 0.5 wt.% surfactant.

Imhof and Pine were unable to find a satisfactory explanation for what molecular properties dictate the emulsifying capacity of non-aqueous molecules but suggested that Ostwald ripening may a

play a key role in the instability of non-aqueous emulsions due to the increased mutual solubilities of non-aqueous solvents and oils. [22] I do not believe Ostwald ripening to be responsible for the lack of success with formamide-in-wax emulsion since none of the combinations tested showed any signs of forming emulsions whatsoever, and formamide was not found to have a high solubility in FR 5560 paraffin wax. Imhof and Pine did find that surfactant molecular weight plays a role in the stability of non-aqueous emulsions, with the greatest stability coming from formamide emulsions formed with high molecular weight triblock copolymers of polyethylene oxide (PEO) and polypropylene oxide (PPO) in a PEO-PPO-PEO structure. PEO-PPO-PEO triblock copolymers are not readily available and prohibitively expensive, costing upwards of \$1000 per gram. While all 18 surfactants were tested for their ability to stabilize emulsions containing water and ethanol, only six total surfactants were tested with formamide. With more time, further testing could help to find a surfactant that is capable of stabilizing emulsions formed between formamide and FR 5560 paraffin wax, if any exist. If none of the inexpensive, commercially available non-ionic surfactants are found to produce stable emulsions, PEO-PPO-PEO surfactants could be tested in small scale experiments to determine the viability as a surfactant for biphasic dispersion hybrid rocket applications.

4.4 Stokes' Settling Velocity and Droplet Sizing

Of the three different liquid fuel additives chosen for the purposes of forming biphasic dispersion fuel grains with FR 5560 paraffin wax, water was the only one found to produce an emulsion that was stable enough to quickly cool and cast into cylindrical fuel grains using the procedures described in Section 3.5.3. I calculated the Stokes' settling velocities for the most stable formulations using photographs taken during emulsion storage and a photo processing code written in MATLAB. Images are uploaded to MATLAB with time stamps to indicate the length of time between consecutive photographs. A calibration image provides the resolution and scale of each emulsion photograph in terms of millimeters per pixel. The code tracks the interface between the emulsion and the clear wax or oil supernatant layer that forms on top and records the total change in emulsion height for each image and the time at which the photo was taken. After all images are processed, the code provides a plot of each data point. The experimental settling velocity is recorded as the slope of the linear portion of the plot, and a simple linear regression of the data verifies that the data fits with an acceptable R^2 value.

Fig. 4.23 shows a plot of the emulsion interface position over time for the emulsion shown in Fig. 4.12. Note that the settling rate of the emulsified droplets is only linear for the two hours of storage, at which point droplet-droplet interaction begins to slow the rate of sedimentation. The slope of the settling rate over the first two hours of storage is 0.0013 inch/minute, with a coefficient of determination of 0.95, suggesting a good fit of the data.

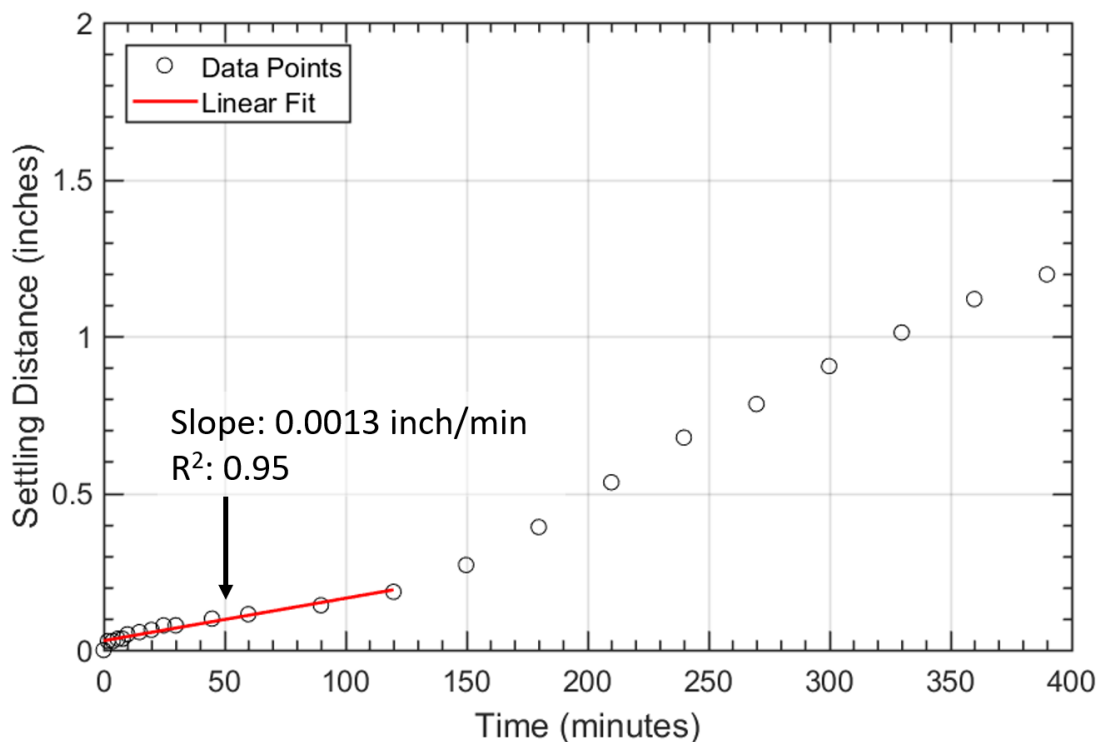


Fig. 4.23 Experimental data points of interfacial position of the emulsion pictured in Fig. 4.12.

The calculated emulsion settling rate, or experimental settling velocity, can be related to an approximate average droplet radius using Stokes' law, as described above in Section 3.4. Using the known values of both η_c and $\Delta\rho$, the expected settling velocity of emulsified droplets for the given emulsion properties can be plotted as a function of droplet radius, as shown in Fig. 4.24. The experimentally determined settling velocity, 0.0013 inch/minute or $5.7 \cdot 10^{-4}$ mm/s, corresponds to an expected averaged droplet radius of 6.2 μm , considering only the balance between viscous drag and buoyancy forces and ignoring all droplet-droplet interactions, droplet deformation, etc.

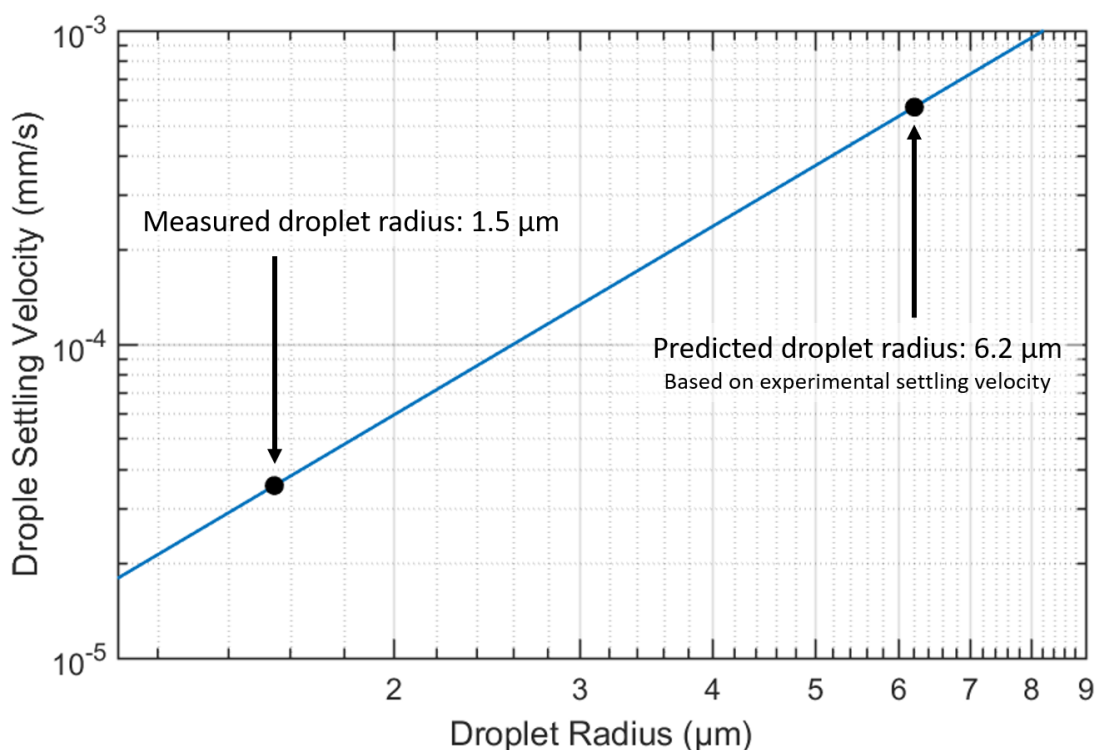


Fig. 4.24 Relationship between droplet settling velocity and droplet radius for an emulsion of water in squalane, assuming Stokes' flow.

Following the work of Souza et al., I calculated an adjusted settling velocity based on the dispersed phase volume fraction, using Eq. 4, in order to account for droplet-droplet interactions. [30] In order to determine the empirical exponent, n , I diluted the emulsion with the continuous phase, squalane, and imaged the droplets on a HIROX KH-8700 digital microscope, as shown in Fig. 4.25. Using a custom image processing code written in MATLAB, and the calibration bar provided on the bottom of each microscope image, I determined an average droplet diameter using several different diluted samples of the same emulsion. 100 emulsified water droplets were counted to form a histogram of the droplet diameters. Results indicate a mean droplet diameter of 3.1 μm with a standard deviation of 1.8 μm .

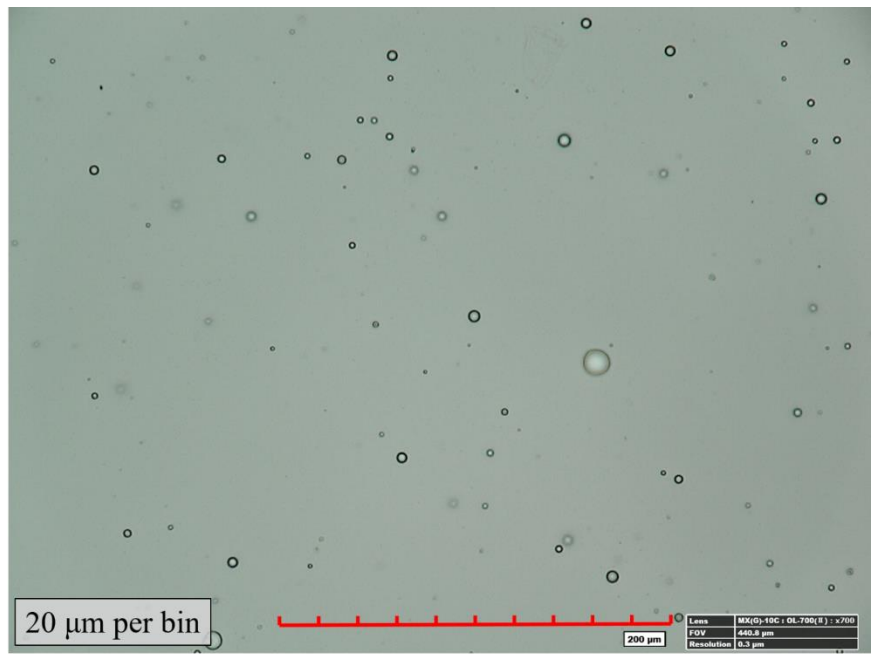


Fig. 4.25 Image of emulsified water droplets taken on a HIROX KH-8700 digital microscope under 700 times magnification.

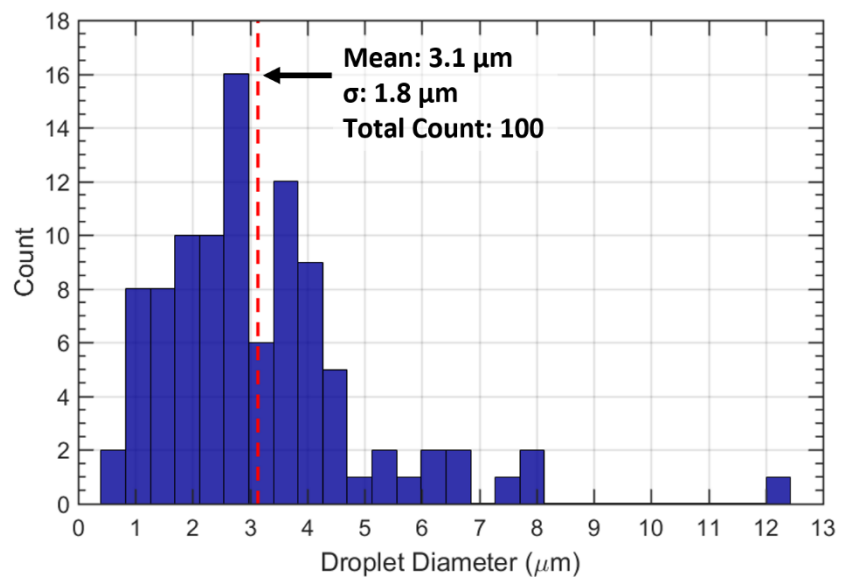


Fig. 4.26 Histogram of emulsion droplet diameters for the emulsion pictured in Fig. 4.12.

Using the mean droplet diameter determined with the microscope images, and the known continuous phase viscosity and density difference between the dispersed and continuous phases, I calculated an expected Stokes' settling velocity using Eq. 4, and solved for the empirical exponent,

n , in Eq. 4. For the emulsion pictured in Fig. 4.12, the empirical exponent is -32.3 . Note that according to Richardson and Zaki, who developed the correlation, n should reside between 2.3 and 5. [31] Additionally, droplet-droplet interaction should decrease the experimental settling velocity relative to what is predicted using Stokes' law. However, the experimentally determined settling velocity for this emulsion is almost three times as large as that predicted by Stokes' law. These discrepancies suggest that the emulsion is unstable, and its behavior is not adequately captured by a simplified Stokes' flow analysis. HIROX images of the undiluted emulsion provides an explanation for the unexpected results. As shown in Fig. 4.27, emulsified droplets formed aggregates or flocs, where smaller droplets combined into larger, irregular particle structures. As the structures grew, buoyancy forces accelerated the rate of sedimentation.

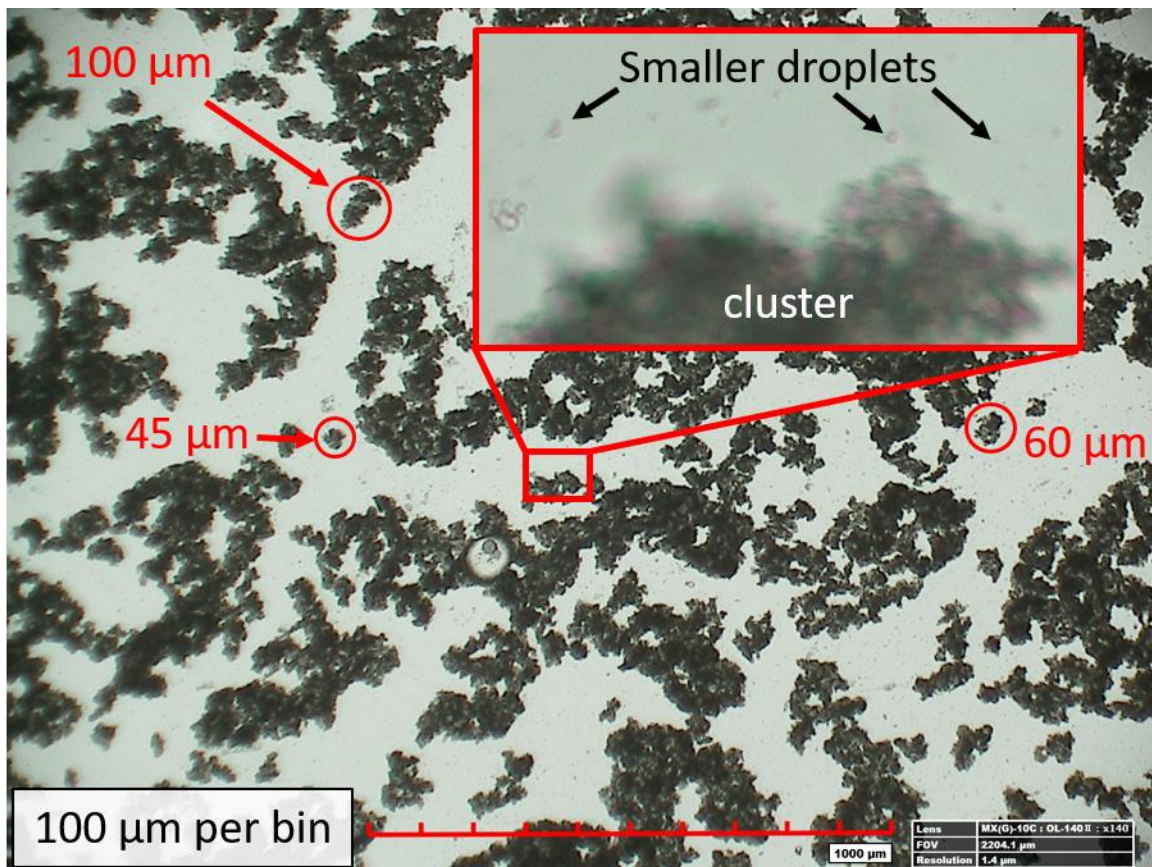


Fig. 4.27 Image of an undiluted emulsion taken on a HIROX KH-8700 digital microscope under 140 times magnification.

I performed a similar analysis for the emulsion used to form BDF formulation three, as shown below. Fig. 4.28 shows periodic photographs taken of an emulsion containing 20 wt.% DI water, 79.5 wt.% paraffin wax, and 0.5 wt.% Span® 80 surfactant. Emulsified water droplets had settled roughly half of the initial emulsion height after only five minutes.

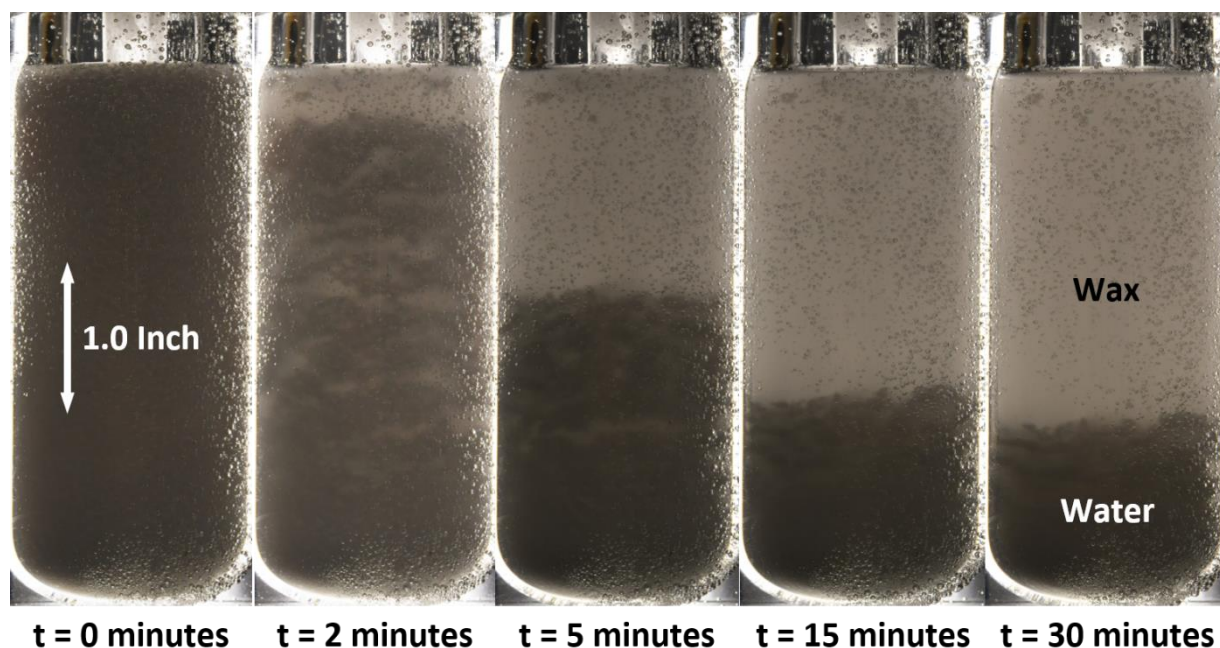


Fig. 4.28 Water-in-wax emulsion formed with Span® 80 as a surfactant. Composition is 79.5 wt.% wax, 10 wt.% water, and 0.5 wt.% surfactant

Using a MATLAB code, the emulsion interface was tracked as a function of time, and plotted to determine the settling velocity, as shown in Fig. 4.29. The experimentally determined settling velocity, 0.361 inch/minute or 0.153 mm/s, corresponds to an expected averaged droplet radius of 37 μm , considering only the balance between viscous drag and buoyancy forces and ignoring all droplet-droplet interactions, droplet deformation, etc. In order to determine the actual droplet size, the emulsion was cooled to form a biphasic dispersion and a small sample was melted and diluted in dodecane. The diluted sample was imaged on the HIROX microscope, and droplets were sized using the MATLAB code discussed previously. A HIROX image of the diluted sample is shown in Fig. 4.30 and the histogram of the droplet diameters obtained from the MATLAB code is shown in Fig. 4.31.

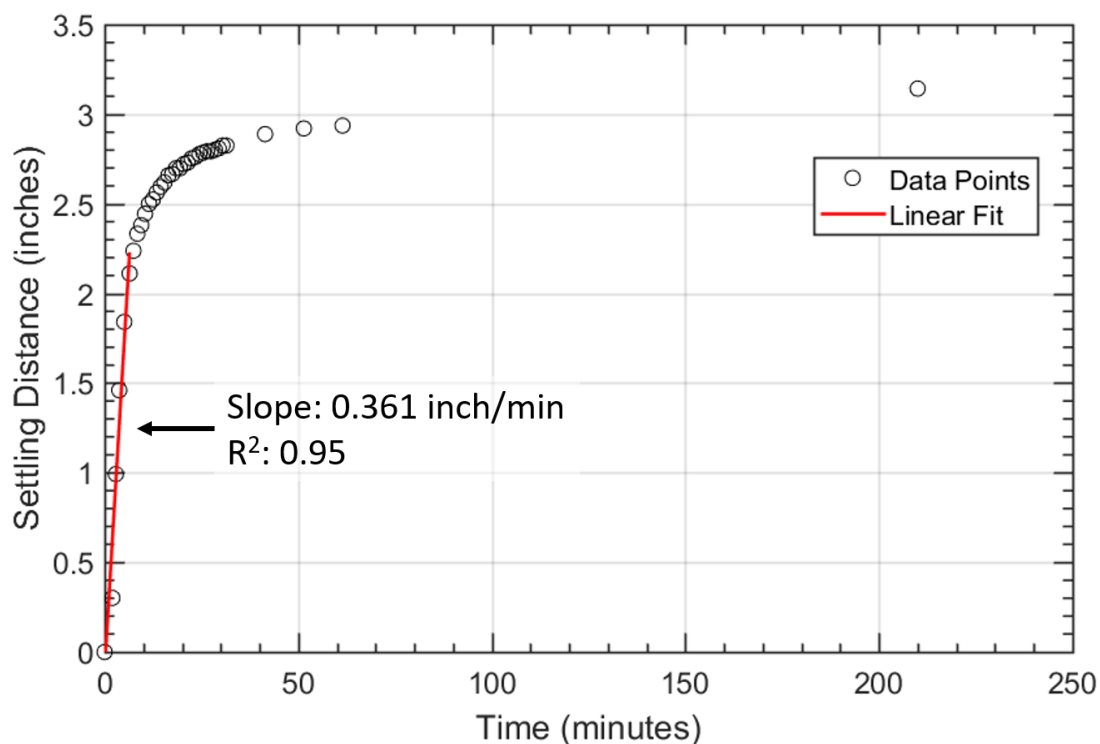


Fig. 4.29 Experimental data points of interfacial position of the emulsion pictured in Fig. 4.28.

Using the mean droplet diameter determined with the microscope images, and the known continuous phase viscosity and density difference between the dispersed and continuous phases, I calculated an expected Stokes' settling velocity using Eq. 4, and solved for the empirical exponent, n , in Eq. 4. For the emulsion pictured in Fig. 4.28 the empirical exponent is -29.6, again suggesting that the emulsion is unstable, and its behavior is not adequately captured by a simplified Stokes' flow analysis. Similar to what was shown in Fig. 4.27, the emulsion formed between water and paraffin wax seems to have rapidly formed droplet aggregates, accelerating sedimentation and causing visible separation within the first two minutes. Photographs of the aggregation process are shown in Fig. 4.32.

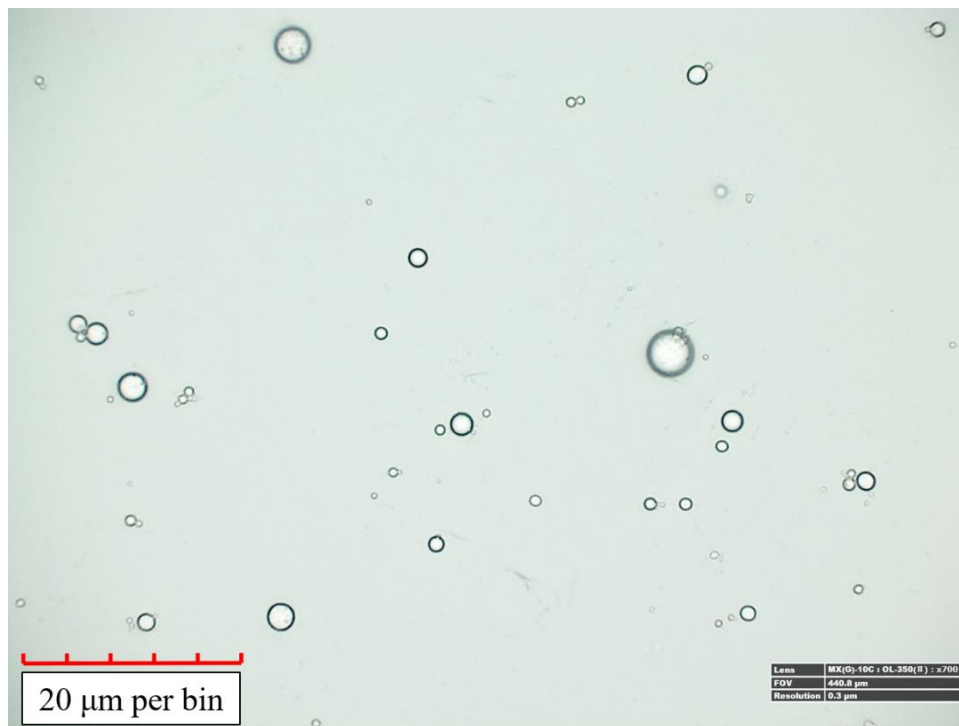


Fig. 4.30 Image of emulsified water droplets from a diluted BDF sample taken on a HIROX KH-8700 digital microscope under 700 times magnification

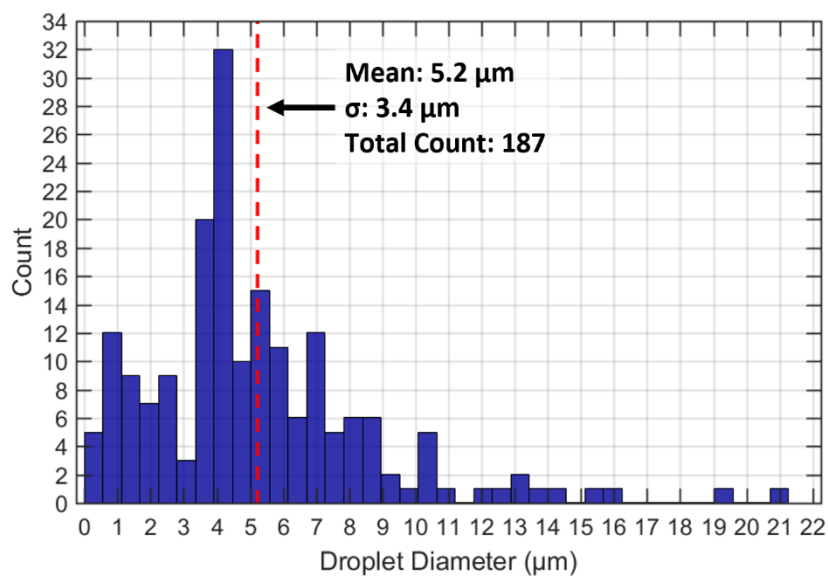


Fig. 4.31 Histogram of emulsion droplet diameters for the emulsion pictured in Fig. 4.28.

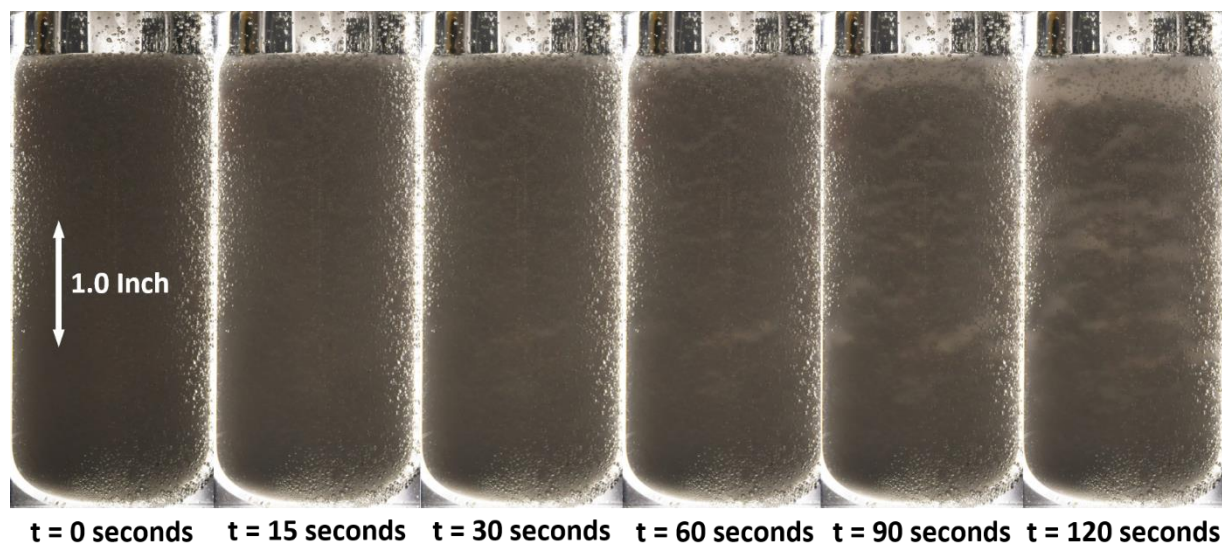


Fig. 4.32 Rapid formation of droplet aggregates in an emulsion formed between water and paraffin wax.

4.5 Biphasic Dispersion Fuel Synthesis

During the course of this research, I synthesized and tested three different biphasic dispersion fuel formulations. The first BDF formulation was formed between paraffin wax and DI water. The second BDF formulation was formed between paraffin wax and an aqueous solution consisting of ethanol and DI water in a 95:5 mass ratio. With difficulties in forming stable emulsions with ethanol, and some success with forming emulsions between water and paraffin oil, I chose to add DI water to ethanol. These first two sets of biphasic dispersions were formed prior to the development of the optically accessible emulsion visualization apparatus described in Section 3.3. Surfactants were chosen based on sample emulsions formed with paraffin oil (CAS #: 8012-95-1) as the continuous phase. Fig. 4.33 shows a sample emulsion formed between DI water and paraffin oil using a mixture of Span[®] 80 and Triton[™] X45 as surfactants. The emulsion took 24 hours to show any signs of change, at which point clear sections of paraffin oil appeared randomly throughout the vial.

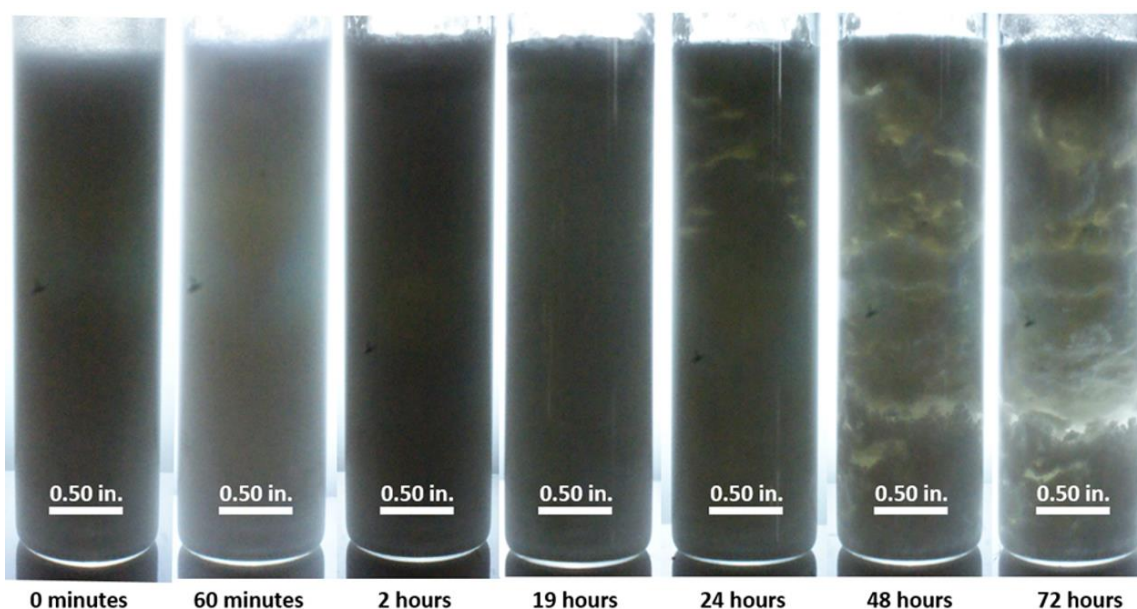


Fig. 4.33 Water-in-paraffin oil emulsion formed with a mixture of Span® 80 and Triton™ X45 as surfactants. Composition is 85 wt.% oil, 10 wt.% water, and 5 wt.% surfactant.

Similarly, I formed a sample emulsion between paraffin oil and the aqueous ethanol solution as shown in Fig. 4.34. An opaque white mixture formed immediately after mixing, but the aqueous ethanol solution began to separate from the paraffin oil after only 15 minutes. After six hours, no further changes were visible. The added water did not appear to make a difference in the emulsion stability. Due to how quickly the ethanol separated from the oil, and issues with how quickly wax mixtures could be cooled to the point of solidifying, BDF formulation two was synthesized with continuous stirring until the wax had solidified.



Fig. 4.34 Ethanol-in-paraffin oil emulsion formed with Span[®] 80 as surfactants. Composition is 85 wt.% oil, 10 wt.% aqueous ethanol solution, and 5 wt.% surfactant.

Each biphasic dispersion formulation contained 75 wt.% paraffin wax, 20 wt.% DI water or aqueous ethanol solution, and 5 wt.% surfactant. BDF formulation one and two were synthesized and mixed using the batch mixing vessel and coring cylinder design discussed in Section 3.5.2. These fuel grains are shown in Fig. 4.35, after preparing them for testing in the OCC with a high temperature silicon caulk to inhibit end burning.

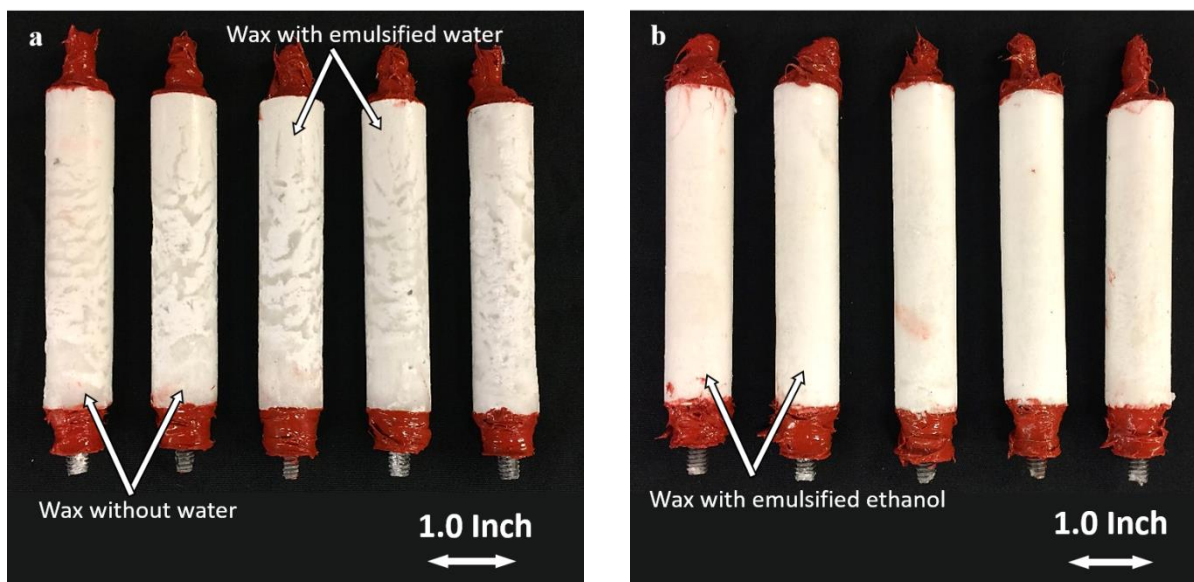


Fig. 4.35 Hybrid rocket fuel grains prepared for OCC testing. a) BDF formulation one. b) BDF formulation two.

Similar to what was observed in the paraffin oil sample emulsion, the paraffin wax based fuels containing water formed random branched structures of emulsified water and clear wax sections during the cooling and solidification process, as shown in Fig. 4.35a. The fuel grains containing ethanol were more homogenous in their appearance, as shown in Fig. 4.35b.

The third BDF formulation was synthesized after making improvements to the synthesis and casting methodology. The third BDF formulation consisted of 20 wt.% water, 79.5 wt.% wax, and 0.5 wt.% surfactant. BDF three fuel grains are shown in Fig. 4.36. Note the difference in appearance between the two fuel grains. Fuel grains were cast using the manifolded casting mold assembly described in Section 3.5.3. Emulsified fuel mixture was injected into two different casting molds sequentially. Each injection took roughly two minutes to complete and thus the first fuel grain injection had two minutes of additional time to settle, prior to disconnecting the grain mold assembly and rapidly cooling. The top fuel grain pictured in Fig. 4.36 was cast first, explaining the difference between the top section containing mostly paraffin wax, and the bottom section containing water droplets dispersed throughout the wax. The bottom grain was cooled quickly enough to prevent settling. I conducted twenty different tests in the OCC, including eight neat paraffin tests, five tests of BDF formulation one, five tests of BDF formulation two, and two tests of BDF formulation three. The results are discussed in the next section.

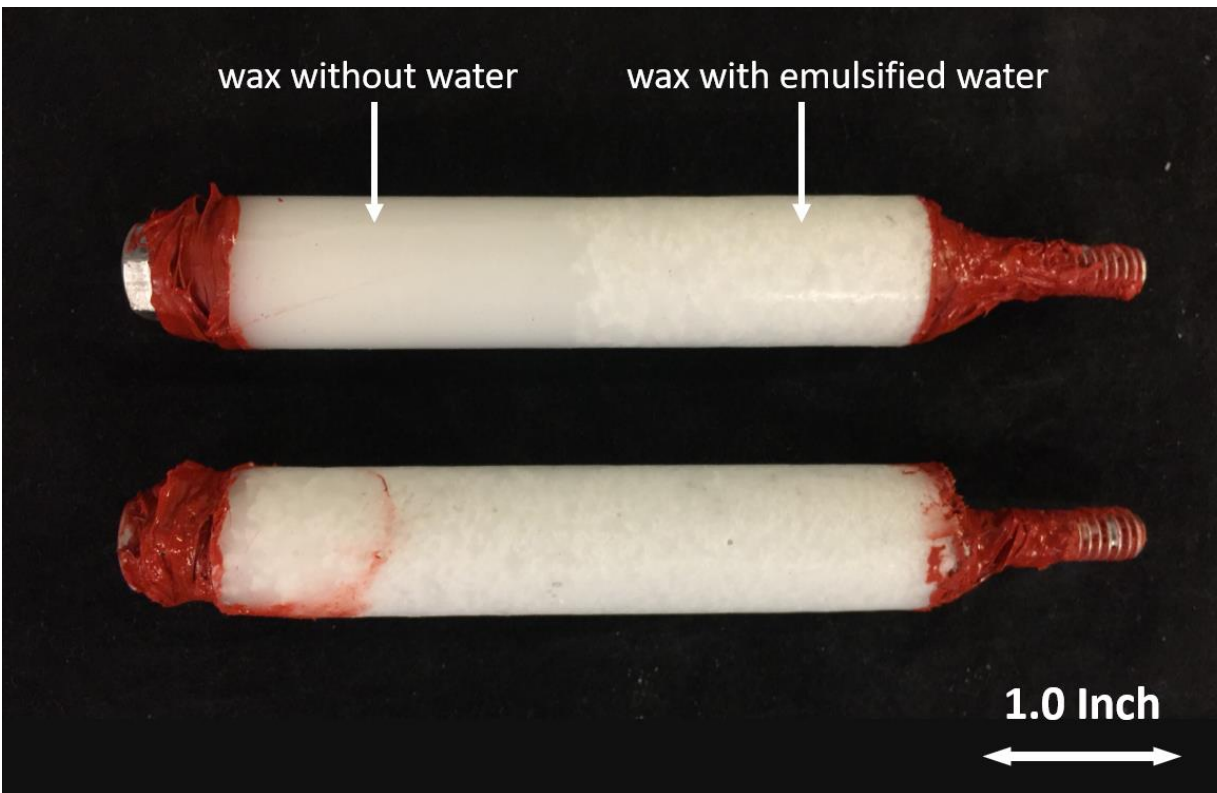


Fig. 4.36 BDF formulation three fuel grains cast using a rapidly cooled injection-style casting mold assembly.

4.6 Combustion Performance Analysis

I tested eight neat paraffin fuel grains in the OCC over a range of oxidizer mass fluxes to form a performance baseline. Similarly, I tested the first and second BDF formulations over a range of oxidizer mass fluxes to compare their performance to the baseline. With only two fuel grains of BDF formulation three, I conducted the OCC tests at a nominal average oxidizer mass flux of $150 \text{ kg/m}^2/\text{s}$ to provide a direct comparison between fuel grains, while also providing a comparison to tests of BDF formulations one and two that were performed at a similar average oxidizer mass flux. A summary of the tests results from all twenty tests is included in Table 4.1. Note that chamber pressure data was not obtained for test number 10 due to a clogged pressure port and regression rate data was not obtained for test number 17 due to overexposure of the video.

Table 4.1 Summary of OCC test results.

Test Number	Fuel Formulation	Mean Oxidizer Mass Flux (kg/m ² /s)	Mean regression Rate (mm/s)	Mean Chamber Pressure (psi)	η_{c^*}
1	Neat Paraffin	75.1 ± 2.0	1.91 ± 0.07	53.2 ± 6.0	93 ± 5.3
2		88.3 ± 2.0	2.34 ± 0.06	57.2 ± 6.0	84 ± 5.0
3		73.0 ± 2.0	2.00 ± 0.06	114.1 ± 6.0	89 ± 6.2
4		80.9 ± 2.0	2.08 ± 0.06	127.0 ± 6.0	91 ± 5.2
5		134.3 ± 2.1	2.32 ± 0.08	197.4 ± 6.0	96 ± 4.4
6		127.7 ± 2.0	2.42 ± 0.09	189.8 ± 6.0	96 ± 4.4
7		124.9 ± 2.1	2.58 ± 0.10	191.6 ± 6.0	92 ± 4.1
8		150.0 ± 2.0	2.69 ± 0.09	219.5 ± 6.0	97 ± 3.6
9	Water BDF	136.6 ± 2.0	2.68 ± 0.08	172.6 ± 6.0	95 ± 4.1
10		157.5 ± 2.0	3.15 ± 0.09	Not Available	Not Available
11		154.5 ± 2.0	3.45 ± 0.06	222.4 ± 6.0	94 ± 3.8
12		155.0 ± 2.0	2.95 ± 0.07	216.3 ± 6.0	91 ± 4.1
13		115.5 ± 2.0	2.46 ± 0.11	169.4 ± 6.0	89 ± 4.9
14	Ethanol BDF	130.7 ± 2.0	4.82 ± 0.07	233.9 ± 6.0	86 ± 4.0
15		147.2 ± 2.0	4.83 ± 0.06	245.9 ± 6.0	87 ± 3.7
16		140.3 ± 2.0	4.77 ± 0.07	240.0 ± 6.0	86 ± 3.9
17		Not Available	Not Available	248.3 ± 6.0	Not Available
18	Water-BDF	132.3 ± 2.0	4.20 ± 0.15	207.7 ± 6.0	90 ± 3.8
19		148.2 ± 2.9	15.0 ± 0.14	229.0 ± 2.0	95 ± 3.1
20		151.2 ± 3.0	16.9 ± 0.15	243.0 ± 2.0	96 ± 3.3

I used a statistical analysis software package, SAS 9.4, to conduct a simple linear regression (SLR) of all combustion performance results. Hybrid rocket fuels are commonly assumed to follow a power law regression rate correlation, as shown in Eq. (6). Although the regression rate of a hybrid rocket fuel depends on more than just one variable, Eq. 6 provides a good fit for the experimental data. More complicated and accurate hybrid rocket regression rate correlations have been developed but are not the subject of this research. If interested, the reader should refer to the works of Chiaverini et al. [38] and Karabeyoglu et al. [6],[39] for their work on the development of semi-empirical regression rate correlations for polymeric and liquifying hybrid rocket propellants, respectively.

$$\dot{r} = a(\dot{G}_{ox})^n \quad (6)$$

The empirical constants, a and n , are determined by taking the logarithm of both sides of Eq. (6), as shown in Eq. (7), and performing an SLR analysis.

$$\log(\dot{r}) = \log(a) + n \cdot \log(\dot{G}_{ox}) \quad (7)$$

Both of the empirical constants were found to be statistically significant at a 95% confidence level for both the neat paraffin fuels and BDF formulation one, but not for the second BDF formulation. I did not perform a statistical analysis of BDF formulation three since only two data points were acquired. A meaningful statistical analysis would require further testing. Regression rate correlations for neat paraffin and BDF formulations one and two are included in Table 4.2, along with representative values for neat paraffin and HTPB found in the work of Zilliac et al. [40].

Table 4.2 Regression rate correlation data for different hybrid rocket propellants

Fuel	a[‡]	n	Average O/F Ratio Range	Number of Tests
Neat Paraffin	0.400	0.375	3.5 – 6.9	8
Water BDF	0.023	0.981	5.0 – 6.2	5
Ethanol BDF	0.282	0.569	4.2 - 5.4	4
Neat Paraffin (SP1-a) [40]	0.488	0.620	1.0 - 4.0	65
HTPB [40]	0.030	0.681	-	16

[‡]Use units of kg/m²/s for G_{ox} to produce average regression rates in units of mm/s

Fig. 4.37 compares the measured regression rates and calculated average oxidizer mass fluxes of the neat paraffin fuels to BDF formulations one and two. Fig. 4.38 compares the measured regression rates and calculated average oxidizer mass fluxes of all twenty OCC tests. Two separate plots were created for clarity due to the wide range of measured regression rates. To compare the regression rates of all three BDF formulations relative to neat paraffin, I used the regression rate correlation empirical constants for neat paraffin, and the calculated average oxidizer mass flux for each test to compute a hypothetical neat paraffin regression rate using Eq. 6. As Fig. 4.37 indicates, both BDF formulations one and two exhibited increases in regression rate, relative to neat paraffin wax, at all investigated oxidizer mass fluxes. At average oxidizer mass fluxes less than 140 kg/m²/s, the water based BDF showed only modest increases in regression rate. At oxidizer mass fluxes greater than 140 kg/m²/s, the water based BDF showed up to a 32% increase in regression rate

over neat paraffin wax at the same average oxidizer mass flux. The ethanol based BDF showed greater increases in regression rate, with up to a 95% increase in regression rate over neat paraffin wax at the same average oxidizer mass flux. OCC tests of BDF formulation three showed a more substantial increase in regression rate than the ethanol-based fuels. Each fuel grain for BDF formulation three was tested at a nominal average oxidizer mass flux of 150 kg/m²/s. Test 19 and Test 20 showed a 466% and 538% increase in regression rate relative to neat paraffin wax for the same nominal average oxidizer mass flux, as shown in Fig. 4.38.

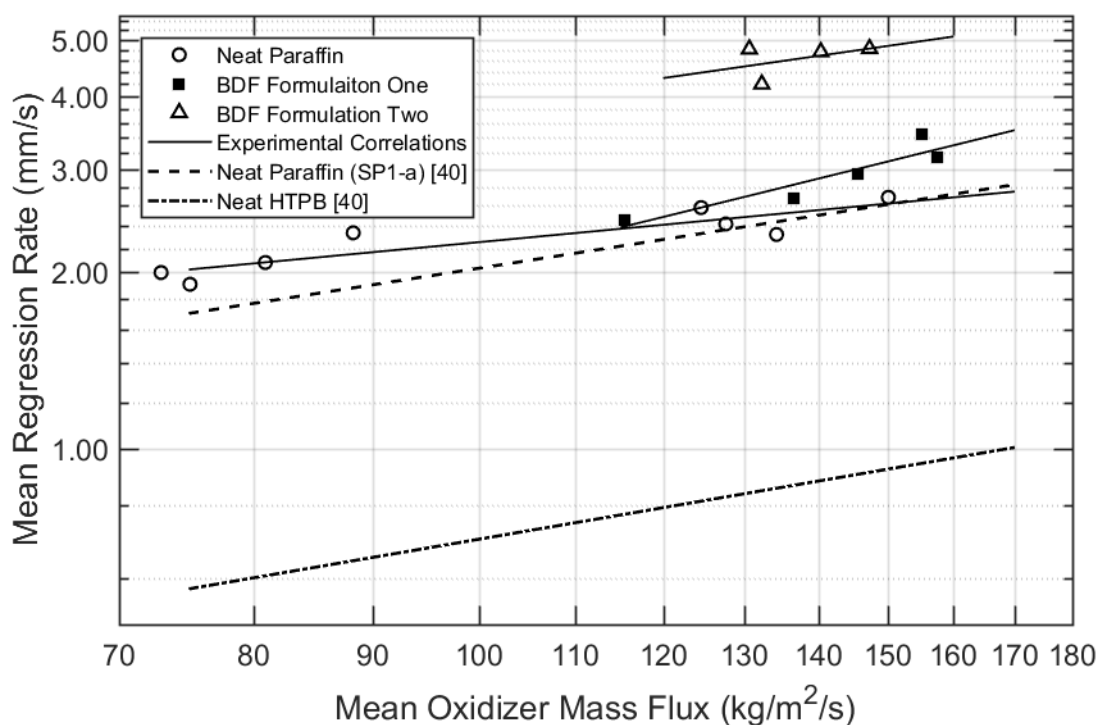


Fig. 4.37 Measured space-time-average regression rates for several different hybrid rocket fuels plotted as a function of mean oxidizer mass flux.

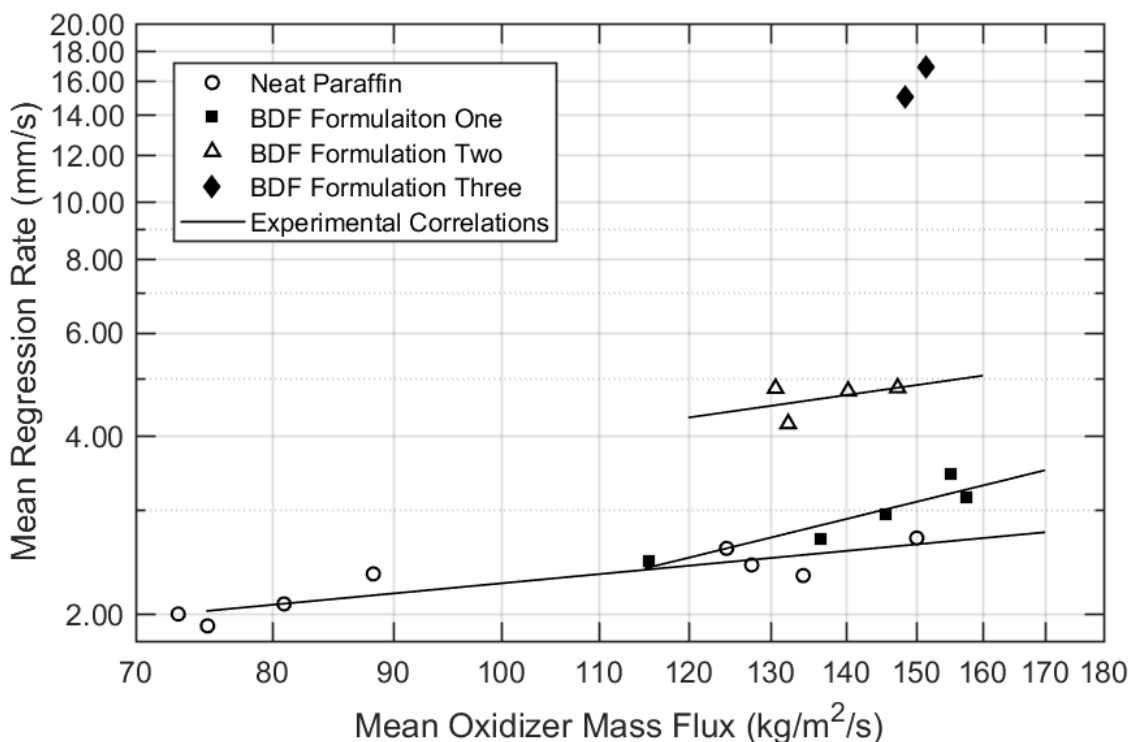


Fig. 4.38 Measured space-time-average regression rates for all three biphasic dispersion fuel formulations plotted as a function of mean oxidizer mass flux.

High speed videos show that all three BDF formulations exhibited a more turbulent combustion than the neat paraffin fuels, with visible increases in both the rate of mass transfer from the fuel surfaces and height of the flame zone, as shown in Fig. 4.39, and microexplosions on both the fuel surface and in the flame zone for the ethanol based BDF tests, as shown in Fig. 4.40. Fig. 4.39 compares the flame height and combustion environment of a neat paraffin fuel grain to all three BDF formulations during an OCC test. Time stamps indicate the time after camera trigger for each test. The top and bottom images for each fuel grain are identical. However, the fuel surface has been outlined for clarity in each of the bottom images. Fig. 4.39a shows a flame that resides close to the fuel surface and a relatively undisturbed port. However, as Fig. 4.39b, Fig. 4.39c, and Fig. 4.39d show, during combustion of the BDF formulations, the flame extends well beyond the fuel surface, creating a more turbulent mixing of fuel and oxidizer species.

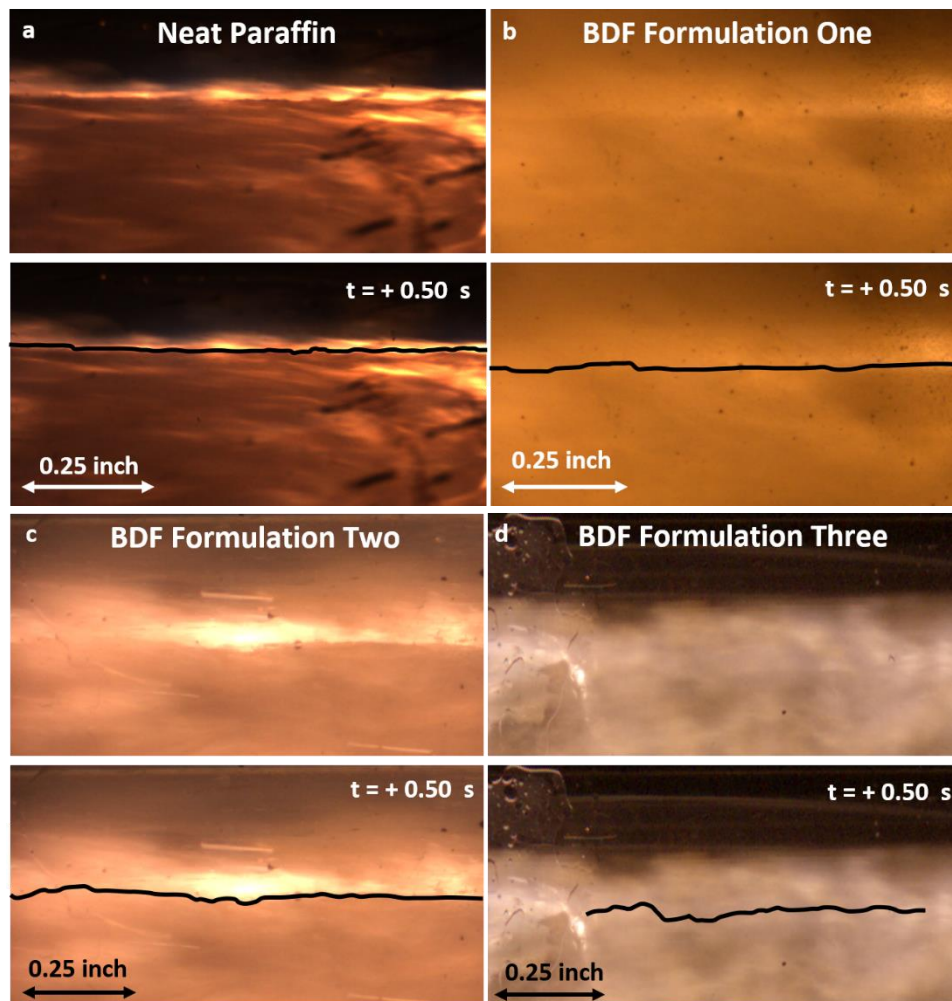


Fig. 4.39 Combustion environment and flame height comparison between three different fuels. Flow is left to right. a) Neat paraffin fuel. b) BDF one (water) c) BDF two (ethanol) d) BDF three (water).

Fig. 4.40 **Error! Reference source not found.** highlights the difference in combustion behavior between the same three tests shown in Fig. 4.39. Pictures are arranged chronologically, from left to right. Fig. 4.40a depicts a more uniform combustion of neat paraffin, relative to the BDF formulations. BDF formulation one and two exhibited surface level explosions, as shown in Fig. 4.40b and Fig. 4.40b. Surface and microexplosions are less visible in the combustion of BDF formulation three, but molten fuel can be seen leaving the surface and combusting in the port region, as shown in Fig. 4.40d.

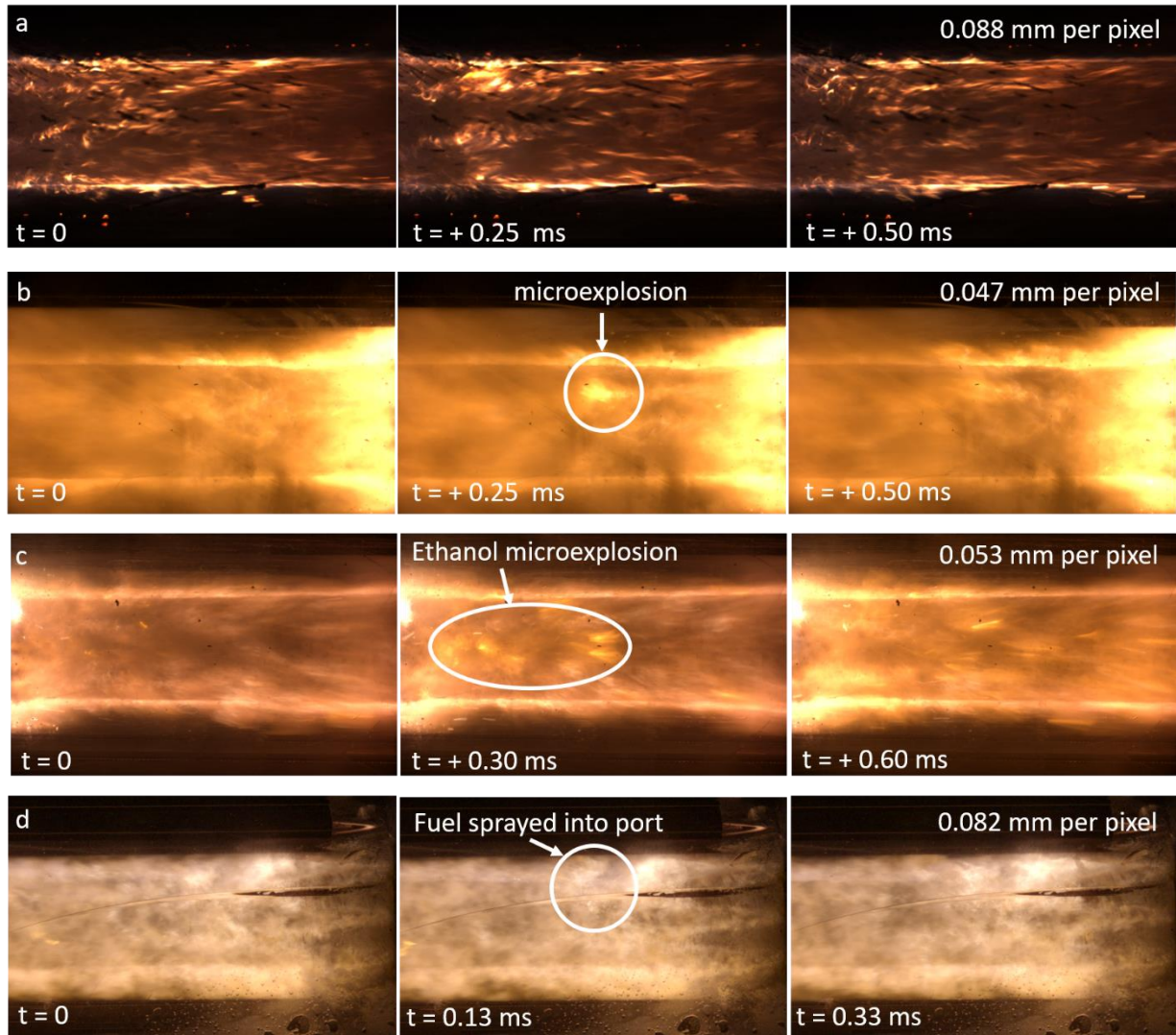


Fig. 4.40 Three subsequent frames from the combustion of hybrid rocket fuels. Flow is left to right. a) Neat paraffin fuel. b) BDF one (water) c) BDF two (ethanol) d) BDF three (water).

The observed increases in regression rates are believed to be caused by surface level microexplosions due to boiling of the liquid fuel additives. These microexplosions would help to disrupt the diffusion-limited combustion regime typical of traditional hybrid rocket systems and more rapidly transfer fuel from the surface to the flame zone. The ethanol-based fuels are believed to have regressed faster than the first water-based fuel formulations due to the greater volatility of ethanol, which would contribute to more violent microexplosions as suggested by the work of Lasheras et al., in addition to the non-reactive nature of water. [11] However, the observed difference in the combustion behavior and regression rate between BDF formulation one and three

(i.e. the two different water-based fuels) is believed to be caused by fuel grain porosity that formed as a result of water leakage during fuel grain casting. Fig. 4.41 one of the two fuel grains of BDF formulation three. The fuel grain clearly shows areas of surface pitting, where emulsified water leaked out during cooling and preparation for testing.

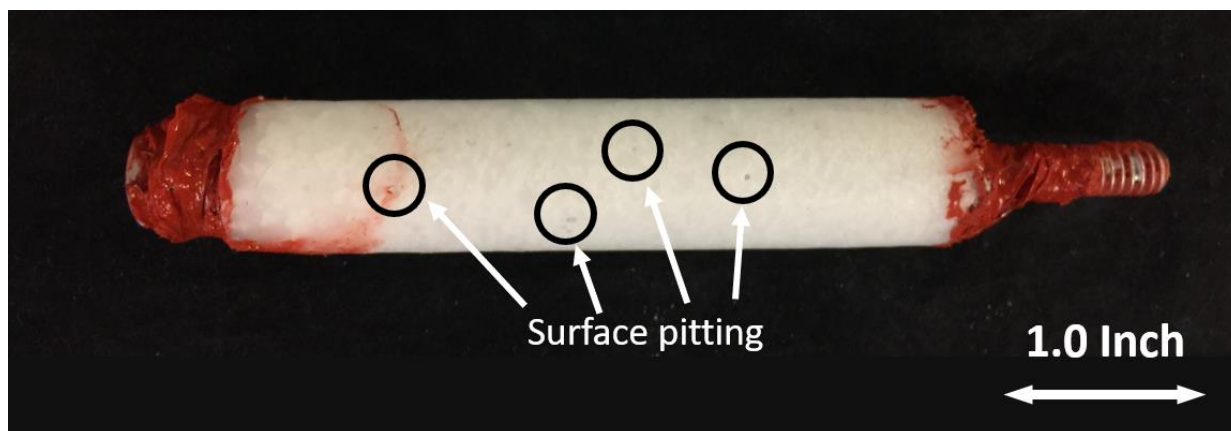


Fig. 4.41 Surface pitting in a fuel grain of BDF formulation three.

Both fuel grains of BDF formulation three were weighed and measured for volume to provide a fuel grain density measurement prior to testing. The measured densities indicate that water leaked out, leaving a mixture of emulsified droplets and porous, air-filled sections throughout the fuel grains. Fig. 4.42 compares the measured fuel grain density to the nominal value expected for a neat paraffin fuel grain and a BDF formulation containing 80 wt.% paraffin wax and 20 wt.% water cast using this method. Neat paraffin fuel grains cast using this method have a nominal density of 882 kg/m^3 , or 95.6% of the theoretical density of FR5560 paraffin wax. Grains one and two of BDF formulation three had measured densities of 806.7 kg/m^3 and 767.8 kg/m^3 , or 86.1% and 82.0% of the expected nominal density, respectively. If all the emulsified water had leaked from the fuel grains, leaving voids in their place, the expected nominal density of fuel grains one and two for BDF formulation three would be 737.5 kg/m^3 , or 78.8% of the expected nominal density. Fig. 4.43 shows a sample of BDF formulation three imaged using a Bruker SKYSCAN 1272 x-ray micro-CT scanner. Fig. 4.43b depicts a horizontal slice of the sample filled with voids. With such a significant portion of the emulsified water replaced by a porous void structure, the fuel grains would be expected to exhibit increased regression rate due an increased burn surface area.

While some water remained trapped within the grain, it is difficult to decipher how much of the increase in regression rate can be attributed to microexplosions, if any, and how much can be attributed to grain porosity and an increased burn surface area.

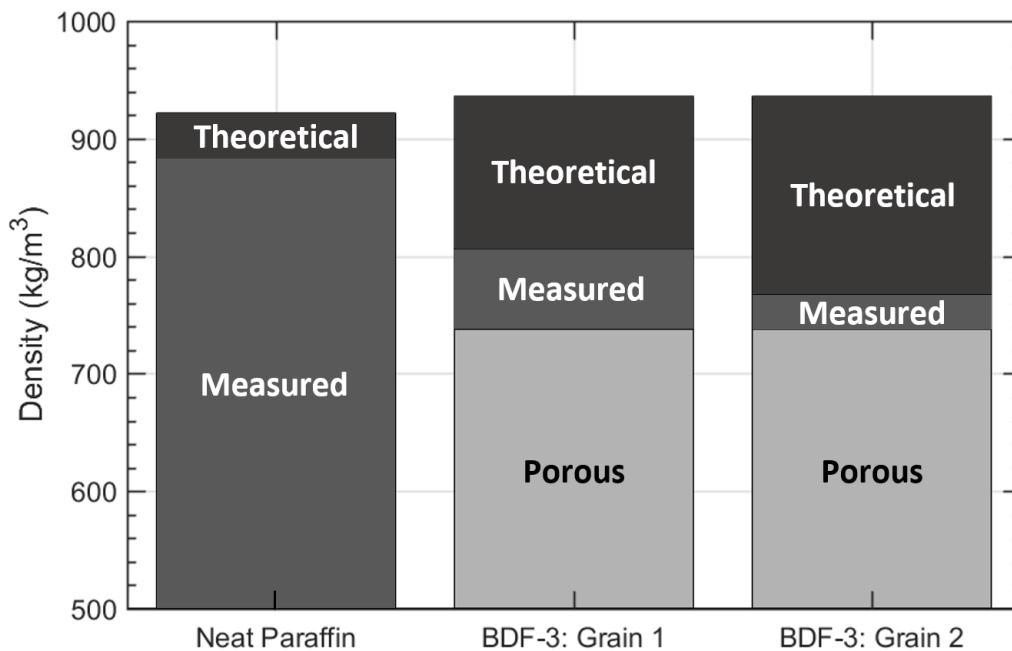


Fig. 4.42 Expected nominal fuel grain densities and measured fuel grain densities for neat paraffin and BDF formulation three.

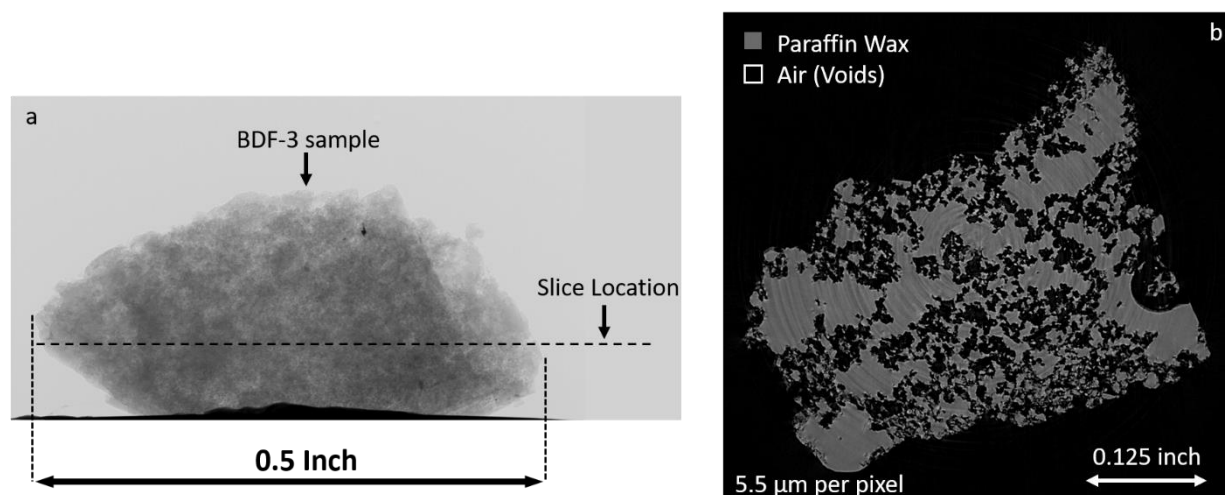


Fig. 4.43 X-ray CT scan image of BDF-3 sample. a) Live x-ray image. b) Image of horizontal slice showing voids.

Pressure traces also indicate that liquid additives dispersed within the fuel binder can augment the fuel regression rate, or in the case of BDF formulation three, a porous internal structure can significantly augment the regression rate. Fig. 4.44 displays representative pressure traces for each formulation and correspond to Test 4, Test 9, Test 18, and Test 19, as found in Table 4.1. A comparison between the pressure decay slopes indicate that the ethanol BDF burned faster than the first water BDF, and that both BDF formulations burned faster than the neat paraffin fuels. The slope of the pressure decay is defined as the change in pressure divided by the time during which the pressure decayed linearly. The corresponding pressure decay slopes for Test 4, Test 9, Test 18, and Test 19 are -10.5 psi/s, -36.3 psi/s, -84.0 psi/s, and -118.2 psi/s as determined using a least squares analysis of the data.

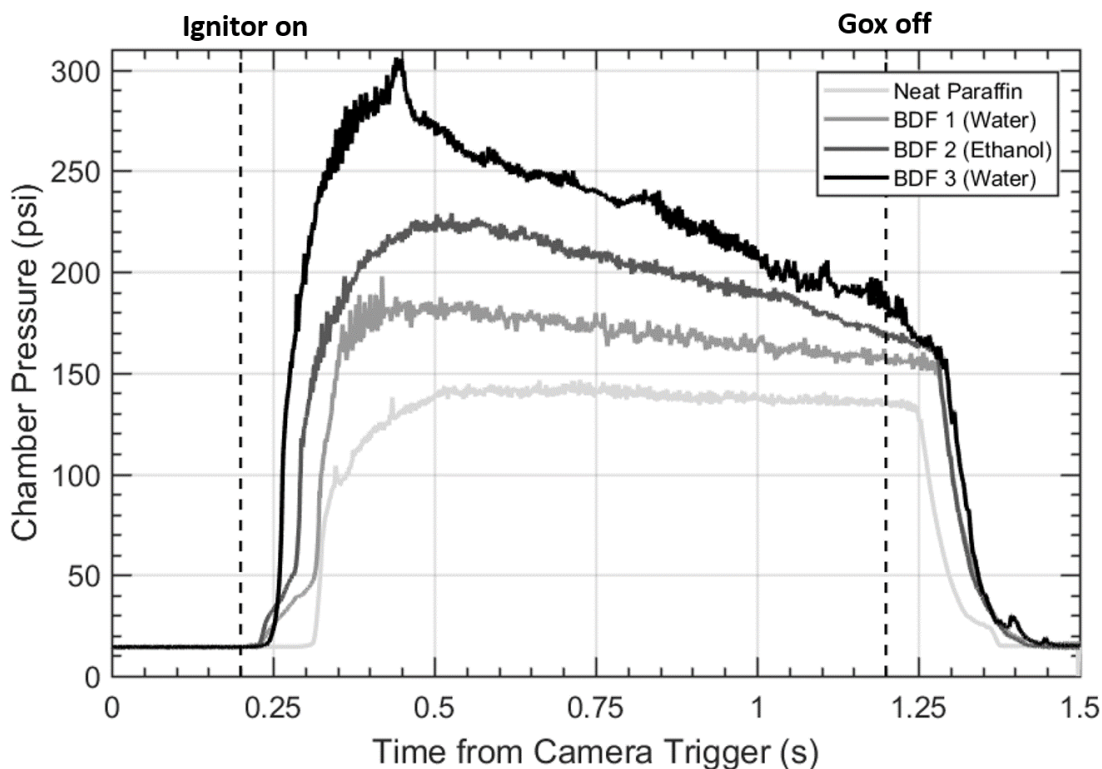


Fig. 4.44 Pressure traces of four different hybrid rocket fuel formulations tested in the OCC.

With up to 32%, 95%, and 538% increases in regression rate for BDF formulations one, two and three, respectively, and a fixed length combustion chamber, one could expect the combustion efficiencies to suffer. However, as Table 1 shows, all three BDF formulations maintained a relatively high combustion efficiency. Fig. 4.45 compares the average combustion efficiency of

all three BDF formulations to the average combustion efficiency of all eight neat paraffin tests. Fig. 4.46 displays the combustion efficiencies from all twenty tests. The combustion efficiency of BDF formulation one exceeded that of the neat paraffin fuel grains by 1% on average, the average combustion efficiency of BDF formulation two was only 4% lower than that of the neat paraffin fuel grains, and the average combustion efficiency of BDF formulation three exceeded that of neat paraffin by 4%, as shown in Fig. 4.45. Note that the combustion efficiency scale has been adjusted for clarity in both Fig. 4.45 and Fig. 4.46.

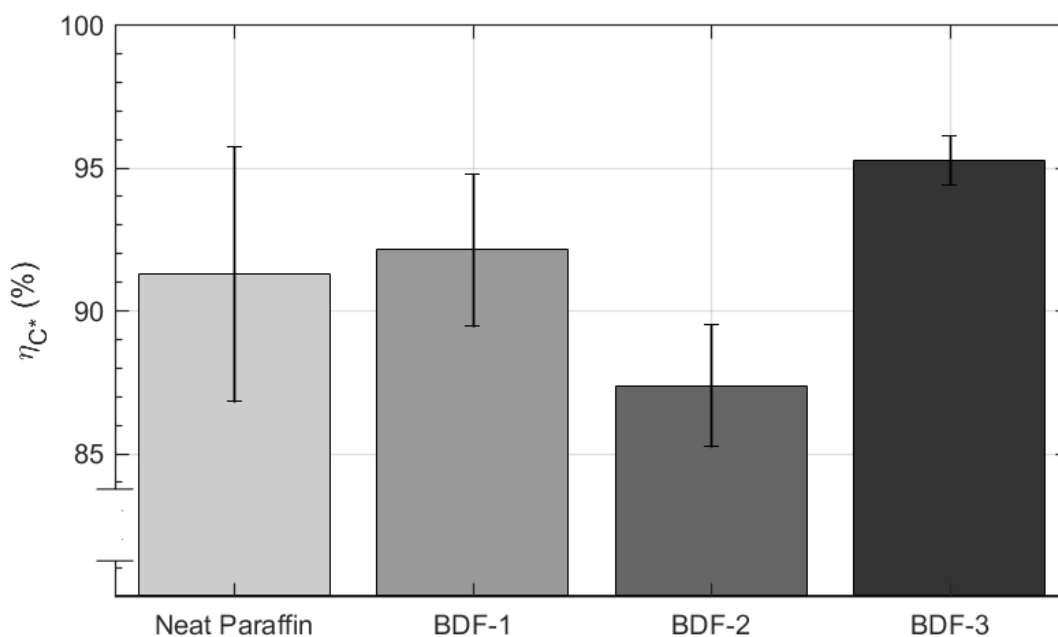


Fig. 4.45 Average combustion efficiencies of four different hybrid rocket fuel formulations tested in the OCC.

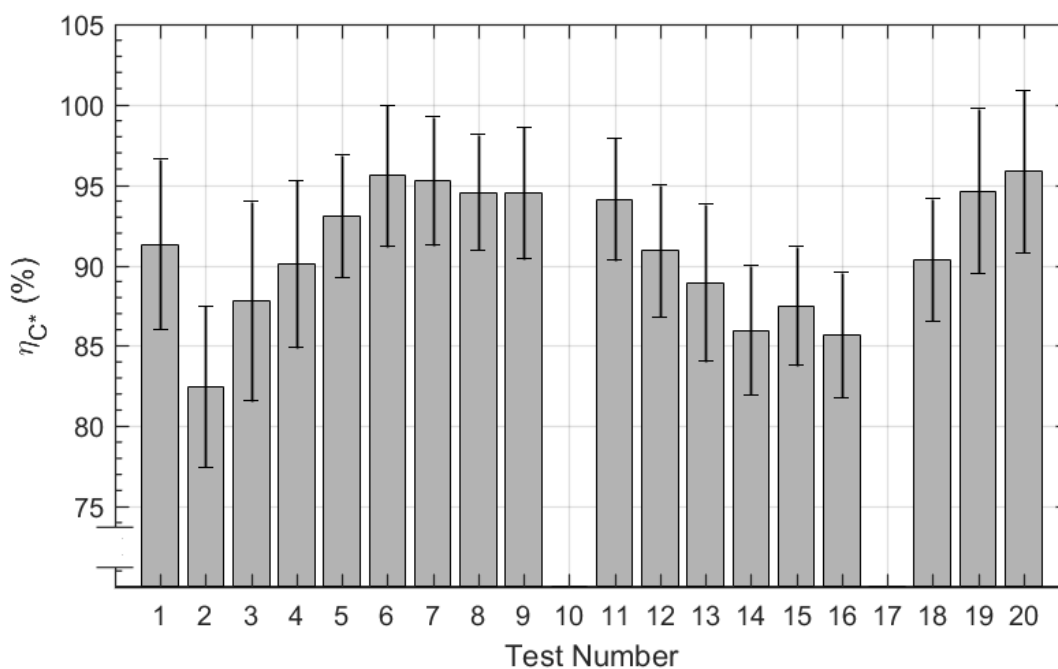


Fig. 4.46 Combustion efficiency of all twenty tests performed in the OCC.

As described previously, the observed increases in regression rate for BDF formulations one and two are attributed to surface microexplosions. I theorize that these microexplosions and the modest increases in fuel mass transfer rate observed for BDF formulation one helped to increase mixing, resulting in a more complete combustion of entrained paraffin. However, the ethanol-based fuels exhibited a more drastic increase in regression rate than BDF formulation one. I theorize that the corresponding increase in the rate of fuel mass transfer from the surface also caused an increase in the amount of unburned paraffin ejected from the nozzle, resulting in a decreased combustion efficiency on average. BDF formulation three exhibited the highest average combustion efficiency of any fuel formulation tested in the OCC. I propose that despite a significant increase in regression rate and mass transfer rate of fuel from the surface, the increased fuel porosity and thus increased burn surface area ultimately reduced the amount of unburned fuel ejected from the nozzle.

Despite the decrease in experimental combustion efficiencies observed for the ethanol-based fuels, the increase in regression rate and fuel mass flowrate for a given oxidizer mass flowrate results in a lower average O/F ratio. A decrease in O/F ratio shifts the reaction closer to stoichiometric, resulting in a higher maximum theoretical characteristic velocity at the experimental conditions,

as shown in Fig. 4.47. The solid black data points represent the maximum theoretical characteristic velocity at the calculated O/F ratio for each test case. The hollow circles represent the calculated characteristic velocity for Test 8, Test 11, Test 15, and Test 20, which represent one test cases from each of the four fuel types, where the nominal average oxidizer mass flux was measured as $150 \text{ kg/m}^2/\text{s}$. The arrows represent deviations from maximum theoretical performance due to incomplete combustion. Test 11 (BDF one) had both a lower maximum theoretical characteristic velocity and calculated characteristic velocity than the comparative neat paraffin case, Test 8. Despite the greater theoretical characteristic velocity for Test 15 (BDF two), the reduced combustion efficiency caused the calculated characteristic velocity to be less than that of Test 8. Test 20 (BDF three) had both the highest theoretical characteristic velocity and calculated characteristic velocity for all tests conducted at a nominal average oxidizer mass flux of $150 \text{ kg/m}^2/\text{s}$ due to the effective decrease in O/F ratio and thus shift towards stoichiometric conditions.

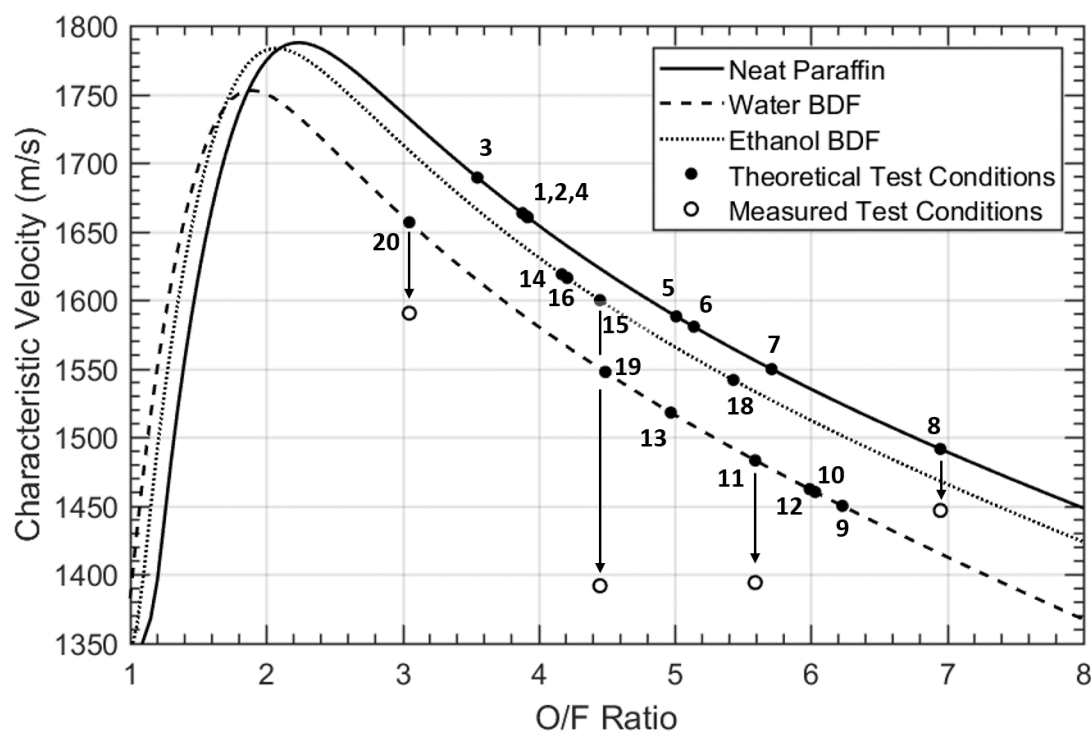


Fig. 4.47 Maximum theoretical characteristic velocity for each fuel formulation as a function of O/F ratio. Numbers refer to test numbers found in Table 4.1.

The thrust produced by each of the four tests conducted at an average oxidizer mass flux of $150 \text{ kg/m}^2/\text{s}$, Test 8, Test 11, Test 15, and Test 20, was also measured, as shown in Fig. 4.48. A simplified theoretical analysis of the expected increase in thrust produced by a paraffin-based fuel exhibiting increased regression rate may provide some perspective. This simplified model assumes a nominal oxidizer mass flowrate and calculates the corresponding nominal oxidizer mass flux and regression rate using the empirical regression rate correlation developed for neat paraffin. Holding the oxidizer mass flowrate constant, the model calculates time-averaged fuel mass flowrate assuming a spatially uniform regression rate, and time-averaged O/F ratio. Using these modeled properties and the NASA Chemical Equilibrium Analysis code (CEA) [27], the resultant theoretical characteristic velocity, specific impulse and thrust are calculated for hypothetical increases in the fuel regression rate. Note that the model assumes a combustion efficiency of 100% for each case. Test 11 (BDF one fuel grain) showed only a slight increase in the peak thrust compared to the neat paraffin baseline, Test 8. Test 11 exhibited a 30% increase in regression rate relative to Test 8, and the model predicts a corresponding increase in thrust of 4.2%, or 1.9 lb_f . The load cell error ($\pm 0.4 \text{ lb}_f$), measured oxidizer mass flux error (nominally $\pm 2.0 \text{ kg/m}^2/\text{s}$), and the reduction in combustion efficiency for Test 11, help to explain the measured 2.2% increase in peak thrust, relative to the base case.

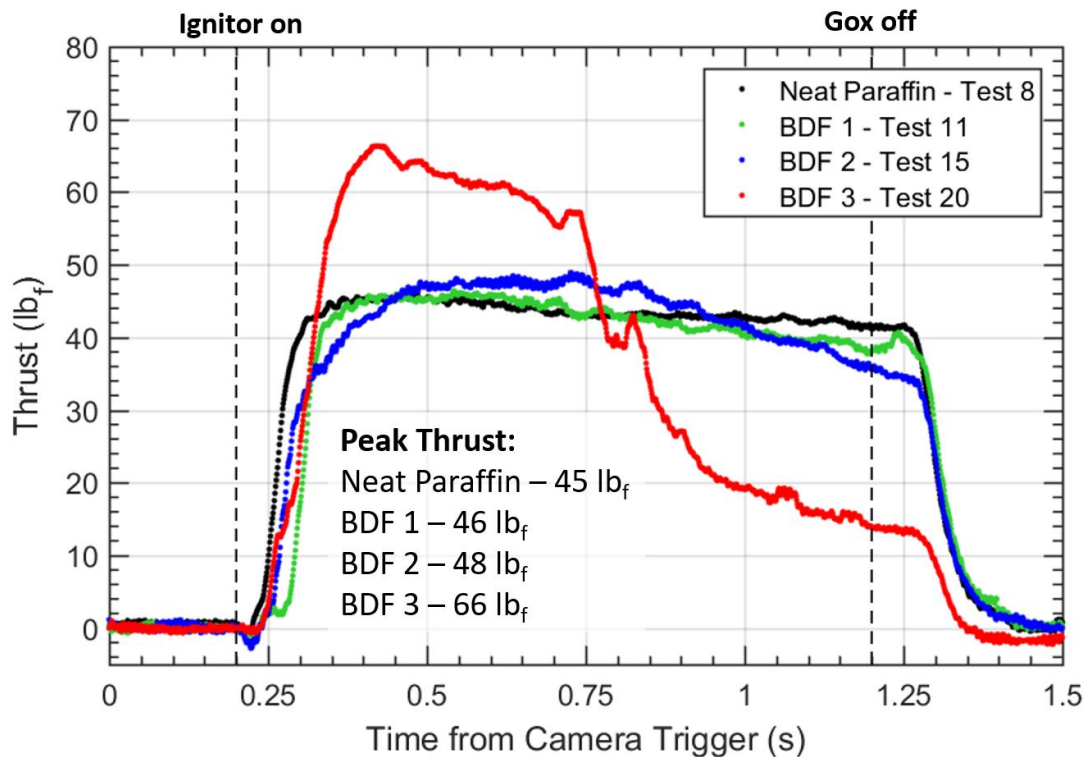


Fig. 4.48 Thrust profile for four different hybrid rocket fuels tested in the OCC at an average nominal oxidizer mass flux of $150 \text{ kg/m}^2/\text{s}$

Test 15 (BDF two fuel grain) showed larger increases in both regression rate (86% increase) and peak thrust (6.7 % increase) relative to the neat paraffin baseline, Test 8. The model predicts an 11.1% increase in thrust for an 86% increase in regression rate. Again, the load cell error, measured oxidizer mass flux error, and the reduction in combustion efficiency for Test 15, help to explain the measured 6.7 % increase in peak thrust, relative to the base case. Test 20 (BDF three fuel grain), showed the largest increase in both regression rate (533%) and peak thrust (46.7%) relative to the neat paraffin baseline test. However, post-test analysis of Test 20 revealed that the nozzle had failed during testing due to excessive heat load. The nozzle throat melted, causing an increase in the throat area. To readjust the analysis, I took pictures of the nozzle throat after its failure and used an image processing code to calculate the increase in throat area. Using the new throat area, the model predicts a 67.3% increase in thrust for the 533% increase in regression rate, assuming complete combustion. The failure of the nozzle during the test introduces further uncertainty in the thrust measurement and thus further testing with a new nozzle is required before making definitive claims about the effective increase in measured thrust for a given increase in fuel regression rate.

5. CONCLUSIONS AND FUTURE WORK

Hybrid rocket systems offer a number of potential benefits over both liquid and solid propellant fueled systems including cost reductions, safety improvements, and simplicity. However, several issues have prevented the development of hybrid rocket technology from reaching a state of widespread use and acceptance as a viable alternative to more traditional systems. Chief among these issues is the low regression rate of hybrid rocket fuels such as hydroxyl-terminated polybutadiene (HTPB) which limit the thrust that can be produced for a given system. Multi-port designs, solid and/or energetic additives, and the use of liquefying hybrid propellants have all been investigated as a means of producing higher fuel regression rates and higher thrust. But unburned fuel slivers, heavy-mass exhaust products, and reduced combustion efficiency, to name a few, are issues inherent to these concepts that have limited performance gains. I investigated a novel approach to augmenting hybrid rocket fuel regression rates, without increasing the complexity of port designs or reducing combustion efficiencies. More specifically, I examined the effect of dispersing volatile and/or reactive liquid fuels within a solid fuel binder on the combustion performance of hybrid rocket fuels. These novel fuels are termed biphasic dispersions, as they contain micron-sized liquid fuel droplets dispersed homogeneously throughout a solid fuel binder.

The techniques employed to synthesize biphasic dispersions involve the emulsification of liquid fuels within fuel binders, using surfactant molecules, at elevated temperature and pressure via high-shear homogenization, and rapid cooling of the emulsified mixture to solidify the binder, trapping liquid droplets in place. Biphasic dispersion fuels were proposed as a means of increasing combustion performance relative to traditional hybrid rocket propellants via secondary atomization effects, or microexplosion phenomenon. As heat is transferred to the fuel surface, or the interior of entrained fuel droplets containing the liquid fuel additive, significant differences in the boiling points of the fuel binder and liquid fuel additive cause rapid increases in pressure to the point of explosion and subsequent secondary droplet breakup. These microexplosions and secondary droplet breakup could help to increase the fuel burn surface area, increase mixing in the boundary layer, and reduce the amount of unburned fuel droplets leaving the nozzle.

Several different volatile and/or hypergolic fuels were proposed as potential liquid fuel additives for the purpose of synthesizing high regression rate hybrid rocket fuels, however only water, ethanol and formamide were investigated due to considerations of liquid additive solubility in the selected fuel binder (FR 5560 paraffin wax), cost, availability, and associated hazards. Surfactant molecules were screened for their ability to stabilize emulsions formed between the selected liquid fuel additives and paraffin wax in small-scale emulsion experiments. Three different biphasic dispersion fuels were prepared to investigate their combustion performance, in terms of regression rate, combustion efficiency, and thrust, in an optically accessible lab-scale hybrid rocket motor relative to neat paraffin wax fuels. Additionally, the average dispersed phase droplet diameters and internal droplet structures were investigated for each synthesized fuel via optical microscopy techniques. The first fuel formulation (BDF-1) contained 75 wt.% paraffin wax, 20 wt.% deionized water, and 5 wt.% surfactant. The second fuel formulation (BDF-2) contained 75 wt.% paraffin wax, 20 wt.% aqueous ethanol solution (95:5 ethanol to water by mass), and 5 wt.% water. The third fuel formulation (BDF-3) contained 79.5 wt.% paraffin wax, 20 wt.% deionized water, and 0.5 wt.% surfactant. BDF-1 showed up to a 30% increase in regression rate and a 1% increase in combustion efficiency on average, relative to neat paraffin fuels tested at similar conditions. BDF-2 showed up to an 86% increase in regression rate and a 4% decrease in combustion efficiency on average, relative to neat paraffin fuels tested at similar conditions. BDF-3 showed up to a 543% increase in regression rate and a 4% increase in combustion efficiency on average, relative to neat paraffin fuels tested at similar conditions. As seen in high speed videos, the improvements in regression rate for BDF-1 and BDF-2 are attributed to microexplosions that occurred on the fuel surface and in the turbulent boundary layer during combustion. The combustion performance improvements measured for BDF-3 are largely attributed to the increase in grain porosity due to the leaking of emulsified water prior to testing.

While the dispersion of liquid fuel droplets within a solid fuel binder has shown greater potential to create formative changes to the current state of hybrid rocket fuels, there are several issues that must be solved to further progress this technology. The synthesis of a stable biphasic dispersion fuel grain hinges on finding a suitable surfactant or surfactant combination to prevent the separation of emulsified droplets prior to casting and cooling fuel grains. In the present research, emulsified fuel mixtures were cooled rapidly using an ice-cooled fuel grain casting mold. However,

as the technology is scaled to accommodate larger applications, fuel cooling becomes more difficult and thus emulsion stability becomes more critical. An effective surfactant could prevent emulsion separation for hours or days and provide adequate time to cure fuels. None of the surfactants tested in this research were effective at stabilizing emulsions formed between water, ethanol or formamide and FR 5560 paraffin wax. More testing with different surfactants is required. High molecular weight triblock copolymers formed between polyethylene-oxide and polypropylene-oxide are reportedly effective surfactants for many different applications in the literature and are a good place to start for future research.

Regarding the fuel binder, FR 5560 paraffin wax was a convenient starting point for this research but possesses several drawbacks. Paraffin wax has found much use as a high-regression rate hybrid rocket fuel over the past decade. However, its low melting point and structural integrity at even modest temperatures limits its use. I found that dispersing liquid fuel additives within paraffin wax further compromises fuel grain structural integrity, often creating cracks, voids, or other non-uniformities. Additionally, the temperature requirements for emulsification set by the melting point of FR 5560 paraffin wax complicates the fuel synthesis hardware and procedures. More traditional polymeric hybrid fuel binders such as hydroxyl-terminated polybutadiene (HTPB), low-density or high-density polyethylene (LDPE/HDPE), or dicyclopentadiene (DCPD) do not share the same structural or temperature limitations with paraffin wax, making them more conducive to holding dispersed liquid fuel droplets in place during storage and testing. These fuel binders have lower regression rates than paraffin wax and could benefit greatly from microexplosions and any resulting enhancement in combustion performance. Similar to the procedures outlined in this dissertation, liquid fuel additives should first be checked for their mutual solubility with the selected fuel binder. PE is highly non-polar and would likely possess similar solubility behavior to paraffin wax. However, PE polarity can be modified by the addition of either polar or non-polar comonomers during polymerization. HTPB is more polar than DCPD, PE, or paraffin wax, and can solvate many additives, making the choice of liquid fuel additive more difficult. Over the course of this research, I investigated the solubility of various volatile and hypergolic liquid fuels with HTPB R-45M resin. I found that 20 wt.% hexane, methanol, ethanol, and 2,3-dihydrofuran added to R-45M resin all formed solutions. Glycol was the only liquid additive that I found to have limited solubility in R-45M, but it does not possess the same potential

for combustion performance enhancements as more volatile, reactive, or hypergolic compounds do. Future work with polymeric hybrid fuel binders in place of paraffin wax would thus first require an extensive screening for solubility behavior. Additionally, catalysis and curing of polymeric fuel binders may affect emulsion stability and should be investigated.

Once a suitable combination of fuel binder, liquid fuel additive, and surfactant have been selected, the research could progress to testing the effect of different concentrations of liquid fuel additive on the combustion performance of biphasic dispersion fuels. During my research, I synthesized and tested biphasic dispersion fuels containing 20 wt.% liquid additives. It would be useful to determine the limits of liquid fuel additive concentration required to augment hybrid rocket fuel combustion performance. A hybrid fuel binder such as HTPB or DCPD would allow for the addition of larger quantities of liquid additive without compromising the structural integrity of the fuel grain. The average droplet size and/or droplet size distribution of emulsified liquid additives may also influence the combustion performance of biphasic dispersion fuels. Further testing and analysis would help to determine how repeatably BDF fuel grains can be synthesized with respect to droplet size distributions.

Overall, the equipment required to synthesize, cast, test, and perform diagnostics on biphasic dispersion fuels have been developed, as described in this dissertation, but much work remains to further develop the technology.

APPENDIX

MATLAB Regression Rate Code

```

%% - - - - - Regression Rate Code - - - - - %%
% - - - - -

%% Code Description
% - - - - -
% This code traces the change in a fuel grain's diameter throughout a test
% fire in the OCC. It requires user input to approximate the location of
% the upper and lower surface of the fuel grain by tracing the surfaces
% with a series of selected points and the code will calculate the
differences
% and average them at X distinct times throughout the test fire. For further
% instructions, refer to the beginning of each subsection below.

close all
clear all
clc

%% Upload Video

% Number of frames to analyze
Nf = 10;

% Read in .avi file format of the cine video
obj = VideoReader('Test_1.avi');

% First frame of video to read, once combustion has started
FirstPict = 500;

% Last frame of the video to read
LastPict = (obj.NumberOfFrames-4000);

% Number of frames to skip (don't want to read thousands of frames)
PictStep = (LastPict - FirstPict)/Nf;

t = 1;
x(t) = 0;
y(t) = 0;
%screenSize = get(0,'ScreenSize');
%Brightness =5;

%% Crop and Calibrate Video

% This section will upload a frame of the high speed video and the user
% will be able to crop the window to any size. The code will record the
% size of the selected crop box and appropriately resize the calibration
% image to the same size. The resized calibration image will be displayed

```

```

% and the user will click in two location, with the line spacing known.
% This known line spacing will allow for the grain diameter to be
% calculated for each frame the user processes.

% Display a frame of the video. User can change the frame number
X = read(obj,FirstPict);
B = imrotate(X,0.0);
thisfig = figure();
thisax = axes('Parent', thisfig);
image(B, 'Parent', thisax);

%% COMMENT BELOW HERE TO VISUALIZE FIRST AND LAST PICTURE
warndlg({'Select Field of View by choosing opposite corners of the
FOV'; 'Press ENTER twice to acknowledge this message'})
pause

% Record the x and y pixel locations of the user's selected FOV
[X00,Y00] = ginputWhite(1);
[X01,Y01] = ginputWhite(1);

% W = Width of FOV & H = Height of FOV, in number of pixels
W = abs(X00-X01);
H = abs(Y00-Y01);
close();

% Can be uncommented to verify calibration image and cropped video frame
% are the same size and aspect ratio
% NewX = imcrop(B, [X00, Y00, W, H]);
% imshow(NewX)
% pause

% Display calibration image
%CHANGE FILE NAME AND ROTATION ANGLE
cal = imread('cal_1to3.bmp');
cal = imrotate(cal,-1.0);
Ncal = imcrop(cal, [300, 200, W, H]);
imshow(Ncal)
warndlg({'Click length scale in Y-Direction'; 'Press ENTER twice to
acknowledge this message'})
pause

% Select two locations on calibration image, with known distance
[X1,Y1] = ginputWhite(1);
[X2,Y2] = ginputWhite(1);
close();

% For length scale along y-axis use the following:
L = abs((Y1) - (Y2));

% Get length scale, from user or hard-code
lengthScale = input('Input calibrated length (in mm): ','s');
lengthScale = str2double(lengthScale);

% Set scale factor
SCALE = lengthScale/L; % [mm/pixel]
close

```

```

%% Video Analysis

% This section will loop through the video, stopping for analysis at
% specific frames decided by the user's input for the number of frames to
% analyze. On every other frame, the user will be prompted to trace the
% top and bottom surfaces of the grain at three locations. The code will
% compute the distance between the y-values of the pixels chosen and
% calculate the grain diameter for that frame. The values be stored as a
% vector.

for i = FirstPict:PictStep>LastPict
    %CHANGE ROTATION ANGLE IF YOU NEED ONE
    X = read(obj, i);
    B = imrotate(X,0.0);
    thisfig = figure();
    thisax = axes('Parent', thisfig);
    image(B, 'Parent', thisax);
    C = imcrop(B,[X00 Y00 W H]);
    imshow(C)
    hold on

    if t == 1
        warndlg({'Select 3 pairs of points, alternating top then bottom for
each pair, along the fuel grain surface'...
                ;'Press ENTER twice to acknowledge this message'})
        pause
    end

    %Mouse inputs for grain surface
    % T = Top Surface
    % B = Bottom Surface

    % Pair 1
    [X_T_1(t),Y_T_1(t)] = ginputWhite(1);
    [X_B_1(t),Y_B_1(t)] = ginputWhite(1);

    % Pair 2
    [X_T_2(t),Y_T_2(t)] = ginputWhite(1);
    [X_B_2(t),Y_B_2(t)] = ginputWhite(1);

    % Pair 3
    [X_T_3(t),Y_T_3(t)] = ginputWhite(1);
    [X_B_3(t),Y_B_3(t)] = ginputWhite(1);

    X_T(:,t) = [X_T_1(t);X_T_2(t);X_T_3(t)];
    X_B(:,t) = [X_B_1(t);X_B_2(t);X_B_3(t)];
    Y_T(:,t) = [Y_T_1(t);Y_T_2(t);Y_T_3(t)];
    Y_B(:,t) = [Y_B_1(t);Y_B_2(t);Y_B_3(t)];

    Diameter_Raw(:,t) = abs(Y_T(:,t) - Y_B(:,t));

    Diam_Avg(:,t) = mean(Diameter_Raw(:,t))*SCALE;

    % Change denominator to match FPS of video

```

```
time(t) = t*PictStep/10000;
t = t + 1;
close();

end

% Linear Fit of Diameter Data

coeffs = polyfit(time,Diam_Avg,2);
yFitted = polyval(coeffs,time');
yresid = Diam_Avg-yFitted';
SSresid = sum(yresid.^2);
SStotal = (length(Diam_Avg)-1)*var(Diam_Avg);
rsq = 1 - (SSresid/SStotal);

slope = num2str(coeffs(1));
rsq = num2str(rsq);

%% Plots and Data Analysis

% Change in time
dt = time(end) - time(1);

% Regression Rate, in [mm/s]
r_dot = 0.5*(yFitted(1) - yFitted(end)) / (dt);

save('Data','time','Diam_Avg','yFitted','r_dot','L','SCALE');

figure(1)
plot(time,Diam_Avg)
hold on
plot(time,yFitted)
```

REFERENCES

- [1] Vonderwell, D. J., Murray, I. R., and Heister, S. D., “Optimization of Hybrid-Rocket-Booster Fuel-Grain Design,” vol. 32, 1995, pp. 6–11, 10.2514/3.26716.
- [2] Zaseck, C. R., Son, S. F., and Pourpoint, T. L., “Combustion of micron-aluminum and hydrogen peroxide propellants,” vol. 160, 2013, pp. 184–190.
- [3] Zaseck, C. R., Shark, S. C., Son, S. F., and Pourpoint, T. L., “Performance of Aluminum-Based Additives in Paraffin Fueled Hybrid Rocket Motors,” *10th International Symposium on Special Topics in Chemical Propulsion & Energetic Materials*, 2014.
- [4] Weismiller, M. R., Connell, T. L., Risha, G. A., and Yetter, R. A., “Characterization of Ammonia Borane (NH₃BH₃) Enhancement to a Paraffin Fueled Hybrid Rocket System.,” 2010, pp. 1–12, 10.2514/6.2010-6639.
- [5] Li, Z., Wang, N., Shi, B., Li, S., and Yang, R., “Effects of Particle Size on Two-Phase Flow Loss in Aluminized Solid Rocket Motors,” vol. 159, 2019, pp. 33–40, 10.1016/j.actaastro.2019.03.022.
- [6] Karabeyoglu, M. A., Altman, D., and Cantwell, B. J., “Combustion of liquefying hybrid propellants: Part 1, General theory,” *Journal of Propulsion and Power*, vol. 18, 2002, pp. 610–620, 10.2514/2.5975.
- [7] Karabeyoglu, A., Ziliac, G., Cantwell, B. J., DeZilwa, S., and Castellucci, P., “Scale-Up Tests of High Regression Rate Paraffin-Based Hybrid Rocket Fuels,” *Journal of Propulsion and Power*, vol. 20, 2004, pp. 1037–1045, 10.2514/1.3340.
- [8] Hiemenz, Paul C., R. R., *Principles of Colloid and Surface Chemistry*, 1997.
- [9] Syu, J., Chang, Y., Tseng, C., Yan, Y., Chang, Y., Chen, C., Lin, W., Syu, J., Chang, Y., Tseng, C., Yan, Y., Chang, Y., and Lin, W., “Effects of Water-Emulsified Fuel on a Diesel Engine Generator ’s Thermal Efficiency and Exhaust,” *Journal of the Air & Waste Management Association*, vol. 64, 2014, pp. 970–978, 10.1080/10962247.2014.905508.
- [10] Chávez, A., Ramírez, M., Medina, E., Bolado, R., and Mora, J., “Advances in the generation of a new emulsified fuel,” *Heat and Mass Transfer/Waerme- und Stoffuebertragung*, vol. 47, 2011, pp. 1051–1063, 10.1007/s00231-011-0858-9.
- [11] Lasheras, J.C.; Fernandez-Pello, A.C.; Dryer, F. ., “On The Disruptive Burning of Free Droplets of Alcohol/n-paraffin solutions and emulsions.,” 1981.

- [12] Shepherd, J. E., and Sturtevant, B., “Rapid evaporation at the superheat limit,” *Journal of Fluid Mechanics*, vol. 121, 1982, pp. 379–402, 10.1017/S0022112082001955.
- [13] Elgowainy, A., Ashgriz, N., “Microexplosion of Emulsified Fuel Drops,” pp. 1–6.
- [14] Ching, E. J., Thomas Avedisian, C., Cavicchi, R. C., Chung, D. H., Rah, K. J., and Carrier, M. J., “Rapid evaporation at the superheat limit of methanol, ethanol, butanol and n-heptane on platinum films supported by low-stress SiN membranes,” *International Journal of Heat and Mass Transfer*, vol. 101, 2016, pp. 707–718, 10.1016/j.ijheatmasstransfer.2016.04.008.
- [15] Law, C. K., Lee, C. H., and Srinivasan, N., “Combustion characteristics of water-in-oil emulsion droplets,” *Combustion and Flame*, vol. 37, 1980, pp. 125–143, 10.1016/0010-2180(80)90080-2.
- [16] Eberhart, J. G., and Schnyders, H. C., “Application of the Mechanical Stability Condition to the Prediction of the Limit of Superheat for Normal Alkanes, Ether, and Water,” 1973, pp. 2730–2736, 10.1021/j100641a004.
- [17] “Thermophysical Properties of Fluid Systems,” *National Institute of Standards and Technology* Available: <https://webbook.nist.gov/chemistry/fluid/>.
- [18] Jiao, J., and Burgess, D. J., “Ostwald ripening of water-in-hydrocarbon emulsions,” *Journal of Colloid and Interface Science*, vol. 264, 2003, pp. 509–516, 10.1016/S0021-9797(03)00276-5.
- [19] Tadros, T. F., *Applied Surfactants: Principles and Applications*, WILEY-VCH, 2005.
- [20] Meng, F., Wang, S., Wang, Y., Liu, H., and Huo, X., “Microencapsulation of oxalic acid via oil-in-oil (O / O) emulsion solvent evaporation,” *Powder Technology*, vol. 320, 2017, pp. 405–411, 10.1016/j.powtec.2017.07.073.
- [21] Oh, C., Park, J. H., Shin, S., and Oh, S. G., “O / W / O Multiple Emulsions via One - Step Emulsification Process,” vol. 2691, 2006, 10.1081/DIS-120027668.
- [22] Imhof, A., and Pine, D. J., “Stability of nonaqueous emulsions,” *Journal of Colloid and Interface Science*, vol. 192, 1997, pp. 368–374, 10.1006/jcis.1997.5020.
- [23] Marxman, G., and Gilbert, M., “Turbulent Boundary Layer Combustion in the Hybrid Rocket.”
- [24] Marquardt, T., and Majdalani, J., “Review of Classical Diffusion-Limited Regression Rate Models in Hybrid Rockets,” 2019, 10.3390/aerospace6060075.

- [25] Benhidjeb--Carayon, A., Gabl, J. R., and Pourpoint, T. L., "Hypergolic Ignition and Relights of a Paraffin-based Hybrid Grain," 2018, pp. 1–14, 10.2514/6.2018-4661.
- [26] Benhidjeb-carayon, A., Drolet, M. P., Gabl, J. R., and Pourpoint, T. L., "Reactivity and Hypergolicity of Solid Fuels with Mixed Oxides of Nitrogen," vol. 35, 2019, 10.2514/1.B37297.
- [27] McBride, J., Gordon, S. M., "Computer Program for Calculation of Complex Chemical Equilibrium Compositions and Applications, Part II: User's Manual and Program Description," 1996.
- [28] Company, C., "Material Safety Data Sheet," p. 8.
- [29] French, H. T., Richards, A., and Stokes, R. H., "Thermodynamics of the Partially Miscible System Ethanol + Hexadecane," 1979, pp. 671–686.
- [30] Souza, W. J., Santos, K. M. C., Cruz, A. A., Franceschi, E., Dariva, C., Santos, A., and Santana, C. C., "Effect of Water Content, Temperature, and Average Droplet Size on the Settling Velocity of Water-in-Oil Emulsion," 2015, 10.1590/0104-6632.20150322s00003323.
- [31] Richardson, J. F., and Zaki, W. N., "Sedimentation and Fluidisation: Part I," *Chemical Engineering Research and Design*, vol. 75, 1954, pp. S82–S100, 10.1016/S0263-8762(97)80006-8.
- [32] Shark, S. C., Zaseck, C. R., Pourpoint, T. L., Son, S. F., and Heister, S. D., "Performance and Flame Visualization of Dicyclopentadiene Rocket Propellants with Metal Hydride Additives," vol. 32, 2016, 10.2514/1.B35853.
- [33] Sutton, G., and Biblarz, O., *Seventh Edition*, Hoboken: Joh Wiley & Sons, INC., 2001.
- [34] Coleman, H.W., Steele, W. G., *Experimentation and Uncertainty Analysis for Engineers*, John Wiley and Sons, Inc., 1999.
- [35] Emel, V. N., Verevkin, S. P., and Varfolomeev, M. A., "Thermochemical Properties of Formamide Revisited: New Experiment and Quantum Mechanical Calculations .," 2011, pp. 7–10.
- [36] Sakthivel, T., Jaitely, V., Patel, N. V, and Florence, A. T., "Non-aqueous emulsions: hydrocarbon – formamide systems," vol. 214, 2001, pp. 43–48.

- [37] Xu, Q., Nakajima, M., and Nabetani, H., “The Effects of Ethanol Content and Emulsifying Agent Concentration on the Stability of Vegetable Oil – Ethanol Emulsions,” vol. 78, 2001, pp. 1185–1190.
- [38] Chiaverini, M. J., Kuo, K. K., Peretz, A., and Harting, G. C., “Regression-Rate and Heat-Transfer Correlations for Hybrid Rocket Combustion,” vol. 17, 2001, 10.2514/2.5714.
- [39] Karabeyoglu, M. A., and Cantwell, B. J., “Combustion of Liquefying Hybrid Propellants: Part 2 , Stability of Liquid Films,” vol. 18, 2002, 10.2514/2.5976.
- [40] Zilliac, G., and Karabeyoglu, M. A., “Hybrid Rocket Fuel Regression Rate Data and Modeling,” 2006, pp. 1–21, 10.2514/6.2006-4504.

VITA

JOSHUA D. MATHEWS

RELEVANT EXPERIENCE

NASA Space Technology Research Fellow (Fall 2015 – Summer 2019)

Advisor: Dr. Timothée Pourpoint, NASA Research Collaborator: George Fletcher

Objective: To determine the effect of volatile and/or hypergolic liquid fuel droplets, homogeneously dispersed within a solid fuel binder, on the combustion performance of hybrid rocket propellants

- Biphasic dispersion fuels were synthesized by emulsifying liquid fuel additives into heated wax and quickly freezing to trap droplets within a solid fuel binder matrix
- Fuel performance was tested in an optically accessible lab-scale hybrid rocket motor and visualized using high-speed cameras
- Biphasic dispersion fuels exhibited augmented regression rates, with increases of up to 95% when burned with gaseous oxygen, relative to neat paraffin wax at similar test conditions

Air Force Research Lab at Edwards Air Force Base (Summer 2018)

Supervisor: Adam J. Brand

- Designed modular hypergolic propellant combustor hardware to experimentally determine the combustion efficiency of various fuel/oxidizer combinations over a range of chamber conditions
- Updated a LabVIEW virtual instrument (VI) to interface with an existing test stand and data acquisition system
- Gained experience in solid propellant chemistry and synthesized HTPB-based propellants using volatile and hypergolic plasticizers

NASA Marshall Space Flight Center (Summer 2017)

Supervisor: George T. Story

- Designed experiments to determine the effect of thermal cycling and cure rate on residual hoop stresses present in JPL Mars Ascent Vehicle (MAV) hybrid propellants
- Performed residual stress analyses using strain gauges via the crack compliance method

Launch Vehicle Design (Spring 2017)

- Conceptual design of a LOX/LCH₄ reusable first-stage, rotating detonation engine powered launch vehicle
- Led the design and analysis of an ox-rich pre-burner and ox-rich staged combustion engine cycle
- Designed an autogenous pressurization system to provide the required turbopump assembly inlet pressures

NASA Ames Research Center (Summer 2016)

Supervisor: Gregory G. Zilliac

- Built a control panel to safely regulate nitrous oxide conditions during the Peregrine hybrid rocket pre-launch operations
- Created a LabVIEW VI to remotely control and monitor the transfer and conditioning of nitrous oxide
- Began testing and implementation of flight-system hardware and the control system VI

Lightweight Hydrogen/Oxygen Thermal Generation for Fuel Cell Power (Fall 2014 – Fall 2015)

- Modeled the heat transfer and diffusion of chemical species for various chemical hydrides using COMSOL Multiphysics
- Tested the efficiency of chemical hydride hydrogen gas production via thermal decomposition experiments
- Designed and performed an aging study to test the chemical compatibility of various metals with chemical hydrides

EDUCATION

Purdue University – West Lafayette, IN

Ph.D. in Aeronautics and Astronautics, Major – Propulsion (Summer 2019, Anticipated) – GPA: 3.74/4.00

Purdue University – West Lafayette, IN

M.S. in Aeronautics and Astronautics, Major – Propulsion (May 2016)

Carnegie Mellon University – Pittsburgh, PA

B.S. in Chemical Engineering (May 2011)

PUBLICATIONS

- Mathews, J., Gabl, J., and Pourpoint, T., "Biphasic Dispersion Fuels for High Regression Rate Hybrid Rockets", *Journal of Propulsion and Power*, Accepted for publication on 13, May 2019, Published online on 10, June 2019.
- Mathews, J., Gabl, J., and Pourpoint, T. "High Performance Hybrid Rocket Colloidal Dispersion Propellants", 54th AIAA/ASME/SAE/ASEE Joint Propulsion Conference, 2018, AIAA Paper 2018-4662.
- Mathews, J., Gabl, J., and Pourpoint, T. "Reactive Colloidal Dispersions for High Performance Hybrid Propulsion", 53rd AIAA/SAE/ASEE Joint Propulsion Conference, 2017, AIAA Paper 2017-5049
- Baker, C., Mathews, J., McKee, L. & Severson, K. "Conceptual Design of the Supply Chain and Production Facility of Lignocellulosic Bio-ethanol via Hydrolysis." Pittsburgh: CACHE Process Design Case Studies. (2011)
- DeLacy, Redding, Mathews, & Army Edgewood Chemical Biological Center APG MD Research Technology Dir., "Optical, Physical, and Chemical Properties of Surface Modified Titanium Dioxide Powders," 2011.

SOFTWARE AND COMPUTER SKILLS

C/C++, COMSOL Multiphysics, LabVIEW, MATLAB, Microsoft Office, NASA CEA, SolidWorks, SPARTA DSMC, Surface Evolver

RELEVANT COURSEWORK

Advanced Rocket Propulsion, Combustion, Computational Aerodynamics, Fluid Mechanics, Gas Dynamics, Heat and Mass Transfer, Launch Vehicle Design, Laser Diagnostics for Reacting Flows, Liquid Propellant Chemistry and Applications

ACTIVITIES

- Carnegie Mellon Varsity Swimming and Diving Team (Fall 2007 – Fall 2010)
 - University Athletic Association All Academic Recognition (2008 – 2010)
 - CSCAA Honorable Mention Scholar All American (2008, 2009)
- Student-Athlete Advisory Council (Fall 2008 – Spring 2010)

PUBLICATIONS

Journal Papers

Mathews, J.D., Gabl, J.R., and Pourpoint, T. L., “Biphasic Dispersion Fuels for High-Regression-Rate Hybrid Rockets,” *Journal of Propulsion and Power*, Accepted for publication on 13, May 2019, Published online on 10, June 2019, 10.2514/1.B37431.

Conference Papers

Mathews, J.D. and Pourpoint, T. L., “Biphasic Dispersion Fuels for Hybrid Rocket Applications,” 66th JANNAF Propulsion Meeting, 2019.

Mathews, J.D., Gabl, J.R., and Pourpoint, T. L., “High Performance Hybrid Rocket Colloidal Dispersion Propellants,” 54th AIAA/ASME/SAW/ASEE Joint Propulsion Conference, 2018, AIAA Paper AIAA 2018-4662, 10.2514/6.2018-4662

Mathews, J.D., Gabl, J.R., and Pourpoint, T. L., “Reactive Colloidal Dispersions for High Performance Hybrid Propulsion,” 53rd AIAA/ASME/SAW/ASEE Joint Propulsion Conference, 2017, AIAA Paper 2017-5049, 10.2514/6.2017-5049.